Study of binding energy of hypertriton from measurement of hypernuclear production cross sections using K meson beam
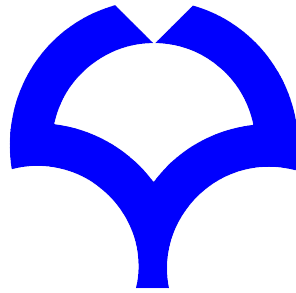
Takaya Akaishi

A dissertation subttemitted to

the Graduate School of Science,

Osaka University
for the degree of Doctor of Science

February, 2024

Abstract

In the study of hypernuclei, an effort is being made to understand the change in nuclear forces caused by the introduction of strange quarks by investigating the forces acting between protons, neutrons, and lambda hyperons. The origin and evolution of matter can be unraveled by understanding the properties of the nuclear force based on quarks. Hypertriton ($^3_\Lambda$H) is the most important nuclide in hypernuclear research. $^3_\Lambda$H is the lightest bound hypernucleus, consisting of a proton, a neutron, and a Λ hyperon. Therefore, $^3_\Lambda$H is one of benchmark nuclei for the hypernuclear physics, and its properties are important for understanding the ΛN interaction. The lifetime and binding energy of $^3_\Lambda$H have been the issues of many experiments and are still matters of discussion. The lifetime of $^3_\Lambda$H was theoretically predicted to be 260 ps based on the physical picture due to the small binding energy, but heavy-ion collision experiments have measured it to be about 140–180 ps, and this inconsistency is called *hypertriton lifetime puzzle*. The exact value of the binding energy has not yet been determined. To solve the puzzle, experiment using the (K^-, π^0) reaction is in progress at J-PARC.

$^3_\Lambda$H is produced by the ^{3}He(K^-, π^0) reaction using a K meson beam with a momentum of 1 GeV/c in the experiment. One unique feature of the experiment is the ability to identify the formation of hypernuclei through the detection of high-energetic gamma-rays from the π^0 decay, even when π^0 cannot be reconstructed by a forward EM calorimeter. A feasibility study with a helium-4 target was performed to determine whether hypernuclei can be identified using the presented experimental method. Then, short production runs was performed to measure the $^3_\Lambda$H production cross section with a helium-3 target as a pilot experiment. In the experiments, the helium-4 target and helium-3 target were irradiated with 9.55×10^9 and 18.2×10^9 K meson beams, respectively. π^- from the mesonic weak decay of $^4_\Lambda$H or $^3_\Lambda$H were measured and π^- momentum spectra were obtained. Mono-momentum peaks due to the two-body decays of $^4_\Lambda$H and $^3_\Lambda$H were observed in the momentum spectra. The numbers of produced hypernuclei were estimated by fitting the signal and background in the π^- momentum spectra. The background mainly comes from decays of hyperons produced by quasi-free processes, and the momentum distribution was reproduced by a Monte-Carlo simulation. The production cross sections of $^4_\Lambda$H and $^3_\Lambda$H by the (K^-, π^0) reaction were estimated as 50.7 ± 2.1 (stat.) $^{+7.8}_{-8.3}$ (syst.) μb and 15.0 ± 2.6 (stat.) $^{+2.4}_{-2.8}$ (syst.) μb, respectively.

Theoretical calculation by Harada *et al* in the framework of the distorted-wave impulse approximation suggests that the production cross section ratio $\sigma_{^3_\Lambda\text{H}}/\sigma_{^4_\Lambda\text{H}}$ in the (K^-, π^0) reaction is sensitive to the binding energy of $^3_\Lambda$H. The ratio $\sigma_{^3_\Lambda\text{H}}/\sigma_{^4_\Lambda\text{H}}$ was estimated to be 0.295 ± 0.053 (stat.) $^{+0.047}_{-0.050}$ (syst.). The binding energy of $^3_\Lambda$H was estimated to be $0.061 ^{+0.028}_{-0.022}$ (stat.)

iv

$^{+0.024}_{-0.021}$ (syst.) MeV from the production cross section ratio with the theoretical analysis of the production cross sections of $^{3}_{\Lambda}$H and $^{4}_{\Lambda}$H. The result suggests that a Λ hyperon is bound quite loosely in $^{3}_{\Lambda}$H.

Contents

List of Figures

List of Tables

Chapter 1

Introduction

1.1 Hypernuclear and strangeness nuclear physics

Nuclear physics is the field of studies of the origin and evolution of matter focusing on nuclei. Most of mass of our visible material world comes from atomic nuclei composed of protons and neutrons bound together by the nuclear force. These protons and neutrons are called nucleons as they are the particles that make up the nucleus. The nuclear force, also referred to as the nucleon-nucleon (NN) interaction, plays a fundamental role in shaping the structure of atomic nuclei and nuclear matter, including neutron stars. This force has been extensively studied for over half a century, particularly through numerous experiments involving proton-proton and neutron-proton scatterings. Several theoretical studies[1, 2, 3] have been conducted to explain the phenomenological nuclear force using extensive experimental data on NN scattering. The interaction between baryons has been found to act as a repulsion at very short ranges (< 1 fm) and as an attraction at middle to long ranges. The exchange of relatively light π mesons describes the long ranges (> 2 fm) by the one-boson-exchange model, while the multi-pion exchange and vector meson exchange such as ρ and ω describe the middle ranges (1–2 fm). Meson exchange model provides a clear explanation for the attractive part of the nuclear force. However, the origins of the short-range repulsion are not yet fully understood. The quark cluster model (QCM) predicts strong repulsive cores due to Pauli blocking between quarks[4]. The QCM model is based on the one-gluon-exchange mechanism between quarks. Since the origin of the nuclear force is the strong interaction between quarks, it is necessary to extend the nuclear force to baryon-baryon interactions, involving different species of quarks, in order to understand the role of quarks in the nuclear force.

Hyperons are members of the nucleon family, which includes strange (s-) quarks. Nucleons are composed of up (u-) and down (d-) quarks. The baryon configuration with the u-, d-, and s-quarks is expressed by the flavor SU(3) symmetry(SU(3)$_f$). Hyperon takes a step further by introducing a new quark flavor, the s-quark, into the system. The s-quarks is introduced as a quantum number called Strangeness (S). The nucleon-hyperon relationship diagram is represented in Fig. 1.1 as a member of a baryon octet in SU(3)$_f$ of spin 1/2 composed of u-, d-, and s-quarks. Several hyperons, which are a part of the same baryon octet, contain at least one strange quark and possess a strangeness quantum number S with values of either -1 or -2.

Among these hyperons, the Λ hyperon is the lightest, followed by the Σ hyperon. In terms of isospin (I), the Σ hyperon has an isospin of 1, whereas the Λ hyperon has an isospin of 0.
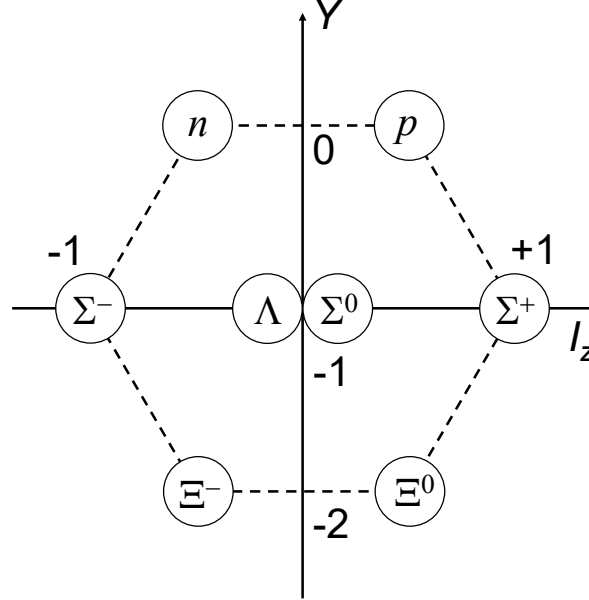
Figure 1.1: Baryon octet is a group of baryons consisting of combinations of three u, d or s quarks with a half spin and a positive parity. I_z and Y represent z component of isospin and hyper charge, respectively.

1.1.1 ΛN interaction

The irreducible representations of the interactions between octet baryons ($8 \otimes 8$) can be decomposed as follows,

$$8 \otimes 8 = 1 \oplus 8_s \oplus 27 \oplus 8_a \oplus 10 \oplus 10^*. \tag{1.1}$$

The first three multiplets in Eq. (1.1) are symmetric and others are antisymmetric under a flavor exchange of two baryons. Relations between the multiplets in the irreducible representations and NN, ΛN, ΣN systems in the isospin basis are summarized in Table 1.1. The NN interactions belong to the (10^*) and (27) multiplets. On the other hand, the ΛN interactions are written with the 10^*, 27, 8_s and 8_a multiplets. The 8_s, 8_a multiplets are not included in the NN interactions, so information about the ΛN interaction extends our understanding of the strong interaction.

Experimental inputs to testing theoretical models of baryon-baryon interactions in two-body system includes the binding energy of few-body system containing hyperon, such as $^3_\Lambda$H, and two-body scattering data between hyperon and proton. The two-body scattering experiment is an important method to derive the baryon-baryon interactions, but the ΛN scattering data are limited because of the short lifetime of Λ hyperon (roughly 260 ps[5]) and its neutral electric

charge. Therefore, most of our knowledge for the ΛN interactions are obtained from the study of Λ hypernuclei, in which a Λ is bound to a nuclear system due to the attractive ΛN interaction.

Table 1.1: NN, ΛN and ΣN interactions written with multiplets in the irreducible representations of interaction between octet baryons.

B-B	Isospin(I)	flavor symmetric	flavor anti-symmetric
NN	$I = 0$	-	$(\mathbf{10^*})$
NN	$I = 1$	$(\mathbf{27})$	-
ΛN	$I=1/2$	$\frac{1}{\sqrt{10}}((\mathbf{8}_s)+3(\mathbf{27}))$	$\frac{1}{\sqrt{2}}(-(\mathbf{8}_a)+(\mathbf{10^*}))$
ΣN	$I=1/2$	$\frac{1}{\sqrt{10}}(3(\mathbf{8}_s)-(\mathbf{27}))$	$\frac{1}{\sqrt{2}}((\mathbf{8}_a)+(\mathbf{10^*}))$
ΣN	$I=3/2$	$(\mathbf{27})$	$(\mathbf{10})$

1.1.2 Λ hypernuclei

Hypernuclei are nuclei that contain hyperons. Spectroscopy and emulsion experiments have been used to observe and study approximately forty species of hypernuclei[6]. Figure 1.2 shows a nuclear chart of the Λ hypernuclei. Thus, considering the number of quarks with flavor quantum numbers as their respective axes, the concept of the atomic nucleus can be extended as a quantum many-body system of hadrons in a multidimensional flavor quantum number space. The physical quantity of $^3_\Lambda$H, the lightest hypernucleus, is important because it is the benchmark for understanding the ΛN interaction.
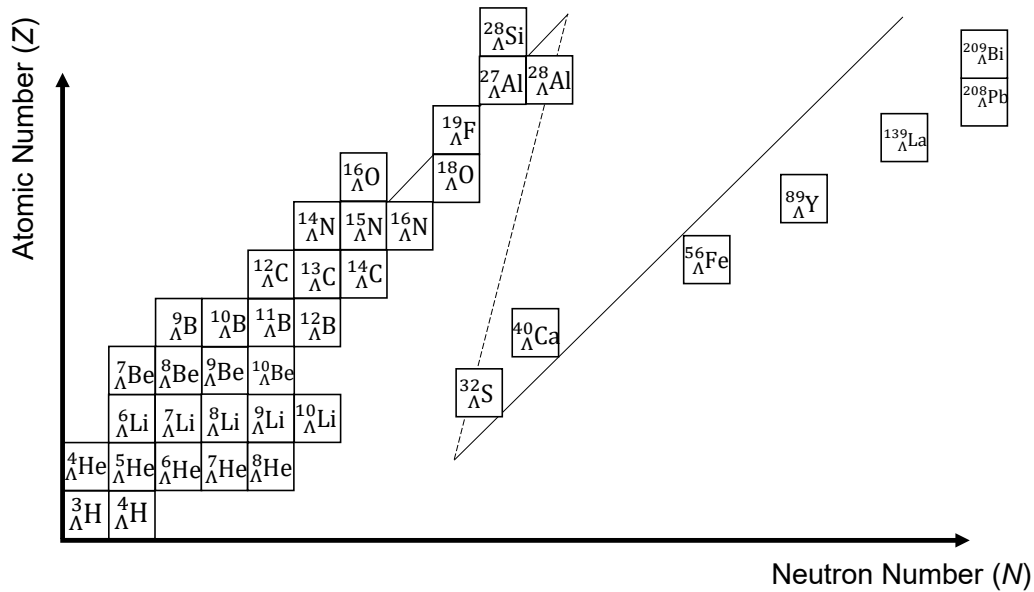
Figure 1.2: A chart of Λ hypernuclei.

1.1.3 Decay of Λ hypernuclei

A Λ hypernucleus decays due to the weak interaction with a lifetime of roughly $100 - 200$ ps. Hypernucleus exhibits two modes of weak decay: mesonic weak decay (MWD), which involves the emission of pions, and non-mesonic weak decay (NMWD), which does not involve the emission of pions. MWD is a decay mode similar to the free decay of Λ, such as $\Lambda \rightarrow p + \pi^-$ and $\Lambda \rightarrow n + \pi^0$. NMWD is a unique decay mode in the hypernuclear medium that arises from weak interactions between Λ and nucleons, such as $\Lambda + N \rightarrow N + N$. In heavy hypernuclei A$\geq$12, MWD is suppressed due to the Pauli exclusion principle. This is because the emitted nucleon momentum, which is approximately 100 MeV/c, is much smaller than the nucleon fermi momentum in a nucleus (approximately 250 MeV/c). As a result, NMWD dominates the decay, where the emitted nucleon momentum in NMWD is approximately 400 MeV/c. The lifetime of medium and heavy hypernuclei remains constant at approximately 200 ps, irrespective of the mass number, due to the short effective distance of the ΛN interaction [7].

1.1.4 Property of hypernuclei

This section describes the property of $^3_\Lambda$H and $^4_\Lambda$H. $^3_\Lambda$H consists of a proton, a neutron and a Λ hyperon. The $^3_\Lambda$H system involves the binding of a Λ hyperon to the core nucleus, specifically the deuteron (d). The spin and party of $^3_\Lambda$H is $J^P = 1/2^+$ [8]. The isospin of $^3_\Lambda$H is $I = 0$. $^4_\Lambda$H consists of a proton, two neutrons and a Λ hyperon. The $^4_\Lambda$H system involves the binding of a Λ hyperon to the core nucleus, specifically the triton (^{3}H). The spin and party of $^4_\Lambda$H is $J^P = 0^+$ [8, 9]. The isospin of $^4_\Lambda$H is $I = 1/2$. Table 1.2 summarize the property of $^3_\Lambda$H and $^4_\Lambda$H. Table 1.3 and Table 1.4 summarize the possible MWD mode of $^3_\Lambda$H and $^4_\Lambda$H, respectively. It should be noted that not all decay modes noted in the table have been observed.

Table 1.2: The property of $^3_\Lambda$H and $^4_\Lambda$H.

	$^3_\Lambda$H	$^4_\Lambda$H
component	d + Λ	^{3}H + Λ
spin/party(J^P)	$1/2^+$	0^+
isospin (I)	0	1/2

Table 1.3: The MWD mode of $^3_\Lambda$H.

	π^- decay	π^0 decay
2-body	$^3_\Lambda$H $\rightarrow$ ^{3}He + π^-	$^3_\Lambda$H $\rightarrow$ t + π^0
3-body	$^3_\Lambda$H $\rightarrow$ d + p + π^-	$^3_\Lambda$H $\rightarrow$ d + n + π^0
4-body	$^3_\Lambda$H $\rightarrow$ p + n + p + π^-	$^3_\Lambda$H $\rightarrow$ p + n + n + π^0

Table 1.4: The MWD mode of $^4_\Lambda$H.

	π^- decay	π^0 decay
2-body	$^4_\Lambda$H $\to$ ^{4}He + π^-	
3-body	$^4_\Lambda$H $\to$ t + p + π^- $^4_\Lambda$H $\to$ ^{3}He + n + π^- $^4_\Lambda$H $\to$ d + d + π^-	$^4_\Lambda$H $\to$ t + n + π^0
4-body	$^4_\Lambda$H $\to$ d + n + p + π^-	$^4_\Lambda$H $\to$ d + n + n + π^0
5-body	$^4_\Lambda$H $\to$ p + n + n + p + π^-	$^4_\Lambda$H $\to$ p + n + n + n + π^0

1.2 Hypertriton lifetime puzzle

The hypertriton ($^3_\Lambda$H), being the lightest hypernucleus consisting of a proton, a neutron and a Λ hyperon, holds a pivotal position in the realm of the hypernuclear physics. Its properties, including spin, lifetime and binding energy, constitute essential information for our understanding of the ΛN interaction. The results of the binding energy and lifetime measurements of $^3_\Lambda$H so far are summarized in Fig. 1.3.
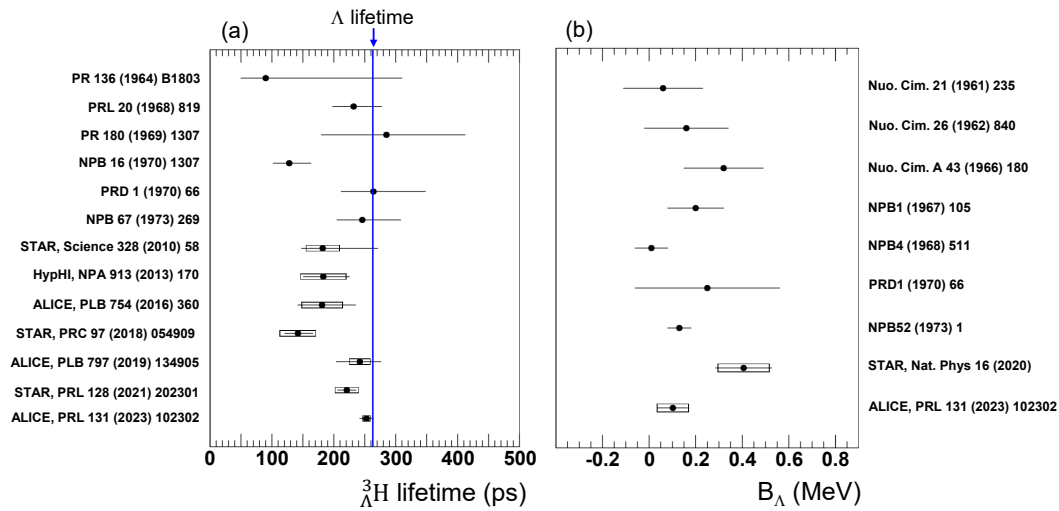
Figure 1.3: Summary of the $^3_\Lambda$H lifetime (a) [10, 11, 12, 13, 14, 15, 16, 17, 18, 19, 20, 21, 22] and the binding energy B_Λ (b) [23, 24, 25, 26, 27, 14, 28, 29, 22] measurements obtained with different experimental techniques. The horizontal error bars and boxes are the statistical and systematic uncertainties, respectively.

The binding energy of $^3_\Lambda$H has been estimated to be 0.13 ± 0.05 MeV based on results of nuclear emulsion experiments through 1960s and 1970s[28]. From the small binding energy, it can be viewed as a simple two-body system of lambda hyperons and deuterons. The spatial

extension of the system could potentially be estimated by the root mean square radius,

$$\sqrt{\langle r^2 \rangle} = \frac{\hbar}{\sqrt{4\mu B_\Lambda}}, \tag{1.2}$$

$$\mu = \frac{m_\Lambda m_d}{m_\Lambda + m_d}, \tag{1.3}$$

where μ is the reduced mass, B_Λ is the binding energy of Λ hyperon[30, 31]. Figure 1.4 shows the result of the calculation of the Eq. (1.2). According to the relational equation, it can be inferred that the distance between the lambda hyperon and deuterium is approximately 10 fm. Because the influence of deuteron is very small, the lifetime of $^3_\Lambda$H was expected to be close
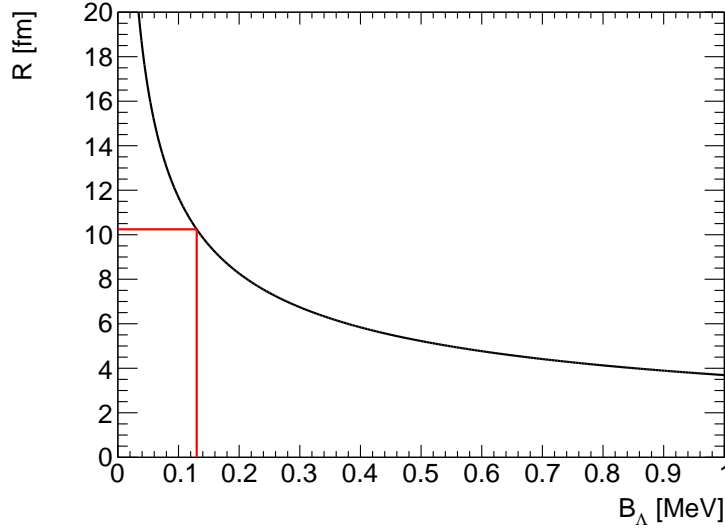
Figure 1.4: The relationship between the binding energy and the root mean square radius between the Λ hyperon and deuteron based on Eq (1.2). The measurement of the emulsion indicates a binding energy of 0.13 MeV for the red line, with a root mean square radius of 10.2 fm.

to the lifetime of a free Λ hyperon ($\tau_\Lambda = 263$ ps). In the 1960s, lifetime measurements using nuclear emulsions and bubble chambers confirmed $\tau = 246^{+30}_{-25}$ ps, which is consistent with the physical picture of the $^3_\Lambda$H. However, in the 2010s, a much shorter lifetime, 166^{+25}_{-23} ps, than that of a free Λ was reported in experiments using heavy-ion reactions, which contradicts the previously believed physical picture and has been called *hypertriton lifetime puzzle*. Very recently, the $^3_\Lambda$H lifetime results reported $221 \pm 15(\text{stat.}) \pm 19(\text{syst.})$ ps from the STAR collaboration and $253 \pm 11(\text{stat.}) \pm 6(\text{syst.})$ ps from the ALICE collaboration in heavy ion collision experiments, whose results contradicts to its own previous one by roughly 3σ.

Binding energies have also been measured by these experiments. The $^3_\Lambda$H binding energy was reported $0.41 \pm 0.12(\text{stat.}) \pm 0.11(\text{syst.})$ MeV from the STAR collaboration and $0.102 \pm 0.063(\text{stat.}) \pm 0.067(\text{syst.})$ MeV from the ALICE collaboration. These values are contradicts to each other indicating that the value of the binding energy has not been determined

unambiguously, yet. Therefore, it is necessary to determine complementary values for both life-time and binding energy by deriving them by a method different from the heavy-ion collision experiments.

1.2.1 Experimental studies

Nuclear emulsion and bubble chamber experiments

Since the 1960s, lifetimes[10, 11, 12, 13, 14, 15] and binding energies[23, 24, 25, 26, 27, 14, 28] of light hypernuclei have been measured in nuclear emulsion and bubble chamber experiments. Hypernuclei were produced by stopped K^- mesons in nuclear emulsions and bubble chambers. In nuclear emulsions and bubble chambers, one could see tracks of the produced hypernuclei and particles from their decays as a photographic image. Momentum and energy associated to a track could be estimated from the length, the image density and the decay angle of the tracks. By combining these information, one could identify the particle type. The lifetime was derived from the decay distances, which are Lorentz-corrected from the measured the momentum. The binding energy was derived by estimating the total kinetic energy of the daughter particles and component with the rest mass of the composing constituients. Using this approach, the lifetime of $^3_\Lambda$H was found to be consistent with the lifetime of a free Λ particle, and the binding energy was found to be 0.13 ± 0.05 MeV by combining events measured in previous emulsions.

HypHI experiment

The HypHI experiment at the GSI Helmholtz Centre reported the $^3_\Lambda$H lifetime measured by using heavy-ion beams[17]. In 2013, using the invariant mass method, the spectroscopy of hypernuclear products of ^{6}Li projectiles on a carbon target at 2 A GeV was performed. Signals of $^3_\Lambda$H was observed for final states as a ^{3}He$+\pi^-$. By analyzing the proper decay time estimated from secondary vertex position and particle momenta with the unbinned maximum likelihood fitting method, the lifetime value was deduced to be 183^{+42}_{-32}(stat.) ± 37(syst.) ps for $^3_\Lambda$H.

ALICE experiment

The ALICE collaboration at LHC reported three values of the $^3_\Lambda$H lifetime. The first result was reported in 2016[18]. The ALICE experiment at LHC measured the production of the hypertriton $^3_\Lambda$H and anti-hypertriton $^3_\Lambda\overline{\text{H}}$ for the first time in Pb–Pb collisions at $\sqrt{S_{NN}} = 2.76$ TeV. $^3_\Lambda$H could be identified via the invariant mass of its 2-body decay products, ^{3}He$+\pi^-$. They measured dN/dL distribution, the number of events per decay distance and used an exponential fit to determine the lifetime. The lifetime value was 181^{+54}_{-39}(stat.) ± 33(syst.) ps.

The second result was reported in 2018[20]. An improved value for the lifetime of $^3_\Lambda$H and $^3_\Lambda\overline{\text{H}}$ has been reported using the data sample of Pb-Pb collisions at $\sqrt{S_{NN}} = 5.02$ TeV. The method for deriving the lifetimes is the same as that of the first result, but due to the high statistics and quality data samples and the good tracking and particle identification of the ALICE detector, the accuracy of the $^3_\Lambda$H lifetime is better. The lifetime value was 240^{+40}_{-31}(stat.) ± 18(syst.) ps.

The third result was reported in 2023[22]. The most precise measurements to date of the $^{3}_{\Lambda}\text{H}$ lifetimes and the Λ binding energy B_{Λ} are reported from the data sample of Pb-Pb collisions at $\sqrt{S_{NN}}$ = 5.02 TeV. The data sample used in the report has even more statistics than the data in 2018. In addition, a new analysis technique, supervised machine learning, is used for signal selection. This has significantly improved the accuracy of the $^{3}_{\Lambda}\text{H}$ lifetime. The lifetime value was $253\pm11(\text{stat.})\pm6(\text{syst.})$ ps. In the report, the binding energy of $^{3}_{\Lambda}\text{H}$ was also estimated. The B_{Λ} value and its statistical uncertainty are obtained from the average of the values measured in each decay length interval weighted on their statistical uncertainties. The value of the binding energy was $102\pm63(\text{stat.})\pm67(\text{syst.})$ keV.

STAR experiment

The STAR experiment reported three papers on lifetime and one on binding energy. The first result was reported in 2010[16]. The experiment was carried out by the STAR collaboration at RHIC. STAR collected Au-Au collision data at $\sqrt{S_{NN}}$ = 200 GeV. They used $^{3}_{\Lambda}\text{H} \rightarrow {}^{3}\text{He} + \pi^{-}$ and $^{3}_{\Lambda}\overline{\text{H}} \rightarrow {}^{3}\overline{\text{He}} + \pi^{+}$ decay modes to reconstruct $^{3}_{\Lambda}\text{H}$ and $^{3}_{\Lambda}\overline{\text{H}}$, respectively. They measured $dN/d(ct)$ distribution and used an exponential fit to determine the lifetime. The lifetime value was $182^{+89}_{-45}(\text{stat.})\pm27(\text{syst.})$ ps.

The second result was reported in 2018[19]. The improved measurement of the $^{3}_{\Lambda}\text{H}$ lifetime was reported in 2018. The STAR collected Au+Au collision data over a broad range of energies, and used $^{3}_{\Lambda}\text{H} \rightarrow {}^{3}\text{He} + \pi^{-}$ and $^{3}_{\Lambda}\text{H} \rightarrow \text{d} + \text{p} + \pi^{-}$ to reconstruct $^{3}_{\Lambda}\text{H}$. For the two-body decay channel analysis, they used data from six different collosion energies, $\sqrt{S_{NN}}$ = 7.7, 11.5, 19.6, 27, 39, and 200 GeV; for the three-body decay analysis, they had three beam energies, $\sqrt{S_{NN}}$ = 27, 39, and 200 GeV. A minimum χ^{2} estimation was used to determine the lifetime of $\tau = 142^{+24}_{-21}(\text{stat.})\pm29(\text{syst.})$ ps.

The third result was reported in 2022[21]. They report the $^{3}_{\Lambda}\text{H}$ lifetime obtained from data samples of Au-Au collisions at $\sqrt{S_{NN}}$ = 3.0 GeV and 7.2 GeV. The data were collected in 2018, using the fixed-target (FXT) configuration. In the FXT configuration a single beam provided by RHIC impinges on a gold target of thickness 0.25 mm located at 201 cm away from the center of the STAR detector. In the same way, they measured $dN/d(ct)$ distribution and used an exponential fit to determine the lifetime. The lifetime value was $221\pm15(\text{stat.})\pm19(\text{syst.})$ ps.

The STAR Collaboration also reports on binding energy[29]. They use Au-Au collision data at $\sqrt{S_{NN}}$ = 200 GeV to derive the binding energy of $^{3}_{\Lambda}\text{H}$ and $^{3}_{\Lambda}\overline{\text{H}}$. The Λ binding energy, B_{Λ}, for $^{3}_{\Lambda}\text{H}$ and $^{3}_{\Lambda}\overline{\text{H}}$ is calculated using the mass measurement. The value of the binding energy was $0.41\pm0.12(\text{stat.})\pm0.11(\text{syst.})$ MeV.

1.2.2 Theoretical studies

The study of the lifetime and binding energy of $^{3}_{\Lambda}\text{H}$, a hypernucleus, has been the subject of significant theoretical research over the years. Various researchers have employed different methods and models to derive their predictions. In 1966, Dalitz and Rayet[32] considered phase space factors and the Pauli principle, including corrections for final state pion scattering and the non-mesonic weak decay channel, leading to a lifetime prediction of 256 ps. Congleton[33] used

updated NN and YN interactions to predict $\tau = 232$ ps. In 1998, Kamada *et al.*[34] calculated the rigorous determination of the hypernuclear wave function and the scattering states of the three nucleons, resulting in a lifetime of 256 ps, which is the closest to that of a free Λ particle. In 2019, Garcilazo and Gal[35] performed calculations using a wave function from the three-body Faddeev equations, with added final-state pion interactions, arriving at $\tau = 213$ ps. In 2020, pionless Effective Field Theory (EFT) proposed values of 265 ps at $B_\Lambda = 130$ keV and 268 ps at $B_\Lambda = 410$ keV[36]. In the same year, predictions were made using Chiral Effective Field Theory (χEFT) with varying results[37]. The predicted lifetimes were $\tau = 234 \pm 27$ ps for $B_\Lambda = 69$ keV, $\tau = 190 \pm 22$ ps for $B_\Lambda = 135$ keV, and $\tau = 163 \pm 18$ ps for $B_\Lambda = 410$ keV.

Regarding the binding energy (B_Λ) for $^3_\Lambda$H, Dalitz's 1972 calculation using a simple model suggested $B_\Lambda = 0.1$ MeV[38]. Recent calculations have yielded different results by Fujiwara *et al.*'s 2008 study using SU(6) quark model baryon-baryon interactions, which calculated $B_\Lambda = 0.289$ MeV. Additionally, Lonardoni *et al.*'s 2017 research[39], which used the Auxiliary Field Diffusion Monte Carlo (AFDMC) method, resulted in a B_Λ value of 0.23 MeV. In their 2020 study, Haidenbauer *et al.*[40] proposed a binding energy range of 0.046 MeV to 0.162 MeV for $^3_\Lambda$H, considering ΛN and ΣN interactions at next-to-leading order in SU(3) chiral effective field theory.

1.3 J-PARC E73 experiment

The J-PARC E73 experiment[41] was proposed to solve the $^3_\Lambda$H lifetime puzzle by measuring the lifetime of $^3_\Lambda$H in a different method than heavy-ion based experiments. In both nuclear emulsion experiment and the heavy ion collision experiment, the lifetime was calculated from the flight length when $^3_\Lambda$H decays. In the E73 experiment, on the other hand, the lifetime is obtained by directly measuring the time until $^3_\Lambda$H decays. To do that, I introduced a new method by using the (K^-, π^0) reaction, in which a proton is converted into a Λ hyperon using a K^- meson beam at 1 GeV/c.

1.3.1 Method of hypernucleus formation

The hypernucleus formation requires the successful completion of two processes: the production of hyperons through the interaction of incident particles with nucleons, and the subsequent binding of these hyperons to nuclei. The reaction probabilities of both processes are determined by the elementary process cross section and the reaction probability, respectively. The elementary process cross section is dependent on the momentum of the beam particles used in the production reaction, as well as the scattering angle of the product particles and the momentum transfer of the reaction. Three major reactions have been used to produce hypernuclei: (K^-, π^-) reaction, (π^+, K^+) reaction, and (γ^*, K^+) reaction. The (K^-, π^-) reaction replaces a d-quark in the neutron with an s-quark, and the target neutron is converted to a Λ hyperon. The Λ hyperon production cross sections are large ($\sim$mb/sr) compared to that of other reactions. For the K^- induced reactions, it can be further divided into *stop* and *in-flight* setup. In the case K^- is absorbed by the target nucleus at rest and reacts at the surface of a nucleus with a recoil momentum of roughly 250 MeV/c, it is called by a specific name the (K^-_{stop}, π^-) reaction. On

the other hand, the in-flight(K^-,π^-) reaction has characteristic of a low momentum transfer. In the case of K^- beam momentum at 500 MeV/c, the reaction gives no momentum transfer to Λ (Fig. 1.5); the momentum is therefore called the magic momentum. Furthermore, even at finite angles, the recoil momentum is kept low with a beam momentum of about 1 GeV/c. At 1 GeV/c momentum, the hypernuclei produced are mostly in the substitutional state, where the produced Λ remains in the same orbit as the neutron. This means that hypernuclei produced in the $(K^-\pi^-)$ reaction are mostly spin non-flip states. The (π^+,K^+) and the (γ^*,K^+) reactions produce a pair of $s\bar{s}$ quarks. These reactions are needed to bring energies from outside to the systems, for example a π^+ energy threshold of $n(\pi^+,K^+)\Lambda$ reaction is 911 MeV. These reactions are useful to study heavy hypernuclei because highly excited or deeply bound hypernuclei can be produced thanks to larger recoil momenta ($300 - 400$ MeV/c). On the other hand, the Λ production cross section in the (π^+,K^+) reaction is smaller (roughly 100 μb/sr) than that of the (K^-,π^-) reaction, and the cross section in the (γ,K^+) reaction is further smaller (roughly 100 nb/sr).
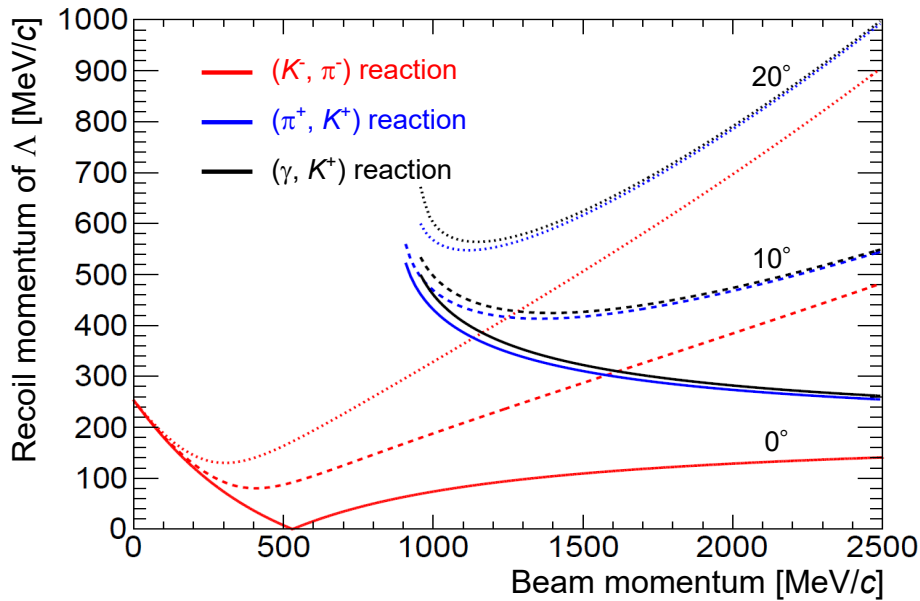
Figure 1.5: The momentum transfer from beam K^- to Λ as a function of the beam momentum. There are nine lines in combination of three reactions (red:(K^-,π^-), blue:(π^+,K^+) and black:(γ,K^+)) and three different opening angles between beam and scattering particle in the laboratory system ($0°$: solid line, $10°$: dashed line and $20°$: dotted line). In the (K^-,π^-) reaction, the recoil momenta have minimum values around 500 MeV/c. In particular, at the forward angle ($0°$) in the (K^-,π^-) reaction, the magic momentum, at where the recoil Λ momentum is zero, exists around 500 MeV/c.

1.3.2 Experimental principle of J-PARC E73

In the J-PARC E73 experiment, hypernuclei are produced by the in-flight (K^-, π^0) reaction using a 1 GeV/c K^- meson beam. The (K^-, π^0) reaction replaces a u-quark in the neutron with an s-quark, and the target proton is converted to a Λ hyperon. Figure 1.6 shows the schematic drawing of (K^-, π^0) reaction. Since the (K^-, π^0) reaction is kinetically identical to the (K^-, π^-) reaction, Λ hyperons can be produced with small recoil momenta. The optimal momentum for hypernucleus formation is 0.5 GeV/c, but it is challenging to prepare K^- beam with such low momentum due to K^- decay during transportation. Furthermore, it is important to note that the intensity of the K^- beam increases with momentum. Additionally, the production cross section of the Λ elementary process reaches a maximum of roughly 5.0 mb/sr at 0.8 GeV/c and decreases as momentum increases, while the Σ cross section increases[42]. To take into account the K^- beam intensity, hyperon production cross section, the ratio of Λ to Σ, and the Λ recoil momentum, a momentum of 1 GeV/c is utilized. Furthermore, it is expected that the hypernuclei produced are dominated by the ground state.
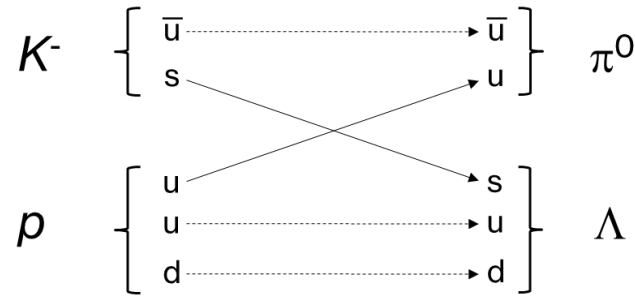
Figure 1.6: The schematic figures of (K^-, π^0) reaction for Λ production.

The reason why hypernucleus spectroscopy by the (K^-, π^0) reaction has been difficult in the past is because of the difficulty in detecting π^0 meson with a good momentum resolution. There was a project at BNL called Neutral Meson Spectrometer to measure the π^0 momentum by measuring energies and an opening angle of two gamma-rays from the $\pi^0 \to \gamma\gamma$ decay[43]. The missing mass resolution was not good, which is not very attractive to identify hypernuclei.

In the J-PARC E73 experiment, π^0 is not reconstituted. It is noteworthy that in the (K^-, π^0) reaction using 1 GeV/c K^- meson beam, the π^0 emitted forward with about 0.9 GeV/c momentum. For π^0 with momentum of about 0.9 GeV/c and $\theta_{\pi^0}=0°$, the opening angle between decay gamma-rays is centered at $\pm 8°$. One of the two gamma-rays decayed from π^0 can be measured with an electromagnetic calorimeter placed in the forward direction. The hypernuclear events are tagged by the gamma-ray from the π^0 decay with higher energies (> 450 MeV). Since the produced $^3_\Lambda$H has low momentum and stopped quickly in the target (t < 10 ps), the identification of the hypernucleus can be accomplished by selecting the π^- meson with mono-momentum resulting from the two-body mesonic weak decay $^3_\Lambda$H $\to^3$ He $+ \pi^-$. The π^- meson is measured by detectors surrounding the target. The mesonic decay time of $^3_\Lambda$H can be obtained by subtract-

ing from the measured flight time to the calculated flight time. Lifetime is derived by fitting the decay time spectrum by an exponential distribution convoluted with a time response function.

1.3.3   Theoretical prediction of hypernuclear production cross section

The report by Harada and Hirabayashi investigates the production cross sections of hypernuclei $^3_\Lambda$H and $^4_\Lambda$H in (K^-, π^0) reaction[44]. The employed method involves the distorted-wave impulse approximation (DWIA) combined with optimal Fermi-averaging $K^- p \to \Lambda \pi^0$ t matrix. Fermi-averaging is incorporated to consider the nucleons motion within the nucleus. The transition density distribution is a crucial theoretical calculation. It is expressed as the superposition of the core-particle relative wavefunction in the produced hypernucleus and the core-nucleon relative wavefunction of the target nucleus ^{3,4}He. By examining the transition density distribution, it is possible to evaluate it in terms of the particle's wavefunction. If the uncertainty of the elementary process cross sections in the medium can be minimized by comparing the differential cross sections of hypernuclei, the differences in shape factors can directly be observed. In other words, by reducing the uncertainty of the reaction process and comparing the quantities related to the $^3_\Lambda$H and $^4_\Lambda$H wavefunctions, their differences become more apparent. A comparative analysis was also conducted for the ^{3,4}He$(e, e'K^+)$ reaction[45]. It is suggested that the production cross section ratio $\sigma_{^3_\Lambda \text{H}}/\sigma_{^4_\Lambda \text{H}}$ depends on the magnitude of the binding energy of $^3_\Lambda$H.

In this thesis, the data for the (K^-, π^0) reaction with a helium-4 target and the production cross section measurement of $^3_\Lambda$H with a helium-3 target, which were conducted as a pilot experiment of J-PARC E73, are utilized. The production cross sections of $^4_\Lambda$H and $^3_\Lambda$H by the (K^-, π^0) reaction are then derived. This information is important for examining the production mechanism and the structure of $^{3,4}_\Lambda$H by the (K^-, π^0) reactions at $p_{K^-} = 1.0$ GeV/c. It is suggested that the production cross section ratio $\sigma_{^3_\Lambda \text{H}}/\sigma_{^4_\Lambda \text{H}}$ is dependent on the binding energy magnitude of $^3_\Lambda$H. Because the same setup was used to acquire data excpept that the target is different in this experiment, the cross section ratio can be derived with a small systematic error. The magnitude of the $^3_\Lambda$H binding energy will be discussed by comparing the experimentally derived production cross section ratio with theoretical calculations.

Chapter 2 describes the experimental setup and run conditions. Chapters 3 and 4 describe the analysis procedures and experimental results. Finally, the $^3_\Lambda$H binding energy is discussed using the experimental result in Chap. 5. A summary of this thesis is given in Chap. 6.

Chapter 2

Experimental Apparatus

2.1 J-PARC

J-PARC (Japan Proton Accelerator Research Complex)[46], located in Tokai, is a group of proton accelerators and experimental facilities for cutting-edge research in a wide range of fields including particle physics, nuclear physics, materials science, life science, and atomic energy. J-PARC is designed around the use of secondary particles generated by a world-leading 1 MW class primary proton beam. J-PARC is made up of three proton accelerators: an H$^-$ linear accelerator that serves as the initial injector, a 3 GeV rapid-cycling synchrotron (RCS), and a main ring (MR). RCS functions as both a booster to MR and a provider of a 3 GeV proton beam to the Material and Life Science Facility (MLF). MLF is dedicated to enhancing the fields of material and life sciences through the use of pulsed neutron and muon beams. MR, currently operating at 30 GeV, supplies a fast extracted beam (FX) for producing neutrino beams directed towards Kamioka. MR provides also a slow extracted beam (SX) to the Hadron Experimental Facility (HEF), where a variety of particle and nuclear physics experiments are conducted using primary proton beams and secondary beams of pions, kaons, and antiprotons.

2.1.1 SX beam to HEF

During the SX mode in MR, the beam is gradually extracted by incrementally shaving off portions of the bundled beam, while the rest of the beam continues to circulate within MR[47]. This process results in a beam spill duration of around 2 seconds, occurring within a cycle that repeats every 5.2 seconds. In the context of this experiment, the SX beam intensity ranged between 50 and 65 kW. A spill duty factor indicating a uniformity of the time structure of the extracted beam is defined as

$$Spill\ Duty\ Factor = \frac{\left[\int_0^T I(t)dt\right]^2}{\int_0^T dt \int_0^T I^2(t)dt}, \tag{2.1}$$

where $I(t)$ is beam spill intensity and T is extraction time range. The spill duty factor is 50–60 % in the current experiment. This is one of the main issues of the slow extraction of the J-PARC

13

main ring due to a spike-like time structure of the extracted beam induced by the large ripples of the magnet power supplies on horizontal betatron tune[48]. The operational parameters for the SX beam as they were in May 2021 are detailed in Table 2.1.

Table 2.1: An overview of the typical operating conditions for the slow extraction (SX) beam in May 2021.

Primary beam energy	30 GeV
Primary beam power	59.8 kW
Protons per spill	6.5×10^{13}
Repetition cycle	5.2 s
Spill Length	2 s
Spill duty factor	50–60 %
Spill extraction efficiency	99.5 %

2.2   K1.8BR beam line in the hadron experimental facility

The primary proton beam is directed towards a production target, designated T1, within the hadron experimental facility (HEF). The experiment involves a T1 target consisting of two gold blocks stacked on top of each other. Each block measures 15 mm in width, 6 mm in height, and 66 mm in length, resulting in a total height of 12 mm. The beam is positioned at the center of the target and has a width of $\pm$ 3 mm. Secondary particles generated at T1 are then directed into various beam lines. The current experiment is performed at the K1.8BR beam line, situated on the north side of HEF. K1.8BR is a shorter branch of the K1.8 beam line, extending 31.3 meters from T1 to its final focus point (FF), making it ideal for producing low-momentum beams up to 1.2 GeV/*c*. Figure 2.1 illustrates the K1.8BR beam line layout, and Table 2.2 shows its parameters. For this experiment, the beam momentum is set at 1 GeV/*c*. The beam line is divided into three sections: the front-end (D1-D2), mass separation (IF-MS1), and beam analyzer (D3-FF). The front-end section extracts secondary particles from T1, using an extraction angle of 6 degrees to maximize the kaon production, as suggested by the Sanford-Wang formula. Mass separation is efficiently achieved with a combination of two vertical slits, an electrostatic separator (ES1), and correction magnets. At the entrance of the mass separation section , the secondary beam is vertically focused, and an IF-V slit adjusts the beam size while filtering out decay particles from *cloud pions*. The 6-meter-long ES1 then vertically separates particle trajectories based on their mass, using a 40 kV/cm electric field. A vertical slit (MS1) and two steering magnets (CM1 and CM2) allow only particles of a specific mass to pass. Two horizontal slits, IF-H and MOM, are positioned where the optics are dispersive. After D3 magnet, an SQDQD magnet system concentrates the beam onto the experimental target at FF of the K1.8BR beam line. The final dipole magnet, D5, functions as a beam momentum analyzer. Figure 2.2 displays the first-order beam envelope as calculated by the TRANSPORT code.

D: dipole magnet
Q: quadrupole magnet
S: sextupole magnet
O: octupole magnet
T1: production target
IF: intermediate focus
MS: mass slit
ES: electrostatic separator
CM: correction magnet
FF: final focus
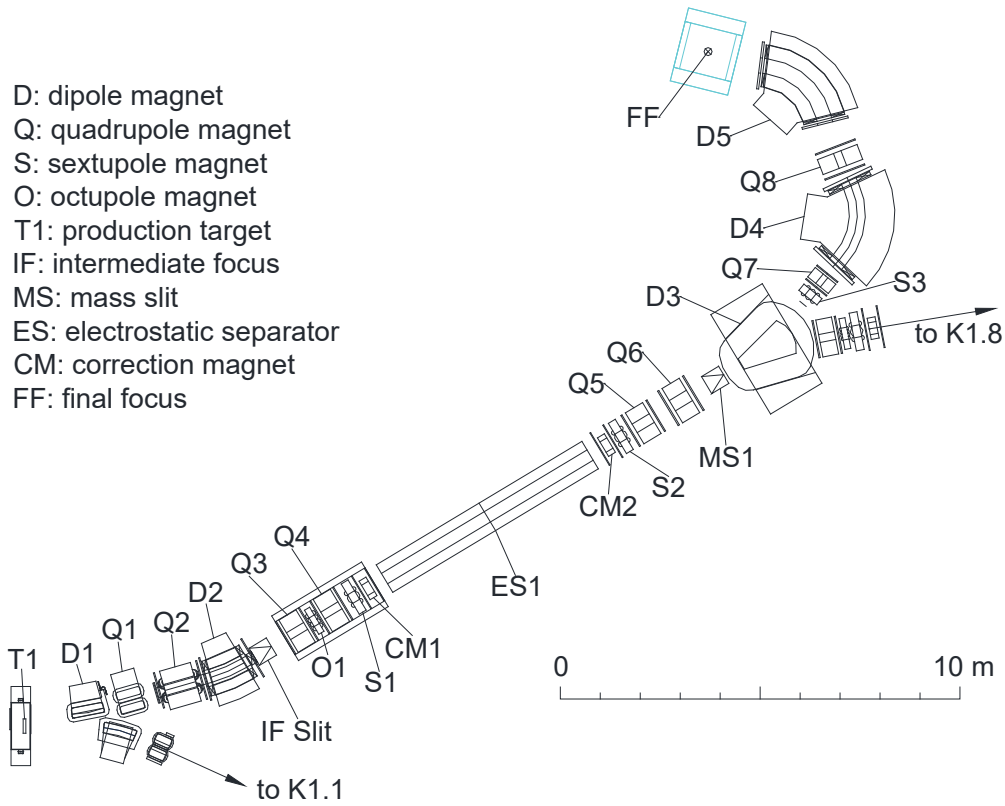
Figure 2.1: Schematic drawing of K1.8BR beam line in the J-PARC hadron experimental facility[49].

Table 2.2: Parameters of K1.8BR beam line.

Production target	Au (50% loss)
Extraction Angle	$6°$
Momentum range	1.2 GeV/c max.
Acceptance	2.0 msr · %
Momentum bite	$± 3$ %
Beam Line Length (T1-FF)	31.3 m

2.2.1 Kaon beam tuning

To optimize the 1 GeV/c kaon beam, my focus was on maximizing kaon intensity at the experimental target while keeping pion levels within acceptable limits. Online triggers were set up to identify kaons. The settings of ES1, CM1, and CM2 were fine-tuned to enhance kaon intensity. The positions of the two vertical slits, IF-V and MS1, were adjusted to alter the vertical beam center. Additionally, the D3, D4, and D5 magnets were adjusted for horizontal beam optimization, along with a more precise setting for the momentum slit. The quadruple magnets, ranging from Q1 to Q8, were also scanned to boost kaon yield and refine the beam focus at FF. The final
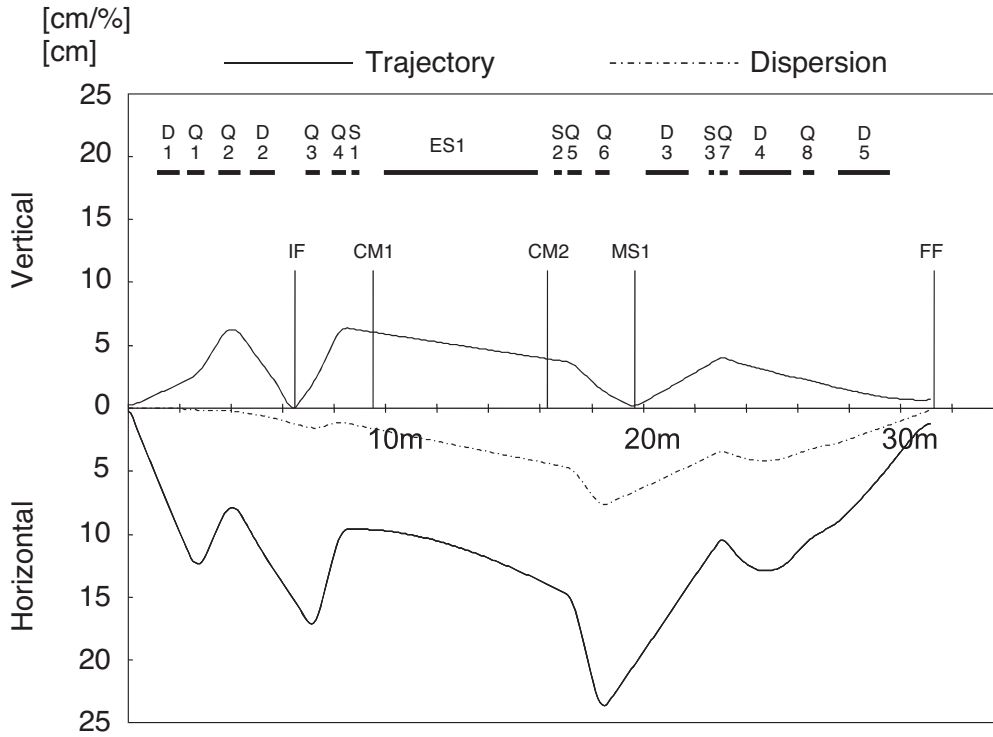
Figure 2.2: First-order beam envelope of the J-PARC K1.8BR beam line[50].

step involved adjusting the openings of two vertical slits (IF-V and MS1) and two horizontal slits (IF-H and MOM), balancing the intensity ratio of kaons to pions (K/π) and the overall beam intensity. Typically, the intensity of the 1 GeV/c kaon beam at FF reached 2.5×10^5 per spill, with a K^-/π^- ratio of approximately 0.37. The optimal settings for the magnets and slits for the 1 GeV/c kaon beam are detailed in Table 2.3 for the slits and Table 2.4 for the magnets.

Table 2.3: Optimized slit settings. All in mm unit.

IF-H	Left: 110	Right: -110
IF-V	Up: 2.2	Down: -1.8
MS1	Up: 5.45	Down: -0.75
MOM	Left: 160.0	Right: -110.0

2.2.2   K1.8BR spectrometer system

The spectrometer consists of a beam line spectrometer, a cylindrical detectors system surrounding the target cell at FF to detect the decay particles from the target region, the liquid helium target system and a forward calorimeter. Details of each component will be described in the following sections.

Table 2.4: Parameters of the beam line magnets. The D5 field is a typical monitored value. Other field values are interpolations of measured points.

Element	J-PARC designation	Gap or bore/2 (cm)	Effective length (cm)	Bend (deg)	Current (A)	Field at pole (kG)
D1	5C216SMIC	8	90.05	10	-369	-6.654
Q1	NQ312MIC	8	67.84		-357	-3.075
Q2	Q416MIC	10	87.04		-668	3.872
D2	8D218SMIC	15	99.65	15	-698	-8.7673
IF-H	Movable horizontal slit for acceptance control					
IF-V	Movable vertical slit, $(y|\phi)=0$					
Q3	Q410	10	54.72		-679	-4.108
O1	O503	12.5	15		-15	-0.29
Q4	Q410	10	54.72		-776	4.692
S1	SX504	12.5	27.6		-42	-0.29
CM1	4D604V	10	20	(0.856)	334	1.569
ES1	Separator	10	600		E=$\pm$200 kV	
CM2	4D604V	10	20	(0.856)	354	1.658
S2	SX504	12.5	27.6		-136	1.02
Q5	NQ510	12.5	56		-470	3.981
Q6	NQ610	15	57.2		-535	-4.316
MOM	Movable horizontal slit for momentum acceptance control					
MS1	Movable vertical slit for K/π separation					
	$(y|\phi)=0$, $(y|y)=0.844$, $(y|\theta\phi)=(y|\phi\delta)=0$					
D3	6D330S	15	165.1	20	205	-6.897
S3	SX404	10	20		-34	-1.062
Q7	Q306	7.5	30.34		-464	4.026
D4	8D440S	20	198.9	60	-1943	-17.945
Q8	NQ408	10	46.5		-110	0.671
D5	8D240S	20	195.9	55	-1641	-16.205

2.3   Detectors for kaon beam

Figure 2.3 depicts the beam analyzer section, which is composed of various components such as beam line magnets, trigger counters, beam trackers, and a counter specifically for kaon identification. The beam trigger mechanism is based on a coincident signal originating from three detectors: a beam hodoscope detector (BHD), a time zero counter (T0), and an additional timing counter (T1) with the distance between BHD and T0 being approximately 7.7 meters. To control the trigger rate, a beam definition counter (DEF) is positioned just before the target. The identification of the kaon beam, which has a momentum near 1.0 GeV/c, is achieved using an Aerogel Čerenkov counter (AC) that has a refractive index of 1.05. The tracking of the kaon beam is conducted using two beam line chambers, BLC1 and BLC2. The momentum of kaon is then analyzed by combining the tracking data with the beam optics information of the D5 beam line magnet. Additionally, the trajectory of the beam just before it reaches the experimental target is precisely measured using a beam profile chamber (BPC). This measurement is crucial for accurately determining the reaction point in the target.
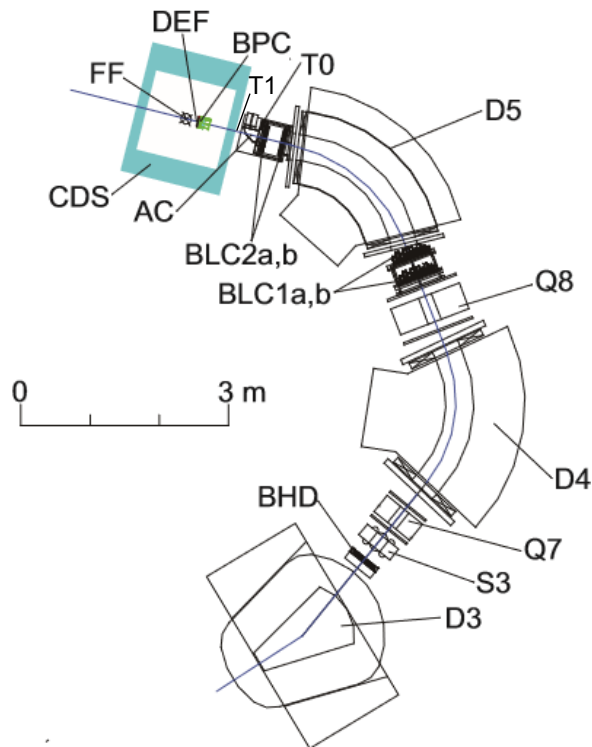
Figure 2.3: Schematic view of the beam line spectrometer setup, featuring a range of components including trigger counters (BHD, T0, T1, and DEF), beam line chambers (BLC1, BLC2, and BPC), and a counter specifically for identifying kaons (AC)[49].

2.3.1 Trigger counters

BHD, T0 and T1

The beam trigger is defined by three plastic scintillation counters: BHD, T0, and T1, which are placed after the D3 magnet, after the D5 magnet and before the Central Drift Chamber System (CDS), respectively. The timing signal from the T0 counter is used to set the zero-time reference for events.

BHD is designed with a 320 mm (horizontal) by 160 mm (vertical) effective area, divided horizontally into 16 segments. Each segment of the BHD scintillator, made from Saint-Gobain BC412 material, measures 160 mm in height, 20 mm in width and 5 mm in thickness. The scintillation light from BHD is directed to a pair of 3/4-inch Hamamatsu H6612B photomultipliers at both the top and bottom ends via acrylic light guides. Given the high event rate of approximately 1 million counts per spill from the photomultipliers, their high-voltage dividers are modified to provide increased current to the final three dynodes. The combined signals from the top and bottom photomultipliers of BHD are used for timing each segment and triggering data acquisition.

T0 features a 160 mm (horizontal) by 160 mm (vertical) area, divided horizontally into 5 segments. T0 is rotated by 45 degrees vertically relative to the beam axis. Each segment of T0, crafted from Saint-Gobain BC420 scintillator, is 160 mm high, 32 mm wide, and 10 mm thick. The method for reading out scintillation light is the same as in BHD. Intrinsic timing resolution of T0, as determined by cosmic-ray measurements, is approximately 60 ps.

T1 is a single-segment plastic scintillation counter made from Eljen EJ-230. It has dimension of 100 mm in height, 180 mm in width and 10 mm in thickness are tailored to match the effective area of AC. The scintillation light from T1 is detected by a 2-inch PMT Hamamatsu H6410B on both sides of the scintillator. A placement of T1 ensures the minimization of particle identification errors due to particles passing outside effective area of AC.

Beam definition counter (DEF)

The DEF counter is positioned right before the target vacuum vessel in the beam line. In the current setup of the beam line spectrometer, the spot size of kaon beam means that only about half of it strikes the liquid helium target. The role of DEF is to selectively target the central part of the beam at the trigger level, integrating its signal with the main beam trigger. This setup is intended to exclude particles that do not actually impact the target, thereby potentially reducing the overall trigger rate. DEF is comprised of five segments, each made from Eljen EJ-230 plastic scintillator, with dimensions of 110 mm in height, 20 mm in width, and 3 mm in thickness. At both the top and bottom ends of each scintillator segment, three 3-mm-square MPPCs (Multi-Pixel Photon Counters), specifically the Hamamatsu 13360-3050CS model, are directly attached in series. The signals from MPPCs are amplified using a discrete circuit, based on the 2-stage HP MSA-0385 amplifier.

2.3.2   Kaon identification counter

The AC (Aerogel Čerenkov counter) is placed between the T0 and T1 counters for the purpose of kaon identification at the trigger level. Figure 2.4 illustrates the threshold refractive indices for Čerenkov radiation as a function of momentum for different particle species like pions, kaons, and others. An aerogel radiator with a refractive index of 1.05 is utilized as a threshold Čerenkov counter. This setup is particularly effective in rejecting pions that have momenta around 1.0 GeV/c. As indicated in Fig. 2.5, AC has a sizeable effective area, measuring 180 mm in width and 100 mm in height with a thickness of 100 mm, ensuring coverage of the entire kaon beam distribution. Čerenkov photons produced in the direction of the beam are scattered within the aerogel, then reflected by surrounding thin mirror foil, and eventually detected by four photomultipliers positioned at both the top and bottom of the counter. For this purpose, three-inch fine-mesh type Hamamatsu R5543 photomultipliers are used, which are suitable for use in the fringe fields of the D5 and CDS magnets. AC is set to identify pions online with a detection threshold of about 7 photoelectrons. This system has been fine-tuned to achieve a pion detection efficiency exceeding 99 %, while the probability of incorrectly identifying a kaon as a pion keeps at approximately 1 %.
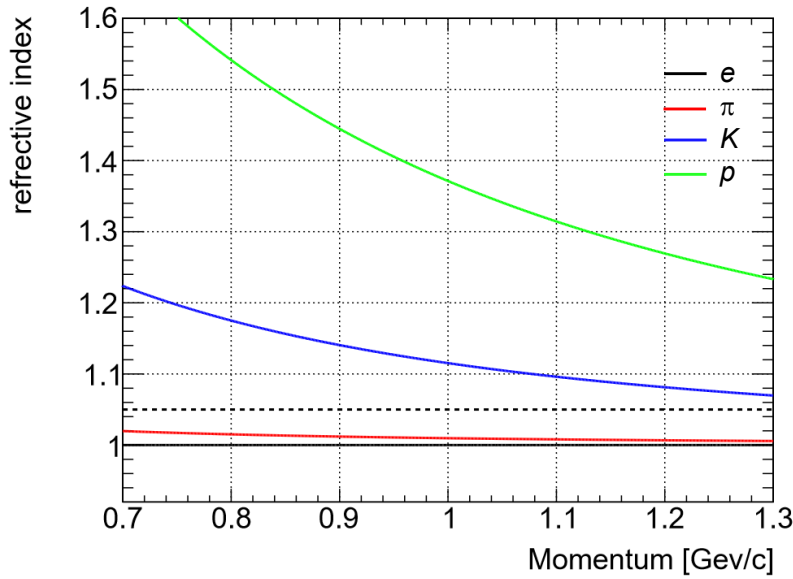
Figure 2.4: Minimum refractive index for producing Čerekov radiation as a function of the momentum of charged particles. The plot includes a dashed horizontal line representing the refractive index of the aerogel, which is n=1.05.
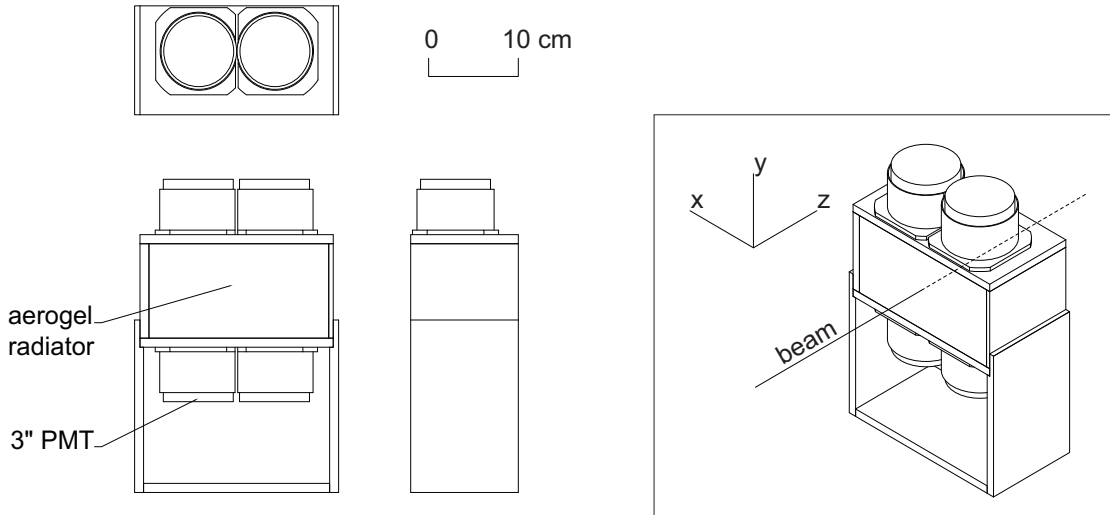
Figure 2.5: Schematic drawing of the aerogel Čerenkov counter, AC.

2.3.3 Beam momentum analyzer

At both the entrance and the exit of the D5 magnet, two planar multi-wire drift chambers, BLC1 and BLC2, are positioned. The momentum of beam particles is determined using the tracking data from these chambers combined with a second-order transfer matrix for calculation. With an position resolution of 200 μm for both BLC1 and BLC2, the momentum resolution of the beam spectrometer $\Delta p/p$ is 1×10^{-3}. The magnetic field strength of the D5 magnet is continuously monitored throughout the experiment using a high-precision Hall probe, which is read out with a Lakeshore 475 device capable of detecting changes in the magnetic field with a resolution of about 10^{-5} T. The observed fluctuation in the magnetic field was approximately 2×10^{-4}, which translates to a 0.2 MeV/c change for a 1 GeV/c beam. Additionally, a helium bag has been installed inside the D5 magnet to reduce the effects of multiple scattering caused by air.

BLC1 and BLC2

BLC1 is composed of two separate but identical drift chambers, BLC1a and BLC1b, which are spaced 300 mm apart along the direction of the beam. Each chamber is arranged in an UU'VV'UU'VV' configuration with the layers tilted at angles of ±45 degrees. Each layer contains 32 sense wires, allowing for a 4 mm drift length and covering an effective area of 256 mm × 256 mm. Both BLC1a and BLC1b have a total of 256 readout channels. Similarly, BLC2 is structured like BLC1 and includes two identical drift chambers, BLC2a and BLC2b. These chambers have a shorter drift length of 2.5 mm, translating to an effective area of 160 mm × 160 mm. BLC2a and BLC2b are positioned 275 mm apart in the beam direction. Both BLC1 and BLC2 utilize gold-plated tungsten wires with 3 % rhenium, each 12.5 μm in diameter, for the sense wires, and copper-beryllium wires, each 75 μm in diameter, for the potential wires. The cathode planes are constructed from 12.5 μm aluminized Kapton. The chambers are filled with a gas mixture of argon and isobutane, enriched with 4 % methylal (dimethoxy-methane), which

is circulated through a bubbler at a refrigerated temperature of 4 °C, in a ratio of 76 % argon, 20 % isobutane, and 4 % methylal. The operational voltage for both BLC1 and BLC2 is set at -1.25 kV, applied to both the potential wires and the cathode planes. The chambers' signals are processed through an ASD (amplifier-shaper-discriminator) board equipped with SONY-CXA3653Q chips, featuring a 16 ns shaping time, and attached directly to the chambers. These output signals are then transmitted to an LVDS-ECL converter board via 7-meter long twisted pair cables. Finally, from this converter, the signals are relayed to a FPGA-based multi-hit time-to-digital converter in the Hadron Universal Logic module (HUL).

2.3.4   Beam Profile Chamber

The Beam Profile Chamber (BPC), a type of planar multi-wire drift chamber with a circular shape, is installed just before the target cell to precisely identify the reaction vertex point. As illustrated in Fig.2.6, the outer dimensions of BPC include a diameter of 290 mm and a length of 92.2 mm along the beam axis. It comprises eight layers arranged in an XX'YY'XX'YY' pattern, each layer containing 32 sense wires. These wires facilitate a 3 mm drift length, covering an effective area with a diameter of 197 mm. BPC has in total 256 readout channels. BPC employs the same sense and potential wires, readout electronics, and gas mixture as used in the beam line chambers. However, its cathode planes are made from 9 μm carbon aramid foil. The operating voltage for BPC is set at -1.475 kV. Figure 2.7 provides a view of the cell geometries of the beam line drift chambers. The specifications and parameters of these beam line chambers are detailed in Table 2.5.
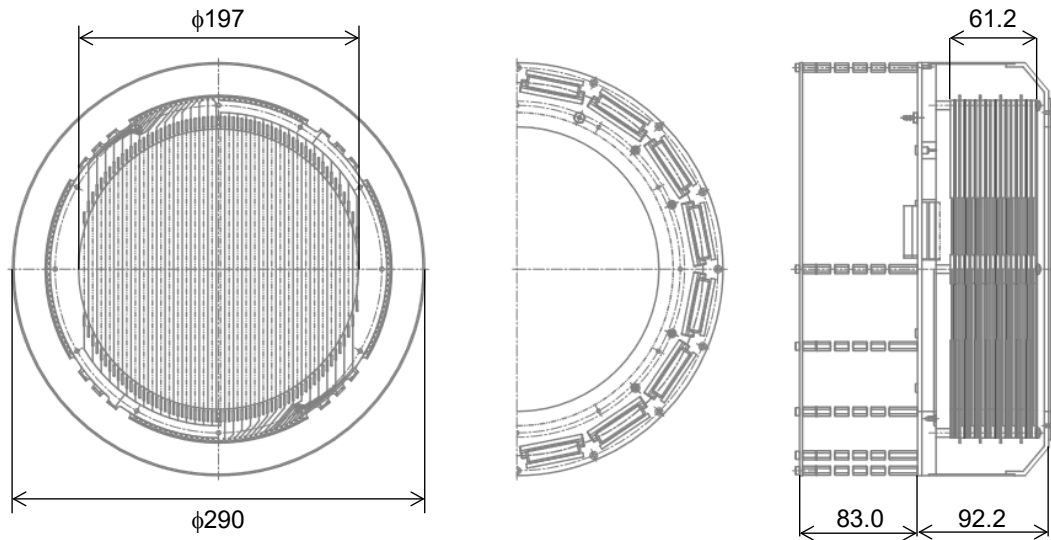
Figure 2.6: Design of BPC (all dimensions in mm).

(a) BLC1/2
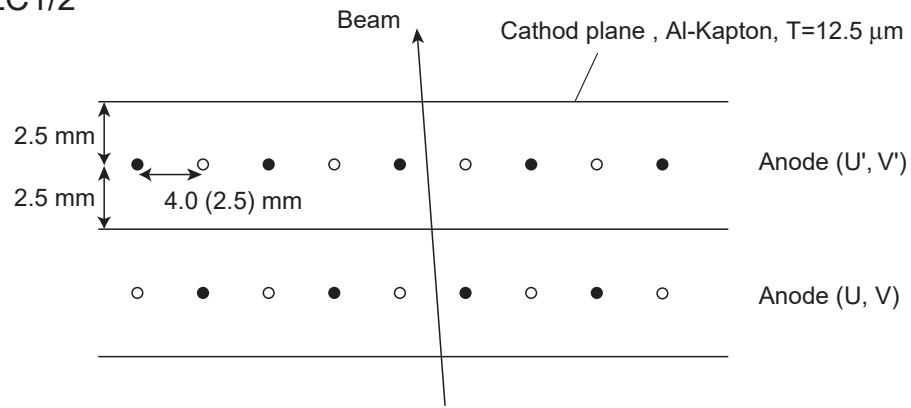
- Sense wire, φ=12.5 μm, W w/ 3% Re (Au plated)
- Potential wire, φ=75 μm, Cu-Be (Au plated)

(b) BPC
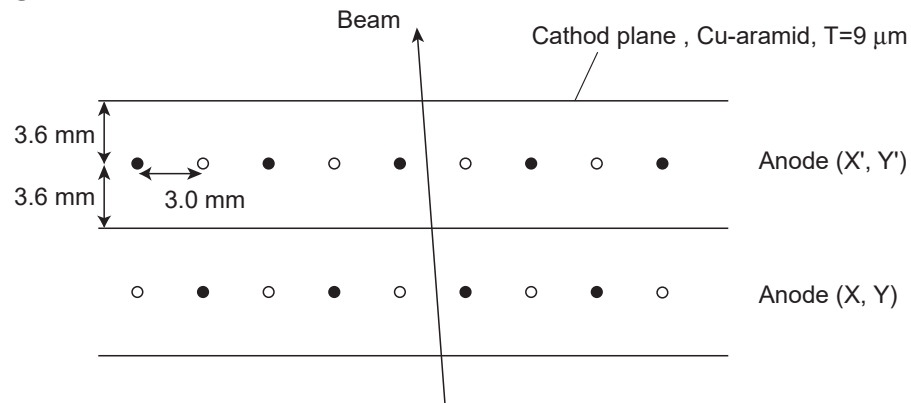
- Sense wire, φ=12.5 μm, W w/ 3% Re (Au plated)
- Potential wire, φ=50 μm, Cu-Be (Au plated)

Figure 2.7: Cell geometries of (a)BLC1/2 and (b)BPC.

Table 2.5: Summary of the beam line chamber parameters.

	BLC1a	BLC1b	BLC2a	BLC2b	BPC
number of planes	8	8	8	8	8
plane configuration	UU'VV'UU'VV'	UU'VV'UU'VV'	UU'VV'UU'VV'	VV'UU'VV'UU'	XX'YY'XX'YY'
number of sense wires in a plane	32	32	32	32	32
wire spacing (mm)	4	4	2.5	2.5	3
effective area (mm)	256 × 256	256 × 256	160 × 160	160 × 160	197 mmϕ
Sense wire material	Au-plated W (3% Re)				
diameter (μm)	12.5				
Potential wire material	Au-plated Cu-Be				Au-plated Cu-Be
diameter (μm)	75				50
Cathode plane material	aluminized-Kapton				Cu aramid
thickness (μm)	12.5				9
Gas	Ar : isoC$_4$H$_{10}$: Metylal = 38 : 10 : 2				
flow (cc/min)	50				
operation voltage potential	-1.25	-1.25	-1.25	-1.25	-1.475
cathord	-1.25	-1.25	-1.25	-1.25	-1.475

2.4 Liquid helium target system

To enhance luminosity in the experiment, a liquid target system, specifically designed for cryogenic use, was implemented. Instead of using a GM-type cryocooler, a pulse tube cryocooler (Cryomech PT410 with a remote motor) was selected. This choice allows for continuous operation of the liquid helium target without the need for periodic cryogen refills, as was necessary in previous systems [51], while still providing sufficient cooling power to liquify both helium-3 (with a normal boiling point of 3.19 K) and helium-4 (4.21 K). A diagram of the liquid helium target system is presented in Fig. 2.8. The horizontal section of the system is engineered to house a forward calorimeter system at the exit of the Central Drift Chamber System (CDS), ensuring adequate coverage of the calorimeter solid angle. The target cell, primarily constructed from beryllium, is identical to the one used in the J-PARC E15 experiment. To minimize the material budget between the target and CDC, the horizontal tube of the vacuum chamber is made from carbon fiber-reinforced plastic (CFRP).
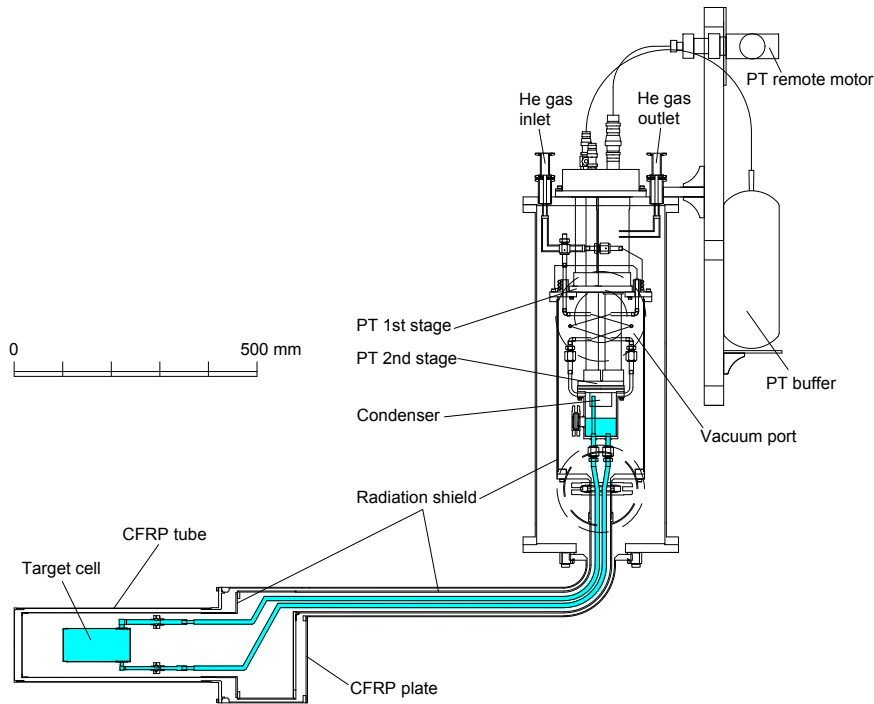
Figure 2.8: Schecmatic drawing of the liquid helium target system.

Figures 2.9 and 2.10 display the temperature variations observed at the target cell during the use of helium-4 and helium-3 targets in the experiments, respectively. The correlation between the temperature of the liquid helium and its density is depicted in Fig. 2.11. During the period when helium-4 was used, the temperature stayed within a range of 2.83 K to 2.87 K, corresponding to a density of 0.1426 ± 0.0002 g/cm^3. In the phase of the experiment involving helium-3, the temperature varied between 2.62 K and 2.71 K, leading to a density of 0.071 ± 0.001 g/cm^3.

These minor variations in density are considered to have an insignificant impact on the calculation of reaction cross-sections.
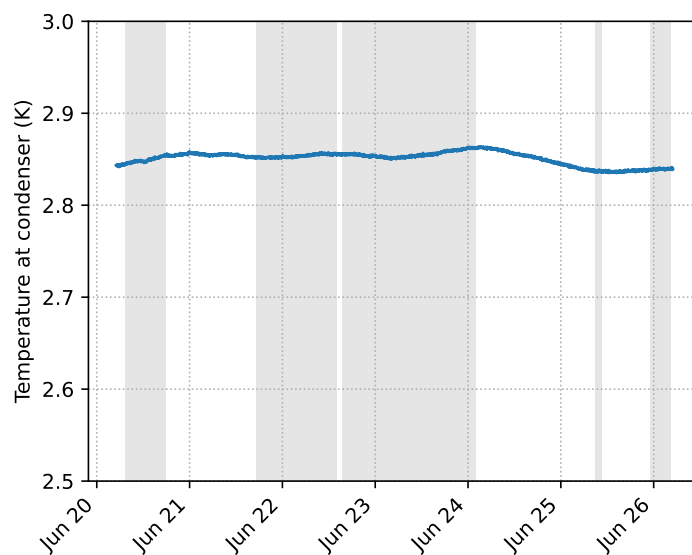
Figure 2.9: Target temperature trend of the helium-4 target operation in June 2020. The hatches show the data-taking periods.
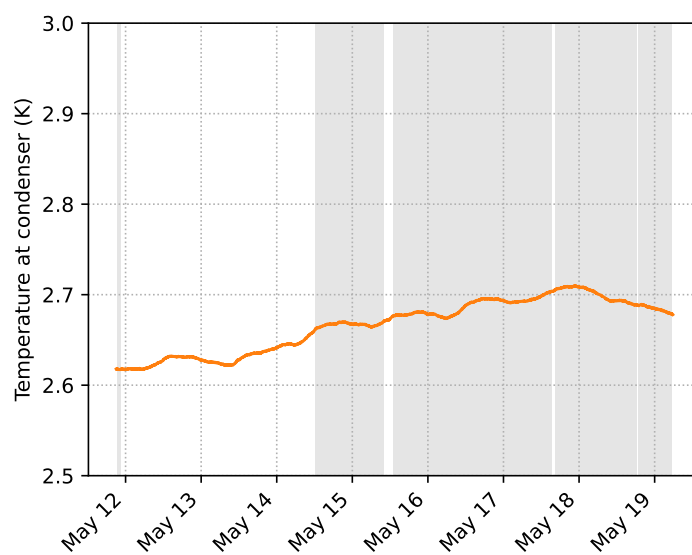
Figure 2.10: Target temperature trend of the helium-3 target operation in May 2021. The hatches show the data-taking periods.
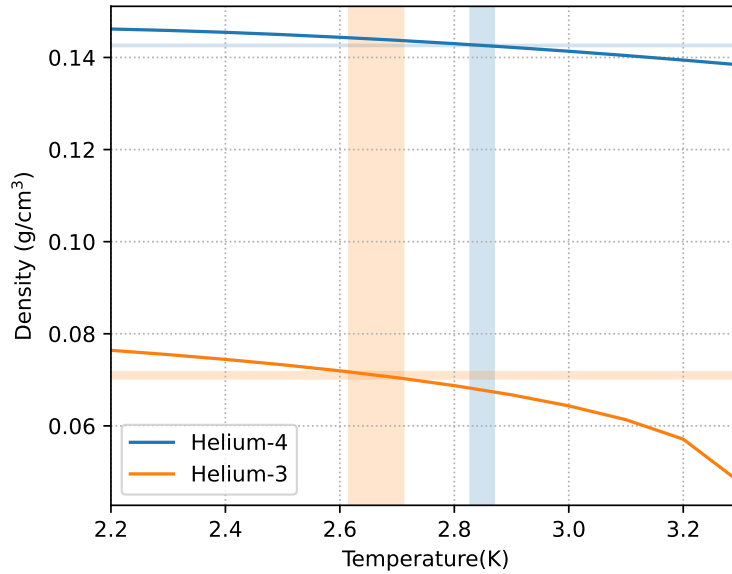
Figure 2.11: Density of liquid helium as a function of temperature. The hatches show temperature fluctuations during data-taking and corresponding density ranges.

2.5 Cylindrical detector system

The layout of the Cylindrical Detector System (CDS) is illustrated in Fig.2.12. Charged particles resulting from reactions at the target are tracked using a cylindrical drift chamber (CDC), which operates within a magnetic field of 0.715 T generated by a solenoidal magnet. A cylindrical detector hodoscope (CDH) is utilized for measuring the time-of-flight of particles, assisting in their identification and triggering the detection of charged particles. DEF and BPC, as discussed in Sec. 2.3, are positioned just before the target chamber. Details about the forward calorimeter system located at the CDS exit will be provided in Sec. 2.6.

2.5.1 Solenoidal magnet

The CDS spectrometer magnet, positioned at the final focus point of the K1.8BR beam line, is of the solenoidal type. It has a bore diameter of 1.18 meters, a length of 1.17 meters, and weighs a total of 23 tons. The design of the magnet is depicted in Fig 2.13. The magnet is engineered to provide a nearly uniform magnetic field across the tracking volume ($|z| < 420$ mm). For the current experiment, the solenoidal magnet operated at a magnetic strength of 0.715 T. The absolute value of the magnetic field was calibrated using the reconstructed invariant mass peak positions of K^0 and Λ.
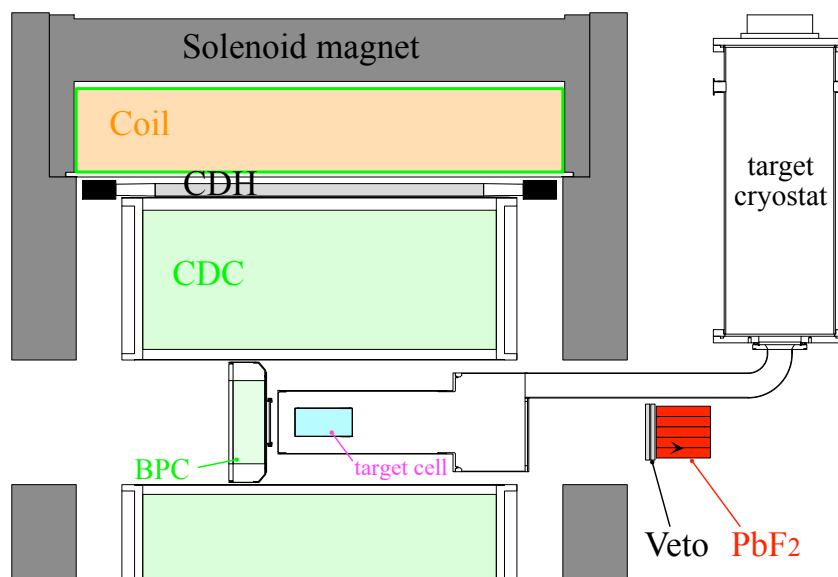
Figure 2.12: A schematic view of the Cylindrical Detector System (CDS) including the liquid helium target system[52].
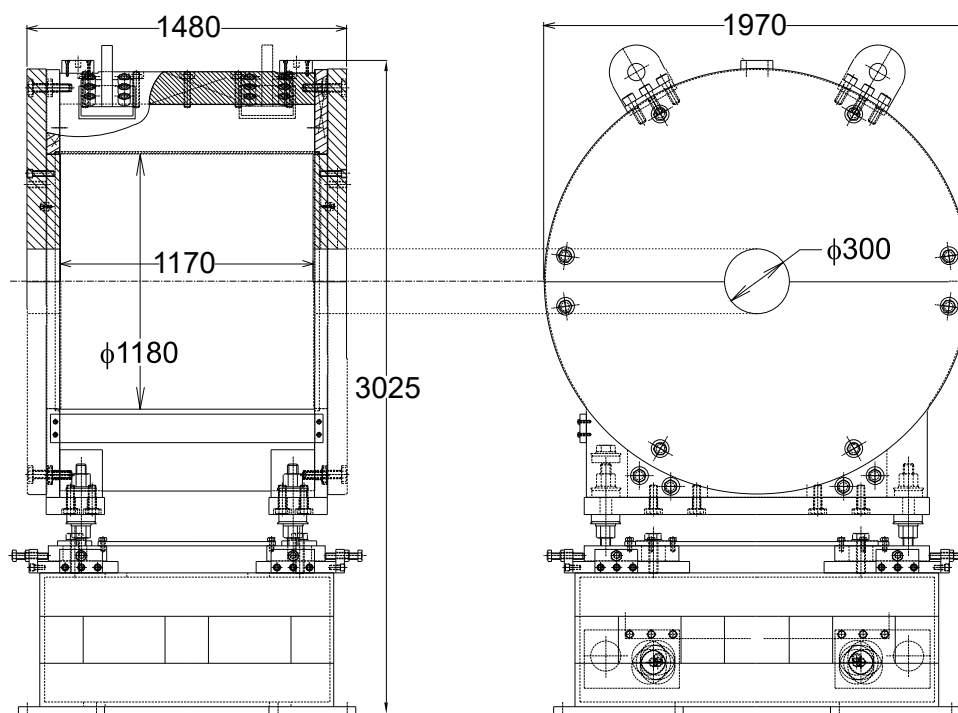
Figure 2.13: Design of the solenoidal magnet (all dimensions in mm)[49].

2.5.2 Cylindrical drift chamber

CDC, a cylindrical multi-wire drift chamber, incorporates 15 layers of sense wires. Its structure is detailed in Fig 2.14. The chamber has an outer radius of 530 mm, an inner radius of 150 mm, and a total length of 950 mm. The axial layers have a wire length of 833.8 mm, allowing for polar angle coverage from the target center of $49° < \theta < 131°$, which equates to approximately 66 % coverage of the full 4π solid angle. CDC is composed of two 20 mm thick aluminum end plates, a 1 mm thick CFRP cylinder forming its inner wall, and six aluminum beams located outside the tracking volume. The sense wires are made of 30 μm diameter gold-plated tungsten, while the field and guard wires use 100 μm diameter gold-plated aluminum. The 15 layers form hexagonal cells of CDC, typically with a 9 mm drift length, and are arranged into 7 super-layers as depicted in Fig. 2.15. Table 2.6 lists the specific wire configurations. The layers extend radially from 190.5 mm (layer #1) to 484.5 mm (layer #15). Eight stereo layers, tilted by about 3.5 degrees, provide information of the longitudinal position. CDC features 1816 readout channels and a total of 8064 wires. The chamber is filled with a pre-mixed gas of argon (50 %) and ethane (50 %) at 1 atm.

The first (A1) super-layer has a high voltage of -2.75 kV applied to the potential wire. The second (U1) and third (V1) super-layers have a high voltage of -2.85 kV applied to the potential wires, while the potential wires of the other super-layers receive -2.80 kV. The guard wires have -1.535 kV applied to the innermost, -1.830 kV to the outermost, and -0.646 kV to other guard wires. The sense wires are at ground potential. The readout electronics of CDC are similar to those in the beam line chambers, comprising a preamplifier board with ASDs (SONY-CXA3653Q, τ = 16 ns), an LVDS-ECL converter, and a TDC.
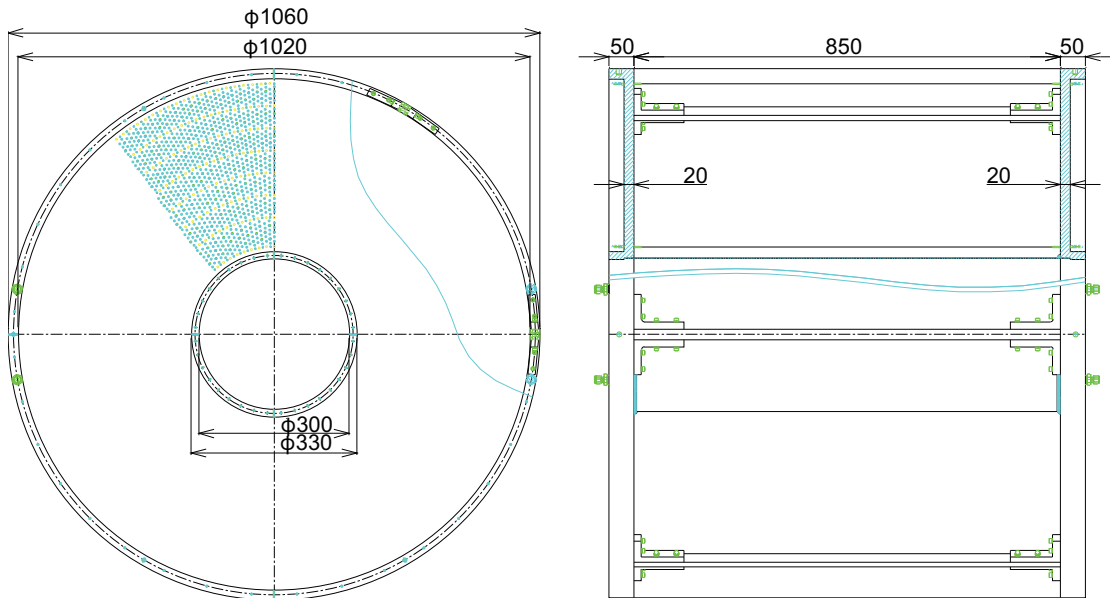
Figure 2.14: Design of CDC (all dimensions in mm). CDC consists of two aluminum end-plates, a 1 mm thick CFRP cylinder as an inner wall and six aluminum beams those are placed outside the tracking volume[49]
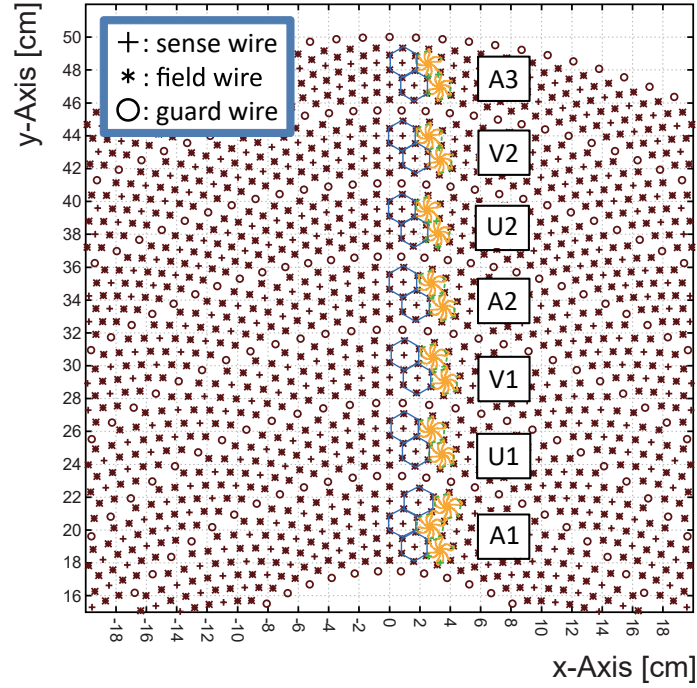
Figure 2.15: Cell structure of CDC[49].

Table 2.6: Wire configuration of CDC.

Super-layer	layer	Wire direction	Radius (mm)	Cell width (degree)	(mm)	Stereo angle (degree)	Signal channels
A1	1	X	190.5		16.7	0	72
	2	X'	204	5.00	17.8	0	72
	3	X	217.5		19	0	72
U1	4	U	248.5	4.00	17.3	-3.55	90
	5	U'	262		18.3	-3.74	90
V1	6	V	293	3.60	18.4	3.77	100
	7	V'	306.5		19.3	3.94	100
A2	8	X	337.5	3.00	17.7	0	120
	9	X'	351		18.4	0	120
U2	10	U	382	2.40	16	-3.28	150
	11	U'	395.5		16.6	-3.39	150
V2	12	V	426.5	2.25	16.7	3.43	160
	13	V'	440		17.3	3.54	160
A3	14	X	471	2.00	16.4	0	180
	15	X'	484.5		16.9	0	180

2.5.3 Cylindrical detector hodoscope

CDH, a cylindrical plastic scintillation counter, is divided into sections along its azimuthal direction and serves the dual purposes of triggering charged particle detection and aiding in particle identification. Positioned at an inner radius of 544 mm from the beam axis, it encompasses a polar angle range from 54 to 126 degrees, which translates to about 59 % coverage of the total 4π solid angle. This detector comprises 36 individual modules, each mounted on the inner wall of the solenoidal magnet. The modules are made of Eljen EJ-200 plastic scintillators, each with a size of 790 mm in length (along the beam axis), 99 mm in width and 30 mm in thickness (in the radial direction). The generated scintillation light is channeled through light guides to Hamamatsu R7761 photomultipliers. These are 1.5-inch fine-mesh type PMTs with 19-stage dynodes, designed to withstand the solenoidal magnetic field. The average time resolution of CDH, as determined without a magnetic field using cosmic ray data, is 71 ± 3 ps (r.m.s.), with the error indicating the variation across different segments.

2.6 Forward calorimeter system

For the current experiment, an electromagnetic calorimeter was installed at a forward angle to detect high-energy gamma-rays associated with hypernucleus production. The calorimeter is installed on the exit of CDS, which is along the path of meson beam. A 1 MHz level charged-hadron beam directly hits the calorimeter. PbF_2 was chosen as the calorimeter material to match the operational conditions. Upstream of the calorimeter, plastic scintillation counters were installed to remove charged particles. Downstream, BTC was installed to identify full-energy deposition events.

2.6.1 PbF$_2$ Calorimeter

The critical requirements for the electromagnetic calorimeter in the present experiment are a fast response and a high radiation hardness because the calorimeter is installed along the path of beam particle. PbF_2 crystal is almost a unique choice to meet these requirements. Their response is fast because they are Čerenkov-radiation based calorimeters. A typical pulse width is a few tens of ns, much faster than scintillation based calorimeters. Another advantage of the PbF_2 crystal is their radiation hardness, being one order of magnitude better compared with a typical lead glass crystal [53]. Little degradation is expected even after one-month beam exposure at J-PARC. In addition, PbF_2 crystal has considerably short radiation length and high density. The calorimeter system can be compact, which helps to integrate it with CDS and the liquid helium system. Also, for the present experiment, PbF_2 is expected to have a sufficient energy resolution about 5% at 1 GeV/c. Table 2.7 summarizes properties of the PbF_2 crystal.

The size of a PbF_2 crystal used in the J-PARC E73 experiment is 2.5×2.5 cm^2 in cross-section and 14 cm in length along the beam axis. The cross-section is determined considering the Moliere radius. The crystal length corresponds to 15 radiation lengths, enough to fully stop electrons and gamma-rays. A PMT Hamamatsu H6612B is attached to the downstream end of

Table 2.7: Properties of PbF_2 crystal [54].

Crystal	Radiation length	Moliere radius	Density	Refractive index
PbF_2	0.93 cm	2.22 cm	7.77 g/cm^3	1.82

a PbF_2 crystal using optical cement or UV-cured resin for helium-4 data in June, 2020. The coupling was changed to silicon cookies for helium-3 data in May, 2021. Aluminized Mylar sheet covers the PbF_2 crystal.

The calorimeter consists of 40 segments of the PbF_2 crystals stacked in five rows in the vertical direction and eight columns in the horizontal direction. The total size is 200 cm (horizontal) $\times$ 125 cm (vertical), corresponding to the angular coverage up to about 10 degrees at 85 cm downstream of FF. The whole assembly is installed in a 1-cm thick iron box to shield the fringing field of CDS. The measured fringing field in the shield box was 15.5 Gauss. Figure 2.16 display a photo of the 1-unit module (left) and a photo of the overall PbF_2 calorimeter (right).
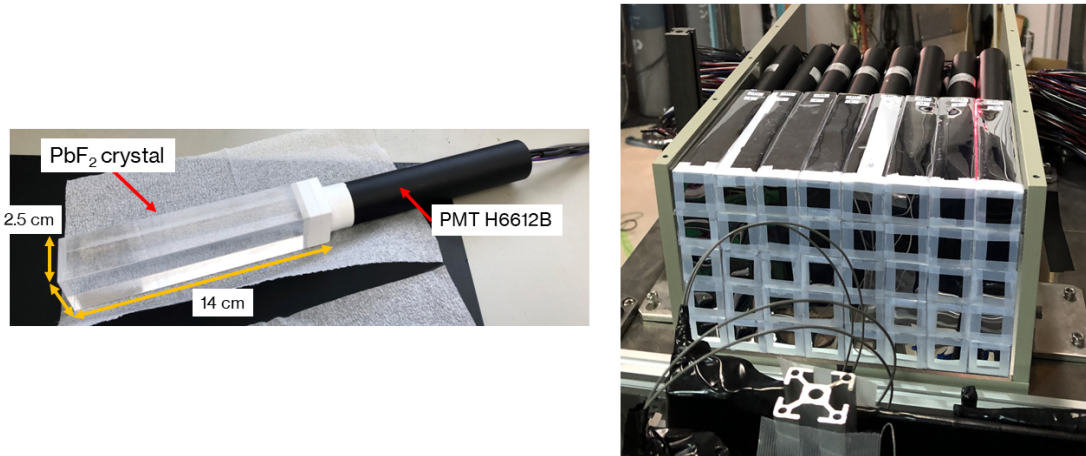
Figure 2.16: Photos of the PbF_2 calorimeter. (left) 1-unit module. (right) the overall PbF_2 calorimeter.

Performance evaluation with a positron beam

The performance of the PbF_2 calorimeter was evaluated using a positron beam at the Research Center for Electron Photon Science (ELPH), Tohoku University[55]. ELPH has a high-energy electron booster synchrotron[56, 57, 58]. The positrons are tertiary particles generated from the second GeV bremsstrahlung photon beam[59, 60]. The positron beam energy was changed from 100 to 800 MeV with 100 MeV steps. Table 2.8 summarizes conditions of the test experiment. Two crossed scintillation finger counters defined the beam injection point at the center of a PbF_2 segment with 5 mm $\times$ 5 mm size. The total energy deposited by the beam particle was evaluated by summing up the energies of a primary segment and 8 secondary segments around it. Here, the primary segment had the largest energy deposit among the 40 segments. In this case, the primary segment is usually just behind the trigger counters. Figure 2.17 shows the energy resolutions

Table 2.8: Summary of test experimental condition

Facility	Beam line	Beam particle	Beam momentum	Reflective material	Period
ELPH	GeV-γ	e^+	0.1–0.8 GeV/c	ESR	Dec. 2019

obtained as a function of the beam energy for a typical primary segment. The energy resolution (σ/E) depended on the incident energy (E) can be well described by Eq. (2.2).

$$\frac{\sigma}{E} = \sqrt{(\frac{a_0}{\sqrt{E(\text{GeV})}})^2 + (\frac{a_1}{E(\text{GeV})})^2 + b^2,} \tag{2.2}$$

where a_0 is a statistical term, a_1 is a electrical noise term and b is a constant term. The values for parameters a_0, a_1, and b were obtained as 0.027, 0.014, and 0.038, respectively. These values are similar to those in the previous studies [61]. The achieved resolution about 5% at 1 GeV/c satisfies the requiement for J-PARC E73.
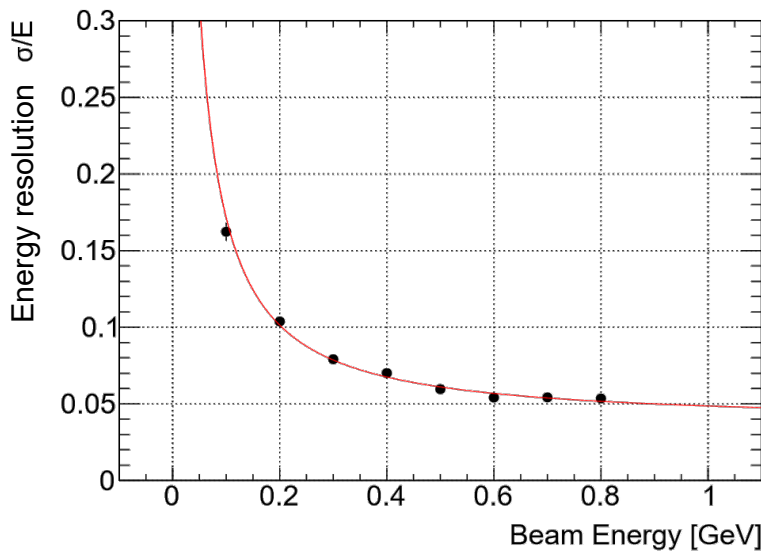
Figure 2.17: Energy resolution (σ/E) as a function of positron energy for a typical segment.

2.6.2 Charged particle veto counter

A charged particle veto counter (VETO) is installed immediately before the PbF$_2$ calorimeter to remove charged particles. VETO is constructed from two layers of plastic scintillators, aligned along the beam direction. These scintillators are crafted from Eljen EJ-200 and each has dimensions of 125 mm in height 200 mm in width, and 10 mm in thickness. The scintillation light generated in the scintillators is then directed to 3/4-inch Hamamatsu H6612B photomultipliers, which are positioned at both the right and left ends of the counter. Apart from its primary

function of vetoing charged particles, VETO is also employed for the identification of charged particles, which aids in the calibration of the PbF$_2$ calorimeter.

2.6.3   Beam Through Counter

The Beam Through Counter (BTC) is situated after the PbF$_2$ calorimeter and is designed to identify beam particles that pass through the PbF$_2$ crystal. This counter, used in conjunction with AC, enables the selection of charged pions that have traversed the PbF$_2$ calorimeter. This selection is crucial for providing a reference for relative gain calibrations among the PbF$_2$ crystals. Additionally, BTC plays an important role in pinpointing full-stop events within the PbF$_2$ calorimeter. By using the upstream VETO to detect charged particles and confirming that BTC did not register these particles, it becomes possible to isolate electrons in the beam. These 1 GeV/c electrons are then utilized as a point of reference for energy calibration. BTC is equipped with a plastic scintillator measuring 200 mm in height 200 mm in width, and 10 mm in thickness. The scintillation light produced by this scintillator is captured by a 2-inch Hamamatsu H6410B photomultiplier.

2.7   Materials in spectrometer system

In the spectrometer system, various materials can cause energy loss, multiple scattering, and reactions for both the beam and the particles that scatter off it. These interactions are likely to lead to systematic deviations in the measured momenta, as well as losses of events and further degradation in the resolution of the spectrometer. To address these issues, corrections are made for the momenta of charged particles, accounting for the materials they encounter along their paths. Specific routines have been developed to correct for the effects of materials on the kaon beam and the charged particles within CDS. These corrections consider the materials listed in Table 2.9 for the kaon beam and Table 2.10 for CDS. However, certain components like the wires and cathode planes of the drift chambers, the windows and reflection sheet of AC, and the wrappings of the scintillator bars are not factored into these corrections. This is because their impact is minor when compared to the desired precision level of a few MeV/c.

2.8   Data acquisition

2.8.1   Data acquisition system

The K1.8BR beamline has implemented a network-based triggered data acquisition (DAQ) system. Data from each detector is read out through each front-end subsystem, and then sent via TPC/IP network to the main DAQ computer, where the event builder combines the data from all subsystems. After event building, the data streams are sent to the recorder and online analyzers via the event distributer. The software package HDDAQ, developed for the experiments at J-PARC HEF [62], handles above processes. A trigger management system is employed for event synchronization across various subsystems, utilizing a Master Trigger Module (MTM) in

Table 2.9: A summary of the materials present in the beam line from the center of BLC2 (at $z = -130$ cm) to the Final Focus (FF) point is provided. The reductions in momentum for a 1 GeV/c kaon beam are calculated based on the Bethe-Bloch formula.

Component	Material	Density g/cm^3	Thickness mm	Thickness g/cm^2	$-\delta p$ (MeV/c) 1 GeV/c kaon
BLC2b	Ar-isoC$_4$H$_{10}$	0.0016	100	0.02	0.03
T0	Scintillator	1.03	10	1.03	2.4
AC	Aerogel	0.20	100	2.00	4
T1	Scintillator	1.03	10	1.03	2.4
BPC	Ar-isoC$_4$H$_{10}$	0.0016	60	0.01	0.02
DEF	Scintillator	1.03	3	0.31	0.72
Target system					
Chamber cap	aluminum	2.7	0.6	0.16	0.3
Radiation shield	aluminum	2.7	0.2	0.05	0.1
Cell cap	AlBeMet	2.07	0.6	0.12	0.23
Target	helium-3	0.071	50	0.36	1.68
	helium-4	0.143	50	0.72	2.51
Air	Air	0.0012	940	0.11	0.24
Total					
helium-3				5.20	9.51
helium-4				5.56	10.34

Table 2.10: Summary of materials factored into the correction for energy loss in tracks within CDC.

Component	Material	Density g/cm^3	Thickness mm	Thickness g/cm^2
Target system				
Target	helium-3	0.071	34	0.25
	helium-4	0.143	34	0.50
Cell wall	beryllium	1.85	0.3	0.06
Radiation shield	aluminum	2.70	0.2	0.05
CFRP	CFRP	1.70	1	0.17
Air	Air	0.0012	75	0.009
CDC				
CFRP	CFRP	1.70	1	0.17
Gas	Ar-C$_2$H$_6$	0.0015	380	0.057
Total				
helium-3				0.77
helium-4				1.02

conjunction with a Receiver Module (RM). This system is tasked with allocating an event tag to each subsystem, which encapsulates both the beam spill number and the event number.

In the context of front-end digitization, the recent development of Hadron Universal Logic (HUL) modules [63] has been a significant advancement. Since the HUL is an FPGA-based module, different fanctionality can be implemeted by modifying the FPGA firmware. The input/output can be also extended by up to two mezzanine cards per module. In the present experiment, HULs are used as reciver modules of the trigger tag (RM), multi-hit time-to-digital converters (MHTDC), high-resolution multi-hit TDC (HRTDC), scaler and a trigger logic module for the calorimeter. HUL-MHTDC and HUL-HRTDC digitize the timing signals from drift chamber and other counters read out with photo sensors, respectively. Pulse charge information of signals from photo sensors, namely photomultipliers and MPPCs, are recorded using CAEN V792 modules. V792s are controlled and read out via the VME bus using a single board computer module GE XVB602. In total, 34 front-end nodes are used; these include 2 VME nodes containing 6 CAEN V792 modules, 26 HUL-MHTDC nodes, 3 HUL-HRTDC nodes, 2 HUL-Scaler nodes, and 1 HUL-RM node. Additinally, a HUL-Scaler monitores spill-by-spill scaler counts of each detector and trigger, independently from the data-acquisition operation.

2.8.2 Trigger scheme

Online triggers are constructed to select events to be recorded with the data-acquisition system. The main analysis channel of the present experiment requires a K^- beam, a forward gamma ray to tag the (K^-, π^0) reaction, and a π^- in CDS to identify the two-body weak decay of hypernuclei. The main online trigger should be constructed accordingly, to maximize the data-acquisition efficiency. Furthermore, objective triggers were employed to assess cross sections and detector performance, as well as to examine other by-product processes.

Kaon beam trigger

The basic beam trigger is formed by combining coincidence signals from the beam line detectors, which include BHD, T0, T1, and DEF. The selection of the kaon beam trigger (K_{beam}) is made from this beam trigger by utilizing the kaon identification counter. Specifically, a veto signal from AC is used to define the kaon beam. The formulation of the kaon beam trigger can be described as follows:

$$K_{\mathrm{beam}} \equiv \mathrm{BHD} \otimes \mathrm{T0} \otimes \mathrm{DEF} \otimes \overline{\mathrm{AC}}.$$

A trigger for the pion beam is established through a coincident signal from AC. Then,

$$\pi_{\mathrm{beam}} \equiv \mathrm{BHD} \otimes \mathrm{T0} \otimes \mathrm{DEF} \otimes \mathrm{AC}.$$

Physics trigger

The physics trigger is given as the coincidence of a kaon beam and a forward gamma-ray,

$$\mathrm{Physicstrigger} \equiv \mathrm{K}_{\mathrm{beam}} \otimes \gamma_{\mathrm{forward}},$$

where the forward gamma-ray trigger is defined as

$$\gamma_{\text{forward}} \equiv \text{Calo} \otimes \overline{\text{VETO}}.$$

CDH was not included in the physics trigger because the number of triggers was already small enough to maintain high DAQ efficiency.

Triggers for the detector calibration

As mentioned in Sec. 2.6, pions and electrons are useful for the energy-scale calibration of the PbF$_2$ calorimeter. The trigger logics are defined as

$$\pi_{\text{calo}} \equiv \text{T0} \otimes \text{Calo} \otimes \text{Veto} \otimes \text{BTC},$$
$$e_{\text{calo}} \equiv \text{T0} \otimes \text{Calo} \otimes \text{Veto} \otimes \overline{\text{BTC}}.$$

For CDH, timing calibration is crucial to analyze the lifetime of the hypernuclei. π^- beam-induced prompt events are useful for the calibration purpose. The trigger logic is defined as

$$\pi\text{CDH} \equiv \pi_{\text{beam}} \otimes \text{CDH}.$$

Additionally, it mixed the trigger logic defined as

$$K\text{CDH} \equiv \text{K}_{\text{beam}} \otimes \text{CDH}.$$

These trigger modes are mixed up with reasonable pre-scaling factors.

DAQ efficiency

The efficiency of the DAQ system is determined by comparing the proportion of events successfully recorded to the total number of events requested. For the production of $^4_\Lambda\text{H}$, the DAQ efficiency was measured at $91.8 \pm 0.7\%$, while for $^3_\Lambda\text{H}$ production, it was slightly higher at $92.6 \pm 0.4\%$. On average, the trigger rate per spill was $1.2 - 1.4 \times 10^4$ events.

Chapter 3

Data analysis

3.1 Overview

This chapter outlines the analysis of data from each detector before the subsequent physics analysis. After the data summary, Sec. 3.2 describes the common analysis procedure for all detectors. Then, the analysis of individual detector components including calibration methods and performance evaluations are presented. Section 3.3 describes the kaon beam analysis and the evaluation of the effective luminosity. Section 3.4 describes the analysis of the CDS; reconstruction of the reaction vertex, particle identification and reconstruction of K_S^0 and Λ. Finally, Sec. 3.5 describe the calorimeter analysis focusing on the calibration method of the energy scale using π^- and e^- beams.

3.1.1 Data summary

Table 3.1 summarizes the data utilized in the present thesis. The helium-4 target data was obtained in a feasibility study of the production of hypernucleus via the (K^-, π^0) reaction, which was performed as a test experiment, J-PARC T77. The helium-3 target data was collected as the first phase of the J-PARC E73 experiment, mainly to evaluate the production cross sections of $_\Lambda^3\mathrm{H}$ prior to the full physics runs to measure the lifetime.

Table 3.1: Data summary.

target	run period	total duration	total primary beam amount	number of kaons by beam trigger
helium-4	2020/6/20–2020/6/26	65 h	138 kW·day	9.28×10^9
helium-3	2021/5/11–2021/5/19	107 h	261 kW·day	18.2×10^9

3.1.2   Definition of the coordinates

In this thesis, the z-axis is aligned with the beam axis, and the x and y-axes correspond to the horizontal and vertical directions, respectively, in a right-handed coordinate system. Downstream of the beamline is the positive direction of the z-axis and upward is the positive direction of the y-axis. When observed from the downstream end of the beam line, the positive x-axis is situated to the right of the beam axis.

3.2   Common analysis procedures for all detectors

3.2.1   TDC data conversion to time

The HUL-MHTDC and HUL-HRTDC modules were used to collect time data. They are synchronous circuits to a master clock. Therefore, the channel-to-time conversion coefficient can be determined accordingly.

3.2.2   ADC data conversion to energy

The energy calibration of the beam line detectors is carried out using a 1 GeV/c π^- beam. For the detectors on the beam line, the energy conversion from ADC channels is performed using a 1 GeV/c π^- beam, which gives approximately 2 MeV/1 cm energy deposition on a plastic scintillator. To calibrate the energy loss of CDH, the reconstructed pion track by CDC is the calibration source based on the pass-through length in CDH evaluated track by track. For the calibration of the calorimeter, the relative energy scale of each segment is aligned with a 1 GeV/c π^- beam. Then, the absolute energy scale was adjusted using electrons at 1 GeV/c.

3.2.3   Time-walk correction and time offset tune for scintillation counters

Timing signals generated by a leading-edge discriminator systematically depend on the pulse height of the detector analog signal. This phenomenon is well known as the time-walk effect. This effect is rectified during offline analysis using a correction function,

$$t_c = t + p_0 + \frac{p_1}{\sqrt{dE}}. \tag{3.1}$$

In this context, t represents the time information derived from Eq. (3.1), while dE indicates the energy detected by the photo-sensor and recorded by ADC, and p_i are the parameters used for correction. These correction parameters are determined through iterative adjustments to the relationship between dE and timing, using a π^- beam. Additionally, this process involves aligning the timing offsets across different segments by tuning the parameter p_0.

3.3   Kaon beam analysis

The beam particle is identified and momentum analyzed using beam line counters and beam line drift chambers. In the analysis of the beam particle identification, the time-of-flight (TOF)

measurement ensures that the beam particle is kaon. In the beam momentum analysis, beam line drift chambers in combination with transport optics of the beam line magnets give the momentum vector of the beam. For these analyses, it is crucial to eliminate beam pile-up events in order to clearly identify reactions induced by kaons. The procedure of the beam line analysis to select single K^- beam events is as follows:

1. Only events with a single hit in T0 are selected.

2. Confirm that the TOF between T0 and BHD matches that expected from a kaon beam.

3. Make sure that both BLC1 and BLC2 register just a single track.

4. Carry out the reconstruction of the beam momentum.

5. Verify that BPC detects only a single track.

6. Assess the agreement between the tracks recorded in BLC2 and BPC.

7. Check that the projected path of the BPC track falls within the fiducial volume of the target.

The subsequent sub-sections provide an detailed description of each step in the analysis procedure.

3.3.1 Kaon identification by TOF between BHD and T0

While the online trigger uses AC to identify the kaon beam, there remains a slight contamination of pions due to inefficiency of AC. Moreover, a significant number of events are marked by multiple hits on T0 and BHD, as shown in Fig. 3.1. The initial step involves selecting events with a single hit on T0 to mitigate beam pile-up. However, multiple hits on BHD are accepted since most pile-up particles at BHD do not reach the experimental target, and excluding them would result in the loss of a substantial portion of the data. The specific BHD hit corresponding to the T0 hit is determined by ensuring that the TOF between BHD and T0 aligns with that of a K^- at 1 GeV/c. To calibrate the relative time offsets and the time-walk effects of BHD segments in relation to the T0 segment #3, pions with a constant flight length of 7.7 m and a beam momentum of 1 GeV/c are used. Deviations of flight length from the central trajectory are not taken into account. A typical TOF spectrum for kaon beam trigger data is shown in Fig 3.2. The TOF resolution is estimated to be about 200 ps (r.m.s.) by analyzing the peak corresponding to kaons. The selection criteria for kaon beam selection are set to $\pm 3\sigma$ around the center of the kaon peak.

3.3.2 beam line drift chamber analysis

Conversion time information into hit position

In the beginning, it is essential to establish a correlation between the drift time and the corresponding drift distance. This process involves the assumption that the beam particles traverse
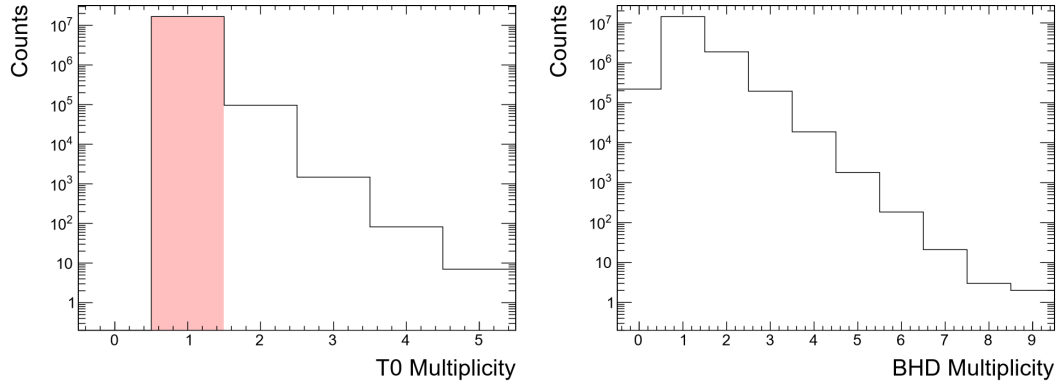
Figure 3.1: Hit multiplicity of T0 (left) and BHD (right) for the kaon beam trigger data. T0 single-hit is required in the right figure.
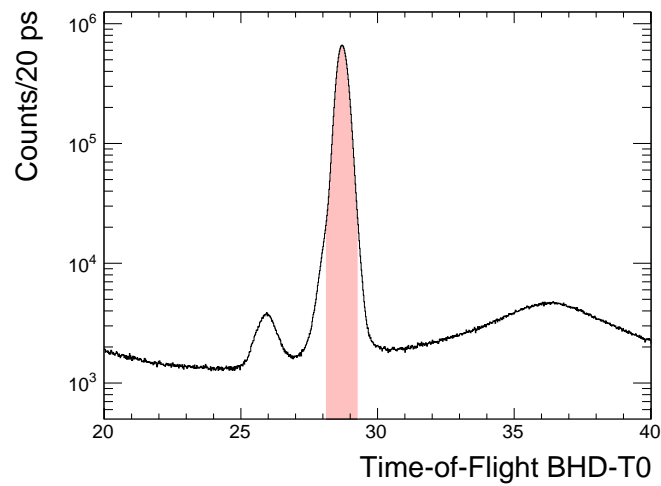
Figure 3.2: For the kaon beam trigger data, the TOF distribution between BHD and T0 is analyzed, permitting the multiple hits on BHD. The peaks at approximately 26 ns and 29 ns are indicative of π^- and K^-, respectively. Beam particles that fall within the TOF range highlighted in red are identified as kaons. This selected range encompasses $\pm 3\sigma$ of the kaon TOF peak.

the drift chambers perpendicular to the wire planes and are almost uniformly distributed across each chamber cell. Subsequently, a conversion formula connecting drift time to drift distance is derived through the integration of the drift time distribution, as depicted in Fig. 3.3 (top and middle). The conversion formula is determined individually for each wire using K^- beams. Additionally, the relative timing offset for each wire is fine-tuned by analyzing the peak position in the differentiated drift time spectrum, which is illustrated in Fig. 3.3 (bottom).

Linear tracking

The position of a hit in each plane is determined using the wire position and the drift length. However, the direction of drift remains uncertain. To resolve this, for a given set of hits, every possible combination of drift directions is considered. The combination that results in the lowest value of χ^2/ndf is chosen. In three-dimensional linear fitting, χ^2/ndf is defined as follows:

$$\chi^2/ndf \quad = \quad \frac{1}{N-4} \sum_i^N \left(\frac{x_i' - f(z_i)}{\sigma_i} \right)^2, \tag{3.2}$$

$$f(z) \quad = \quad \cos\theta(a + zb) + \sin\theta(c + zd), \tag{3.3}$$

where N represents the total number of identified hits, while x' denotes the positions perpendicular to both the wire and the beam direction. The function $f(z)$ calculates the position at z within a plane that is rotated by an angle θ, and σ symbolizes the assumed precision of the position. The four parameters a, b, c, d in Eq. (3.3) are analytically determined at the point where χ^2/ndf reaches its minimum, based on the provided set of hits.

Timing analysis

Due to the configuration of TDCs with gate windows around 1700 ns, numerous multi-beam-particle events occur, leading to multiple detections in the beam line drift chambers. To unambiguously determine the relevant hits and discard irrelevant hits not associated with the trigger particle, a method of timing analysis is employed. Relying on timing selection from a single plane is ineffective because of the broad distribution of drift times, typically about 150 ns. A more effective approach is the paired-plane analysis, such as the XX' technique, which can accurately determine the time of particle transit with satisfactory resolution. The beam line chambers are composed of staggered plane pairs, each offset by half the size of a cell. For a correct hit selection, the total drift lengths of the paired hits should be close to the size of one cell. Figure 3.4 (top) illustrates the relationship between the differences and the averages of drift times in the paired planes for single-track events. The correlation seen in Fig. 3.4 (top) results from the non-linear relationship between drift time and drift length, especially due to the slower drift velocity near the cell edges (as shown in Fig. 3.3 (middle)). Correcting this correlation, as shown in Fig. 3.4 (bottom), the revised average drift time accurately reflects the particle passage time at the specific paired plane. The adjustment is made separately for each paired plane. If the search for paired hits is unsuccessful, those particular planes are then excluded from the timing analysis.
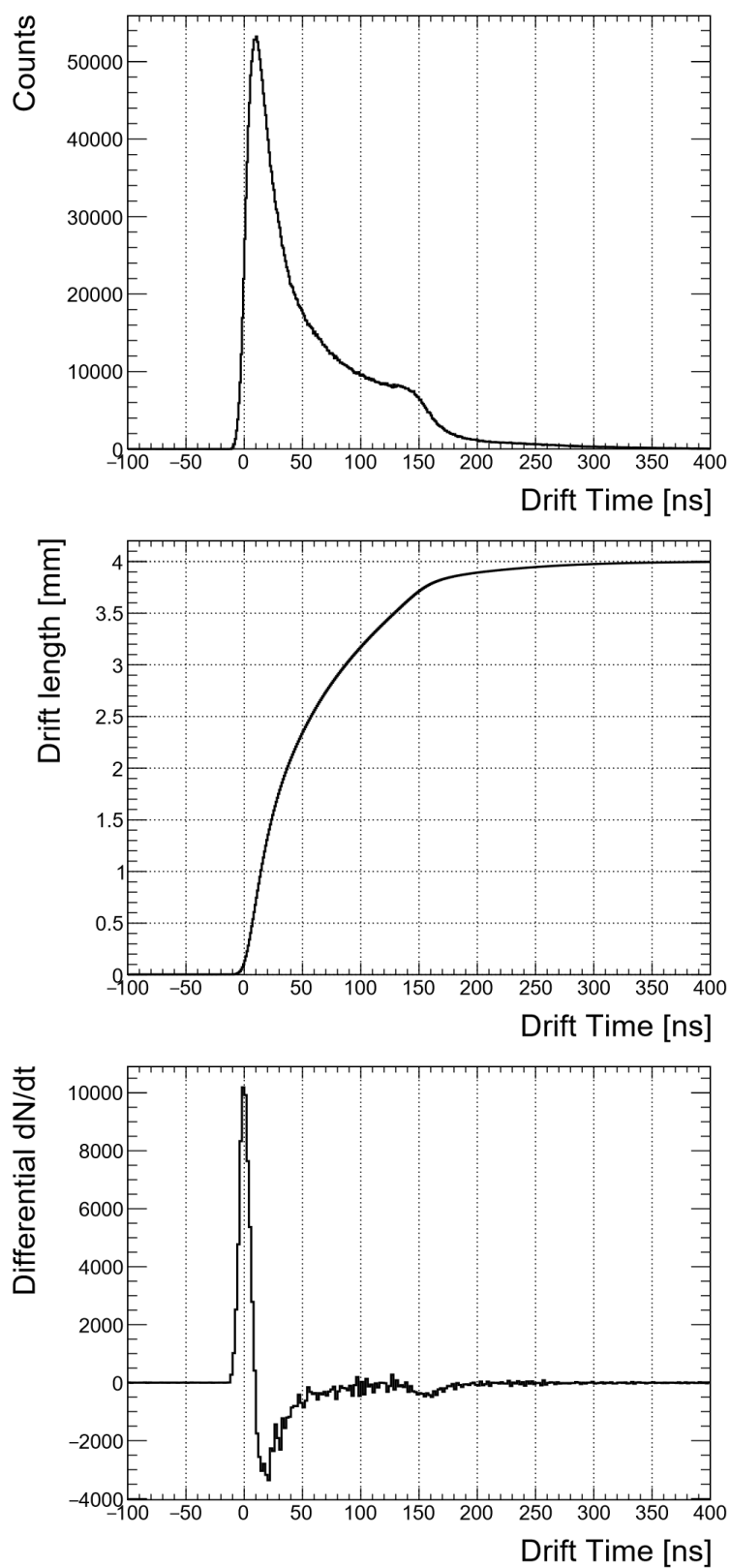
Figure 3.3: (top) Drift time distribution of a typical wire in BLC1. (middle) Integrated drift time spectrum. The maximum velue was normalized by the cell size. (bottom) Differential of the drift time distribution. The peak position was used to adjust the relative timing offset.
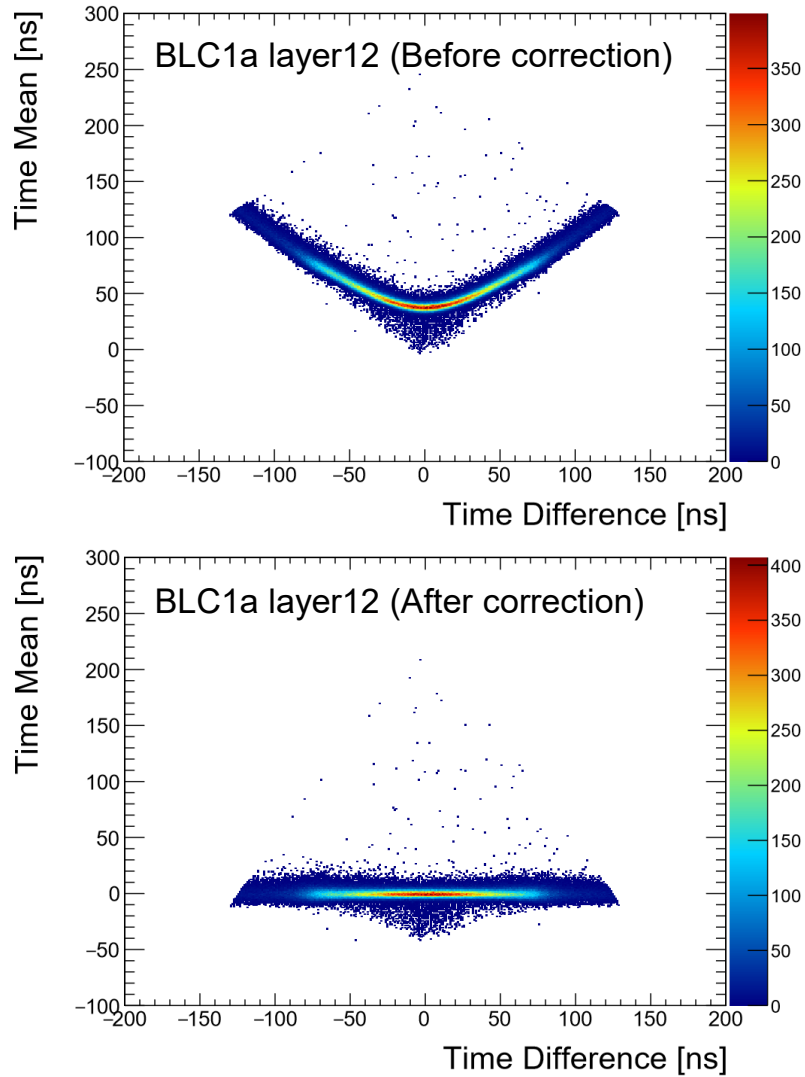
Figure 3.4: (top) A common correlation is observed between the difference in drift times and the average drift time for hits in two adjacent layers. This correlation is particularly evident in single-track events, which are identified at 0 ns using data from other chambers and counters. (bottom) A typical correlation is also seen between the difference in drift times after correction and the average drift time.

Track search at a local level

Separate local tracking is performed in BLC1, BLC2, and BPC. In the local tracking, all possible hit combinations are tried. For BLC1 and BLC2, a valid track candidate must have hits in at least five out of the eight planes in both U and V planes. In the case of BPC, hits in all eight planes are mandatory due to its non-redundant nature. The number of potential track candidates

is then narrowed down using the timing analysis and preliminary fitting employing a MWPC approach, which does not consider drift time. After the selection of the track candidates, the hit combination that yields the lowest χ^2/ndf is selected as the primary track. This method is repeated, excluding hits from already reconstructed tracks, until there are insufficient remaining hits to form an additional track.

Definition of a good track

The tracks that have been reconstructed undergo further evaluation. Firstly, they must have a χ^2/ndf value of less than 10, as shown in Fig. 3.5. Additionally, it is essential that these tracks correspond with the timing of the trigger. The distribution of track timings is illustrated in Fig. 3.6. The time frames set for associating these tracks with the trigger are $(-5, 5)$ ns for BLCs and $(-10, 10)$ ns for BPC.

3.3.3 Beam momentum reconstruction

The tracks from BLC1 and BLC2 are combined using a second-order transfer matrix, which is calculated by the TRANSPORT code and includes an extra parameter for the beam momentum. The calculation of χ^2/ndf is similar to that in Eq. (3.3), but with the addition of beam momentum as an extra variable. The optimization of χ^2/ndf is carried out using the Minuit minimization code. The distribution of χ^2/ndf is displayed in Fig. 3.7. Events are accepted if they have a χ^2/ndf value less than 20. Figure 3.8 illustrates the distribution of the reconstructed momentum.

3.3.4 Event selection

Track matching between BLC2 and BPC

Some K^- particles either decay or interact with materials after being identified by AC. To minimize such events and confirm that the BPC track is associated with the identified kaon beam, the alignment between the BLC2 and BPC tracks is checked. This comparison is made at z = -73 cm from the final focus point, which is the midpoint between BLC2 and BPC. Figure 3.9 presents the data on positional and angular alignment. For this analysis, the differences in x and y positions are chosen to be within a range from -0.75 to 0.75 cm, and the differences in dx/dz and dy/dz are selected within the range from -0.02 to 0.02.

Beam profile at final focus point

Figure 3.10 (left) shows the position distribution of the kaon beam at the final focus point extrapolated from the BPC track. In the KCDH trigger data, the target cell shape is clearly observed as shown in Fig. 3.10 (right).
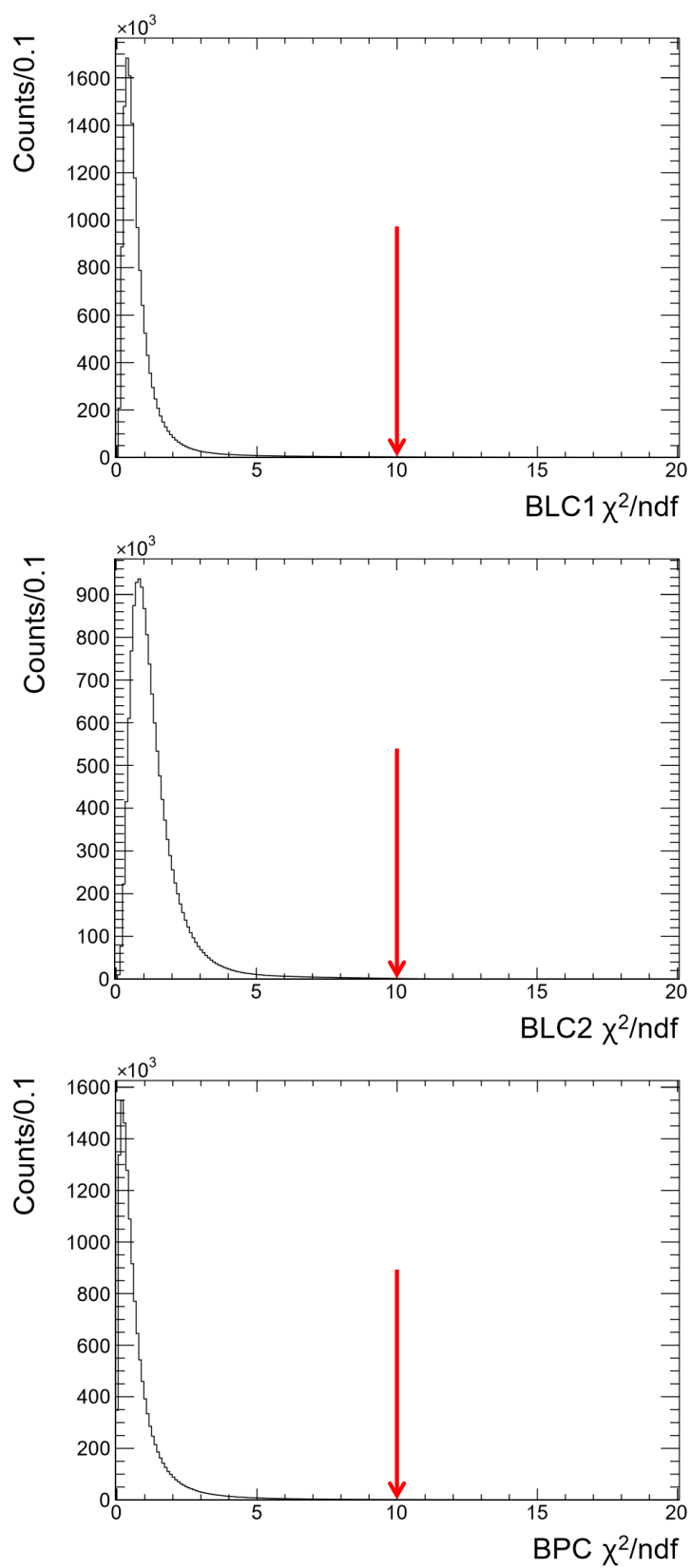
Figure 3.5: Reduced χ^2 distributions of BLC1 (top), BLC2 (middle) and BPC (bottom). Tracks with $\chi^2/ndf < 10$ were accepted.
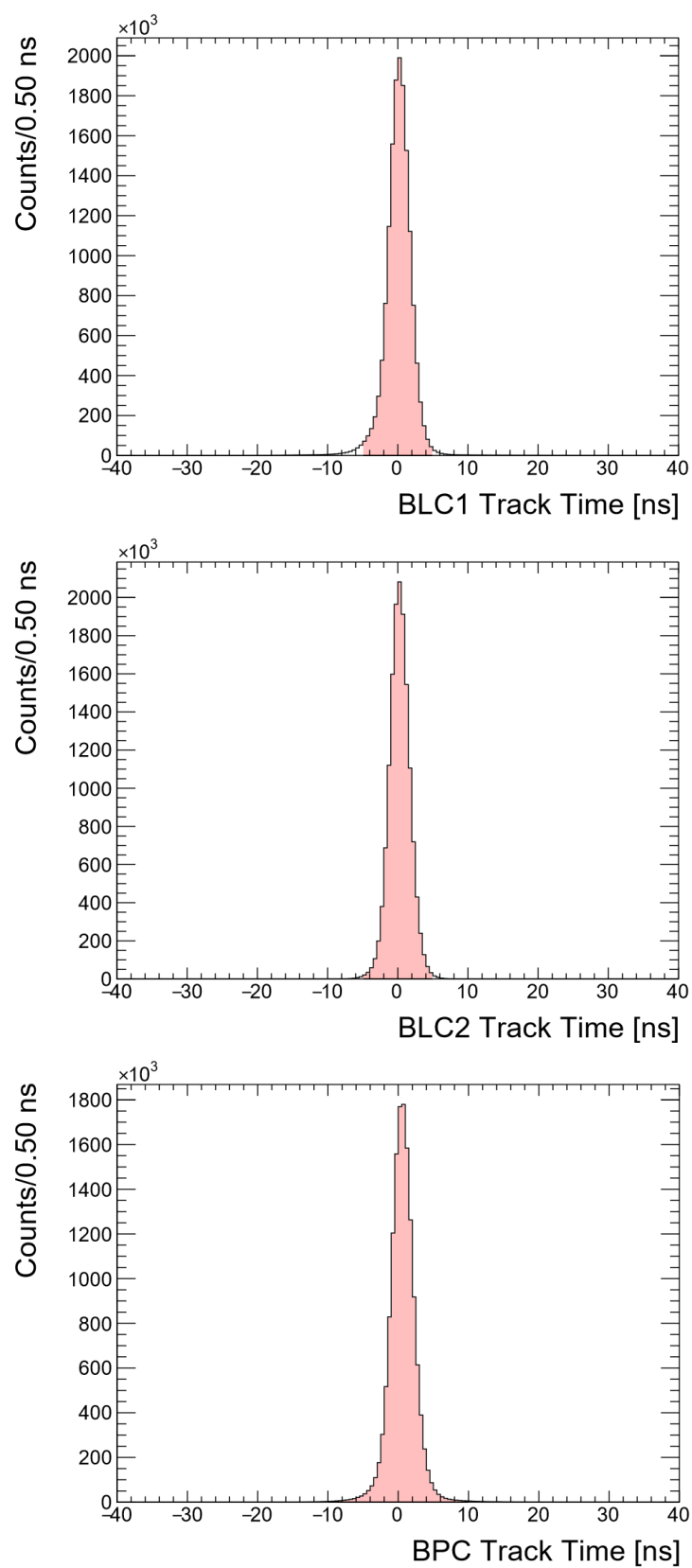
Figure 3.6: Track timing distributions of BLC1 (top), BLC2 (middle) and BPC (bottom). The timing windows of the trigger association were selected to be $(-5,5)$ ns and $(-10,10)$ ns for the BLCs and the BPC in red filled region, respectively.
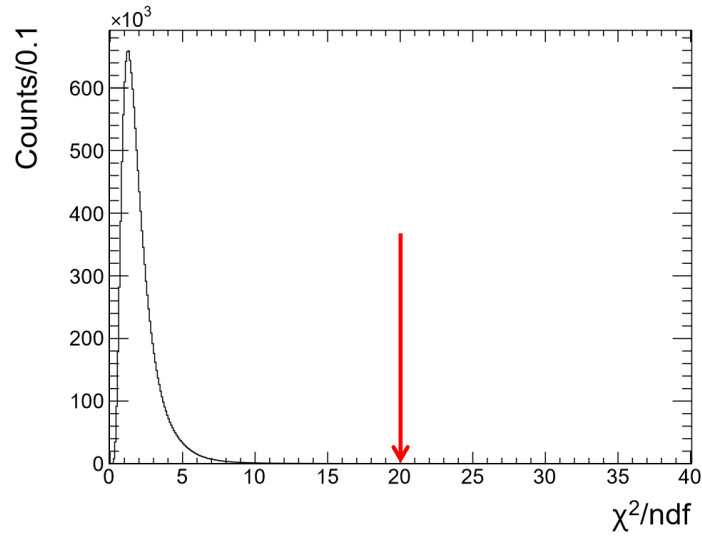
Figure 3.7: The χ^2/ndf distribution in the reconstruction of the beam momentum using BLC1 and BLC2. Events with the χ^2/ndf less than 20 are accepted.
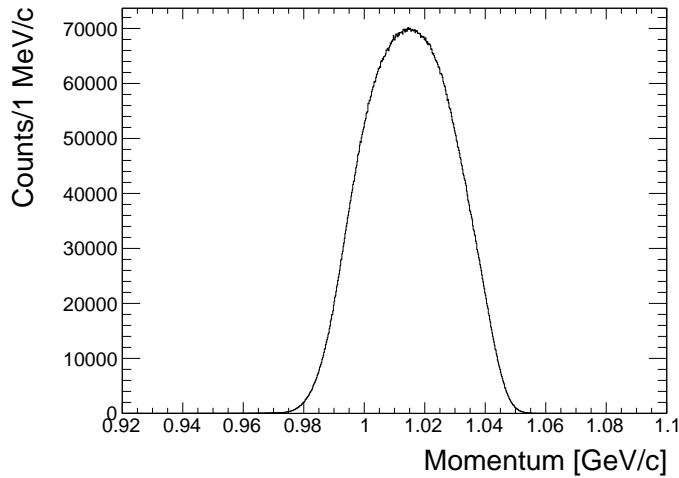
Figure 3.8: Beam momentum distribution measured with the beam spectrometer system.

3.3.5 Luminosity evaluation

Decay and reaction loss

After applying the event selection criteria mentioned above, it is ensured that the K^- particle comes to the final plane of BPC without decay. While a hit in DEF is necessary to trigger DAQ, it is important to note that charged particles resulting from K^- decays or reactions often hit DEF. Therefore, the probabilities of decay and reaction losses between the last plane in BPC (z
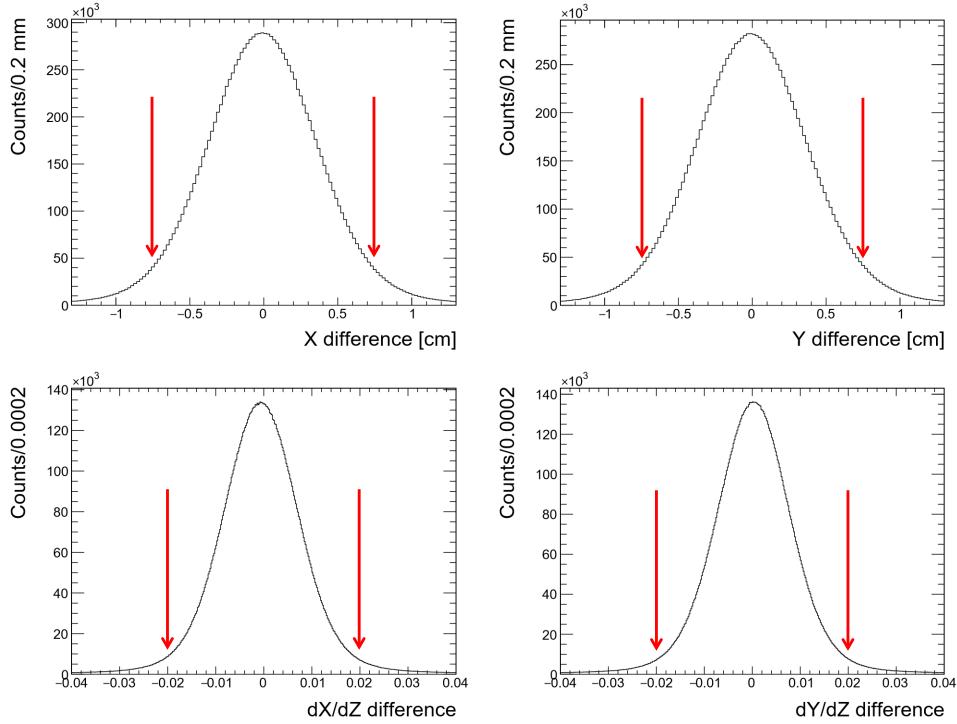
Figure 3.9: (top)The difference in position between the tracks extrapolated from BPC and BLC2 is evaluated at a point 73 cm upstream of final focus point, which corresponds to the midpoint between BLC2 and BPC. In each histogram, the acceptable range is shown by two red vertical arrows. The differences in the x and y positions are chosen to be within a range from -0.75 to 0.75 cm. (bottom)The differences in the angles dx/dz and dy/dz are limited to a range from -0.02 to 0.02.

$= -15$ cm) and the FF point ($z = 0$) have been calculated. With an average beam momentum of 1.017 GeV/c, the decay loss of kaons is calculated to be 4.5 %. A systematic error of 0.3 % arises from the relative position uncertainty of 1 cm between BPC and FF. Additionally, the impact of the beam momentum variation, approximately 3.5 %, is about 0.1 % for the kaon decay loss. For estimating the loss of the kaon beam due to reactions, the elementary $K^- N$ reaction cross section is multiplied according to the relative areal size of the nucleus, represented by $A^{2/3}$. The materials taken into the evaluation include DEF, the cap of the target vessel, the radiation shield, and the window of the target cell. The total material thickness is 0.65 g/cm^2, as detailed in Table 2.9. The rate of the reaction loss is determined to be 0.7 %, and the uncertainty related to the $K^- N$ reaction cross section is estimated to cause a 20 % systematic error.

Number of target particle

The length of the target was set to 10 cm. The traversal distance of K^- within the target length is determined by extrapolating the tracks from BPC using data from the kaon beam trigger. This

Figure 3.10: Beam image at the final focus point with requiring the kaon beam trigger (left) and KCDH trigger (right). The target image is observed by selecting the KCDH trigger.
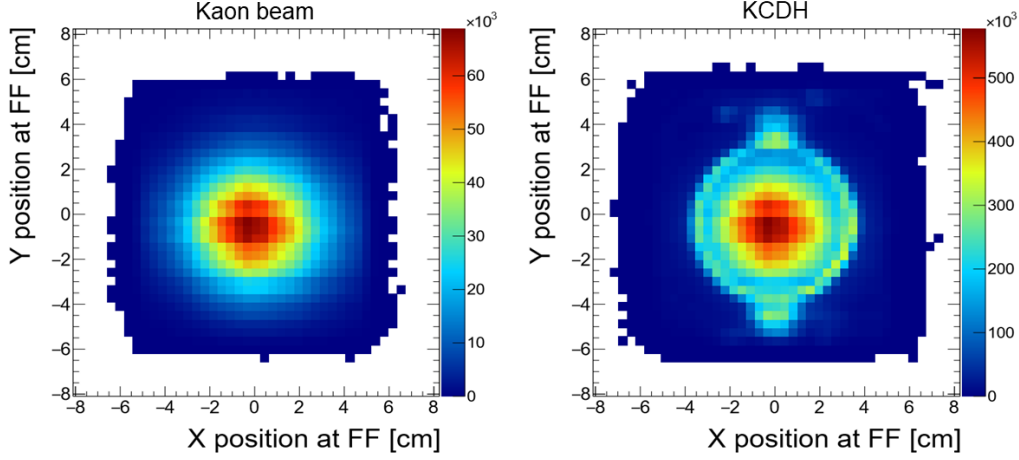
results in a effective target length of 10.03 ± 0.02 cm. The associated error is calculated based on the time fluctuations observed during the production run. The densities of the helium-4 and the helium-3 targets have been obtained as 0.1426 ± 0.0002 g/cm^3 and 0.071 ± 0.001 g/cm^3, respectively, as detailed in Sec. 2.4.

Kaon flux and integrated luminosity

The total flux of the K^- beam and the integrated luminosity are determined using the scaler count from the kaon beam trigger, the efficiency of the event selection process, and the various factors previously discussed. The criteria for event selection and their corresponding efficiencies are compiled in Tables 3.2 and 3.3. The total numbers of K^- particles incident on the targets are calculated to be $(4.03 \pm 0.11) \times 10^9$ for the helium-4 target and $(6.90 \pm 0.17) \times 10^9$ for the helium-3 target. The luminosity (L) is defined as

$$L = N_{\text{beam}} \cdot N_{\text{target}} = N_{\text{beam}} \cdot \frac{N_A \cdot d \cdot l}{M_{4,3\text{He}}}. \tag{3.4}$$

Here, N_{beam} provides effective beam number which contains survival ratio in the beam line analysis. N_{target} is number of target, d and l are the density and the length along the beam direction of the target, N_A and $M_{4,3\text{He}}$ are the Avogadro constant and the molar mass of ^{4,3}He, respectively. The integrated luminosity are estimated to be 868 ± 24 μb^{-1} and 984 ± 27 μb^{-1} for the helium-4 and helium-3 targets, respectively.

Table 3.2: Typical survival rate at each step of beam selection and summary of luminosity during the helium-4 target run. Relative uncertainties of the survival rates in the kaon beam selection are determined by the fluctuations during the experimental period.

Helium-4	number	survival rate	relative uncertainty (%)
Scalar number	9.55×10^9		
T0 single hit		0.973	0.2
TOF kaon		0.954	0.3
BLC1 single track		0.927	0.4
BLC2 single track		0.983	0.2
momentum reconstruction		0.990	0.2
BPC single track		0.972	0.3
BLC2-BPC connection		0.802	2.3
Fiducial selection at FF		0.683	1.3
decay loss		0.956	0.3
reaction loss		0.993	0.3
Total	4.03×10^9	0.422	2.7
Density (g/cm^3)	0.143		0.1
Thickness (cm)	10.03		0.2
Luminosity (μb^{-1})	868		2.7

Table 3.3: Typical survival rate at each step of beam selection and summary of luminosity during the helium-3 target run. Relative uncertainties of the survival rates in the kaon beam selection are determined by the fluctuations during the experimental period.

Helium-3	number	survival rate	relative uncertainty (%)
Scalar number	18.2×10^9		
T0 single hit		0.993	0.1
TOF kaon		0.917	0.4
BLC1 single track		0.889	0.6
BLC2 single track		0.979	0.3
momentum reconstruction		0.988	0.2
BPC single track		0.965	0.5
BLC2-BPC connection		0.765	2.1
Fiducial selection at FF		0.692	1.0
decay loss		0.956	0.3
reaction loss		0.993	0.3
Total	6.90×10^9	0.379	2.5
Density (g/cm^3)	0.071		1.0
Thickness (cm)	10.03		0.2
Luminosity (μb^{-1})	984		2.7

3.4 Analysis of cylindrical detector system

The cylindrical detector system (CDS) detects a π^- from the two-body weak decay of the hypernuclei. The particle species are identified, the momentum is analyzed and the reaction vertex is reconstructed. In addition, to check the detector performance and to validate the evaluation of the cross sections, $K_S^0 \to \pi^+\pi^-$ and $\Lambda \to \pi^- p$ are reconstructed. Analysis in this section use data with the KCDH trigger.

An analysis procedure of CDS is as follows:

1. Track finding in CDC.

2. Look for hits on CDH corresponding identified tracks within CDC.

3. Calculate a vertex point by combining the beam track with the CDC track.

4. Determine the squared mass of the tracks found in CDC.

5. Reassess the tracks in CDC, applying slewing corrections to the drift time of the CDC hits.

6. Update the squared mass calculation for the tracks.

7. Classify the type of each particle tracked in CDC using its momentum and the updated squared mass value.

8. Refine the vertex point calculation using the mass of the identified particles.

9. Determine the three-dimensional momentum vector of each CDC track at the vertex point.

3.4.1 Tracking with CDC

In a uniform magnetic field, the movement of a charged particle can be depicted as a helical path. A simulation was conducted to explore the suitability of a helical representation for illustrating the trajectory of a charged particle in CDS. The simulation, utilizing data generated in a solenoid field calculated via the TOSCA code, was analyzed with the presumption of a uniform field. This analysis verified that the helical model is capable of accurately depicting the tracks of charged particles, with a momentum precision better than 0.2 %. Consequently, the helix model has been chosen to depict tracks in CDC.

Helix parametrization

A helix in the CDC local coordinate can be parametrized as,

$$
\begin{aligned}
x(\phi) &= d_\rho \cos\phi_0 + \frac{1}{\rho}(\cos\phi_0 - \cos(\phi_0 + \phi)), \\
y(\phi) &= d_\rho \sin\phi_0 + \frac{1}{\rho}(\sin\phi_0 - \sin(\phi_0 + \phi)), \\
z(\phi) &= d_z - \frac{1}{\rho}\tan\lambda \cdot \phi,
\end{aligned}
$$

where d_ρ represents the helix distance from the pivotal point in the xy-plane, while ϕ_0 is the azimuthal angle defining the pivotal point relative to the center of the helix. ρ signifies the reciprocal of the signed radius of the helix, and d_z is the distance of the helix from the pivotal point along the z-axis. $\tan \lambda$ denotes the dip angle of the helix. The deflection angle ϕ is measured starting from the pivotal point and indicates the specific location of the charged particle on the helical path. The particle momentum is linked to the helical parameters as follows:

$$p = \frac{cB}{\rho} \begin{pmatrix} -\sin(\phi_0 + \phi) \\ \cos(\phi_0 + \phi) \\ \tan \lambda \end{pmatrix}, \tag{3.5}$$

where c is the light velocity and B is the magnetic field strength along the beam axis (z-direction).

TDC data conversion to drift length

The drift time distribution for a specific layer of CDC is depicted in Fig. 3.11. Initially, the relative time offset of each wire was aligned in the same manner as that for the beam line chambers. To convert drift time into drift length, a fifth-order polynomial function was utilized. This conversion function underwent iterative refinement, aimed at reducing systematic discrepancies in the residuals based on drift time. The fitting residuals are calculated by deducting the drift length from the nearest distance between the wire hit and the helix. Figure 3.12 illustrates the relationship between the drift length and the drift time following the adjustment of relative time, as well as the correlation between drift time and drift length. This correlation was modeled using a fifth-order polynomial function.

Track finding and χ^2 fitting

To begin with, track candidates are identified in the xy-plane by considering only the axial layers. This is followed by a circle fitting process to select the appropriate set of hits in the axial layers and to obtain a initial set of parameters of the helix, namely d_ρ, ϕ_0, and ρ. Next, the process involves locating corresponding hits in the stereo layers by examining a track in the z-ϕ plane, which aids in determining d_z and $\tan\lambda$. The final step involves conducting a helix fitting using the Minuit tool, aiming to minimize the reduced-χ^2 defined as follows:

$$\chi^2/ndf = \frac{1}{N-5} \sum_i^N \left(\frac{\delta_i - dl_i}{\sigma_i} \right)^2, \tag{3.6}$$

where N represents the total number of hits. The term δ_i denotes the minimum distance from each hit wire to the helix track, while dl_i refers to the drift length. σ_i indicates the spatial resolution for each hit. The resulting distribution of χ^2/ndf is displayed in Fig. 3.13, and tracks that have the χ^2/ndf value less than 30 are classified as satisfactory tracks. Each track must have a minimum of one hit in every axial super layer. Furthermore, a track must comprise at least five hits in the stereo layers and a total of 10 hits or more.
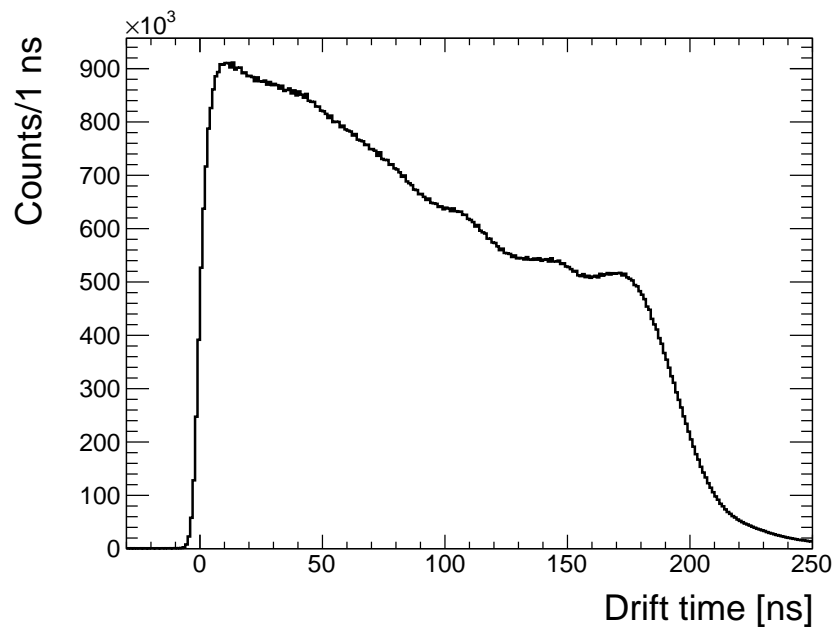
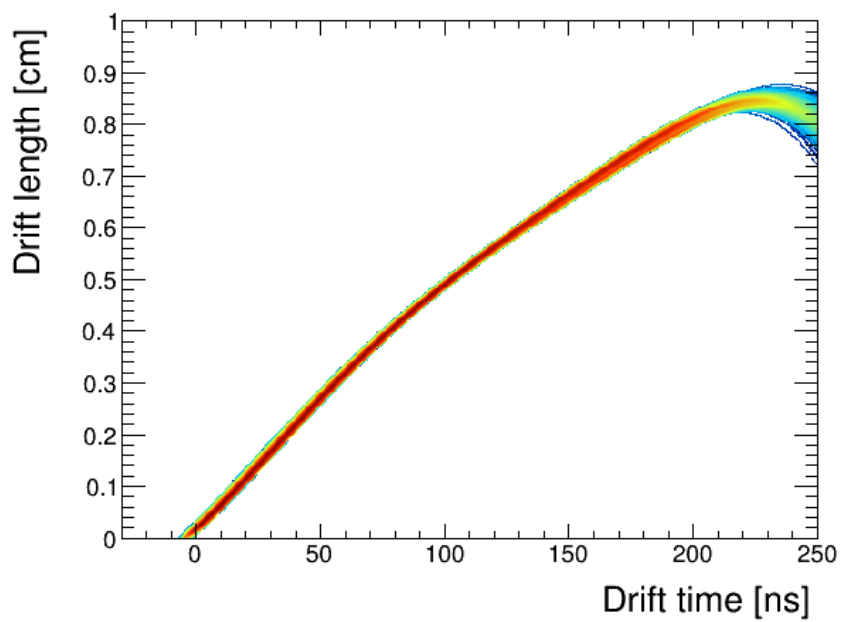**Figure 3.11:** Drift time distribution of a typical CDC layer.

Figure 3.12: Correlation between the drift length and the drift time. The correlation was fit by using fifth-order polynomial function.
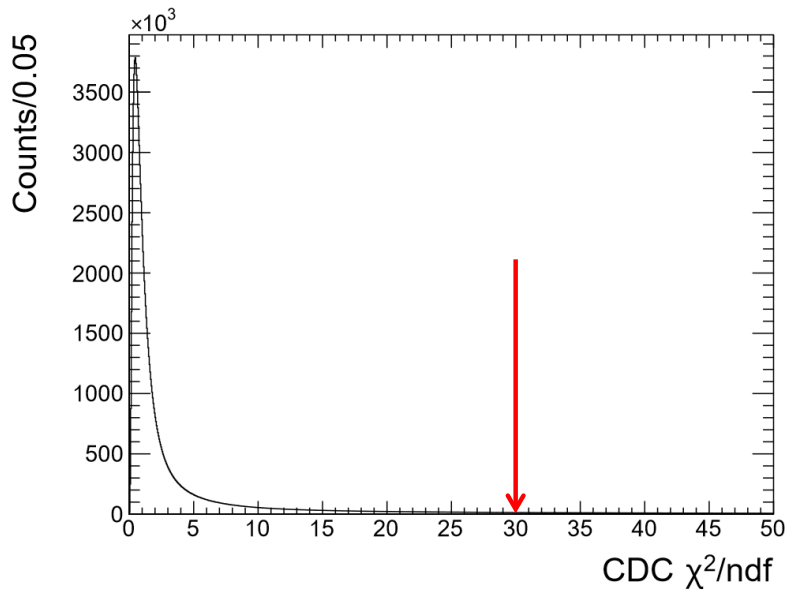
Figure 3.13: Reduced χ^2 distribution of the CDC tracks in the helix tracking. Tracks with $\chi^2/ndf <30$ are accepted.

CDC tracking efficiency

The tracking efficiency of CDC is estimated using the cosmic-ray. A special trigger was set to acquire cosmic-ray data during off-spill during beam time. The event was selected when two CDH on opposite sides of CDC had hits. Figure 3.14 shows a schematic view of the triggered event. This allows the selection of events that pass through space near the center of the CDC, and allows the estimation of the number of tracks to be two per cosmic-ray. In other words, twice the number of events with the two CDH hits is the expected number of tracks. One possible way to estimate the efficiency of CDC tracking is by calculating the ratio of the number of tracks to the number of events. The result is 98.1$\pm$ 0.2 % for the helium-4 target runs and 97.7 $\pm$ 0.3 % for the helium-3 target runs. The errors are statistical uncertainty.

3.4.2 Associated hit search in CDH

After establishing a track in CDC, the next step involves searching for corresponding hits in CDH based on the projected trajectory of the CDC track. Figure 3.15 presents the correlation of the azimuthal angle for CDH at a radius of $r = 544$ mm, specifically when there is a single track detected in CDC and a solitary hit in CDH. The efficiency of this matching process exceeds 99 %. CDC tracks that align with multiple CDH hits are typically considered, with verification of this matching usually performed at the outer radius of CDH at $r = 574$ mm. In the case, where several CDH hits correspond to a single CDC track, the timing for the CDC track is determined by the segment with the earliest timing among the hits.

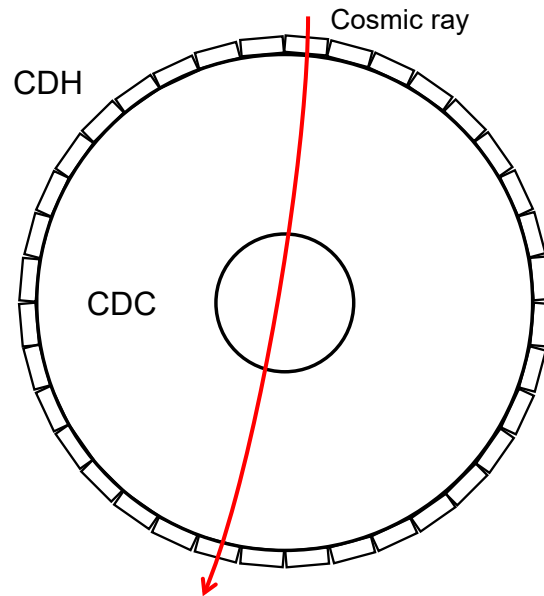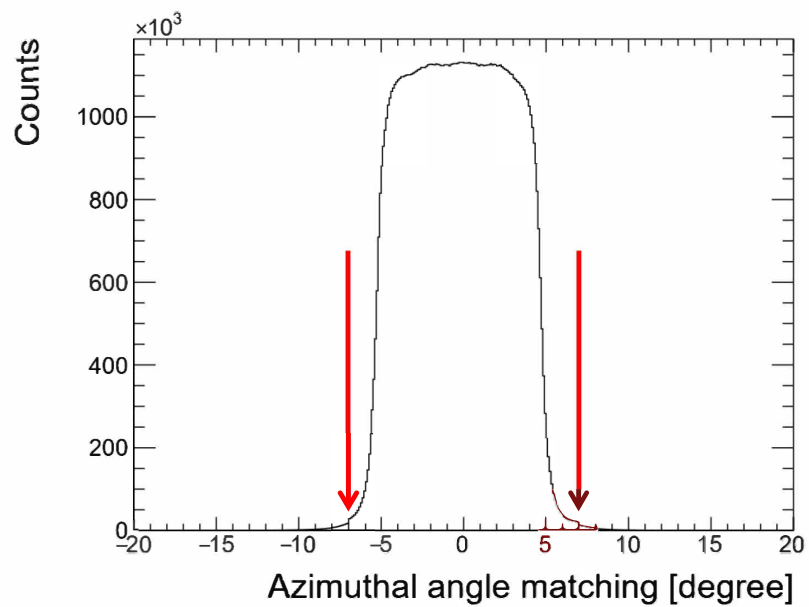**Figure 3.14:** A schematic view of a cosmic-ray passing through CDC and CDH.

Figure 3.15: Azimuthal position matching between a CDC track and a CDH hit. Events between two red arrows are accepted. The segment size of CDH corresponds to $\pm 5°$.

3.4.3   Vertex reconstruction

Reconstructing the vertex of the CDS track is essential for determining the velocity and the initial momentum vector of the particle. There are two scenarios for pinpointing the vertex point within CDS. The first scenario occurs when the CDC track originates directly at the K^- beam reaction point. In that case, the vertex is identified as the point nearest to both the CDC and beam tracks, as illustrated in Fig. 3.16 (left). The second scenario involves a primary K^- reaction producing an intermediate particle that subsequently decays into two charged particles after traveling a certain distance. In this situation, the nearest point between the two CDC tracks is computed. The momentum vector of the parent particle is deduced by summing the momentum vectors of these two CDC tracks. The vertex in this case is defined as the point closest to both the combined momentum vector of the parent particle and the beam track, as depicted in Fig. 3.16 (right).
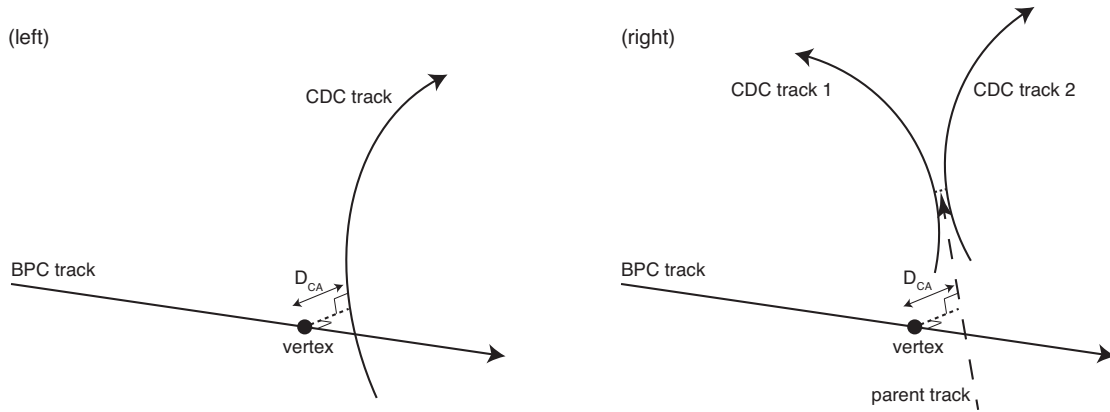

Figure 3.16: In terms of defining the vertex in the particle tracking: Single CDC Track Scenario (left): When only one track is detected in CDC, the vertex is identified at the point on the BPC track that lies nearest to the CDC track. Two CDC Tracks Scenario (right): In cases where there are two tracks in CDC, the point where these two tracks are closest to each other is determined.

CDH calibration

The particle velocity is calcurated by employing its observed momentum (p) and mass (m_x) as,

$$\beta_{calc} \quad = \quad \sqrt{\frac{m_x^2 + p^2}{p^2}}. \tag{3.7}$$

Adjustments are made to the timing offsets and time-walk effects to ensure that the discrepancy between the experimentally measured beta β as per Eq. (3.8) and the theoretically calculated β_{calc} from Eq. (3.7) is nullified, with these adjustments being based on observations of pions.

3.4.4 Fine corrections

To reduce systematic discrepancies arising from different types of particles and the particle momenta, two specific adjustments are implemented on the drift time measured by CDC.

Re-timing of the CDC drift times

Because the T0 timing sets the start point for TDC of CDC, the TDC readings from CDC are divided into two components: the drift time and the flight time between T0 and the CDC cell. The drift time is derived by computing and subtracting the flight time, which involves using the helical path of the particle, the timing of the hit in CDH, and the particle velocity as determined by Eq. (3.8).

Time-walk effect of CDC drift times

The time-walk effect, commonly observed in photon sensors and typically corrected using the relationship with pulse charge, is also expected to occur in a drift chamber. While the charge itself do not be documented in the setup, its impact can be inferred by examining the time-over-threshold (TOT) data. As depicted in Fig. 3.17, there is a noticeable correlation between TOT and the tracking residual, which has been converted to a time scale. This correlation is accounted for by employing a fifth-order polynomial function for fitting, as demonstrated in the same figure.
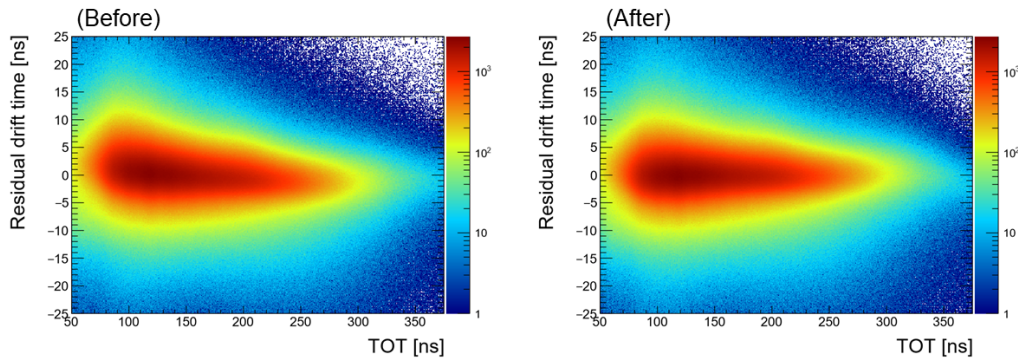

Figure 3.17: Distribution of the residual drift time in relation to TOT for CDC. Before Correction (left): There is a correlation between the residual drift time and TOT. The correlation is corrected using a fifth-order polynomial function. After Correction (right): This depicts the distribution post-application of the correction.

3.4.5 Fiducial volume selection

Figure 3.18 displays the vertex distributions in the xy, zx, and zy planes. Within these distributions, several key structures are seen, such as DEF located at $z = -13.5$ cm, as well as the

vacuum vessel, the thermal radiation shield, and the helium transfer pipes. The fiducial volume in the helium target is specified with dimensions of a 30 mm radius and a 100 mm length. The fiducial volume is carefully positioned away from the beryllium cylinder of the target cell to minimize contamination from other materials. The length and positioning of the fiducial volume in the z-direction are specifically chosen to align with the beryllium cylinder.

3.4.6   Particle identification

The velocity β and the mass-square M^2 for a track in CDC are determined using the following equations.

$$\beta = \frac{L_{\mathrm{CDC_{in}-CDH}}}{((T_{\mathrm{CDH}} - T_{\mathrm{T0}}) - T^{\mathrm{calc}}_{\mathrm{T0\text{-}vertex}} - T^{\mathrm{calc}}_{\mathrm{vertex-CDC_{in}}}) \times c}, \tag{3.8}$$

$$M^2 = p^2 \times \frac{1 - \beta^2}{\beta^2}, \tag{3.9}$$

where $L_{\mathrm{CDC_{in}-CDH}}$ refers to the length of the helical track from the CDC entry point at a radius of 151 mm to CDH. $T_{\mathrm{CDH}} - T_{\mathrm{T0}}$ represents the recorded flight time between CDH and T0. $T^{\mathrm{calc}}_{\mathrm{T0\text{-}vertex}}$ and $T^{\mathrm{calc}}_{\mathrm{vertex-CDC_{in}}}$ are the calculated flight times from T0 to the vertex, and from the CDC entry point to CDH, respectively. Adjustments for changes in velocity and curvature due to energy losses are included in these calculations. The resulting momentum versus mass-square distribution, as shown in Fig. 3.19, clearly distinguishes between pions, kaons, protons, and deuterons.

3.4.7 K^0_{S} and Λ reconstruction

To illustrate the effectiveness of CDS, the reconstructed invariant masses for pairs of $\pi^+\pi^-$ and π^-p are presented in Figs. 3.20 and 3.21, respectively. In the invariant mass distributions, distinct peaks corresponding to K^0_{S} and Λ are visible. The locations of these peaks are consistent with the values provided by PDG within an accuracy of 1 MeV/c^2.
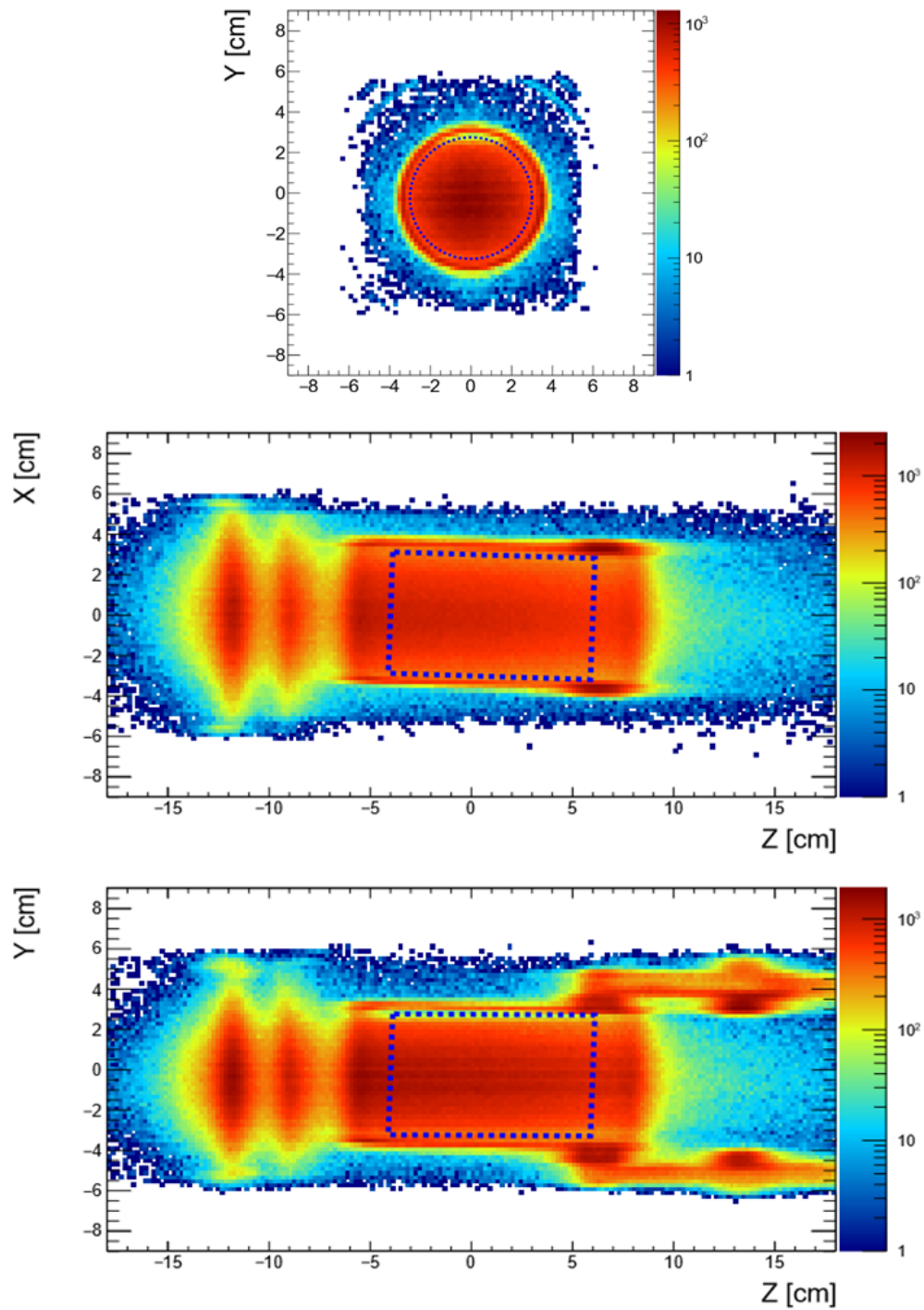
Figure 3.18: Reconstructed vertex distribution. Target cell is filled with helium-4.
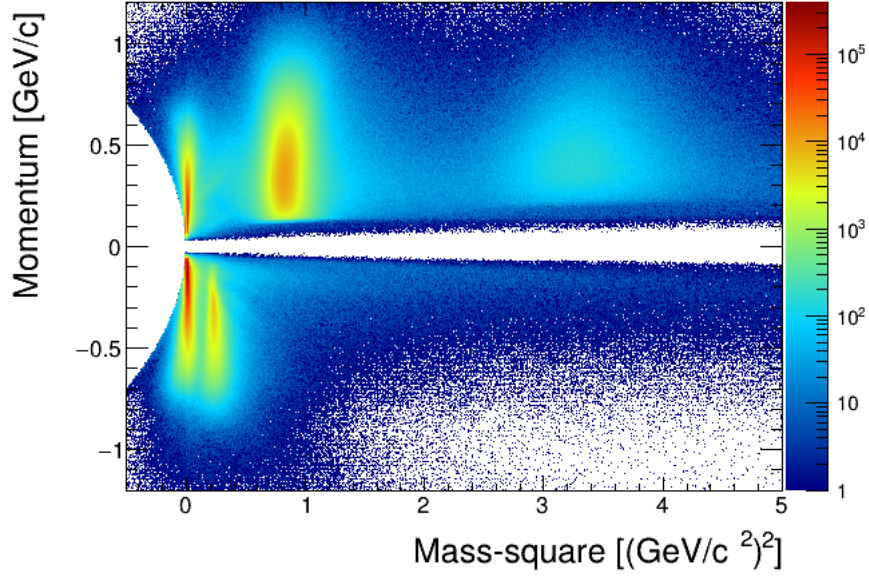
Figure 3.19: Particle-identification plot for CDS. π^+, protons and deuterons are clearly separated in the positive momentum side, while π^- and K^- are clearly seen in the negative side.

Figure 3.20: The distribution of invariant mass for $\pi^-\pi^+$ pairs identified by CDS is represented. The fitting of this distribution, indicated by the red and blue dotted lines, employs a combination of a Gaussian function for the peak and a third-order polynomial for the background. The determined mass and resolution of this peak are 497.41 MeV/c^2 and 6.2 MeV/c^2, respectively.
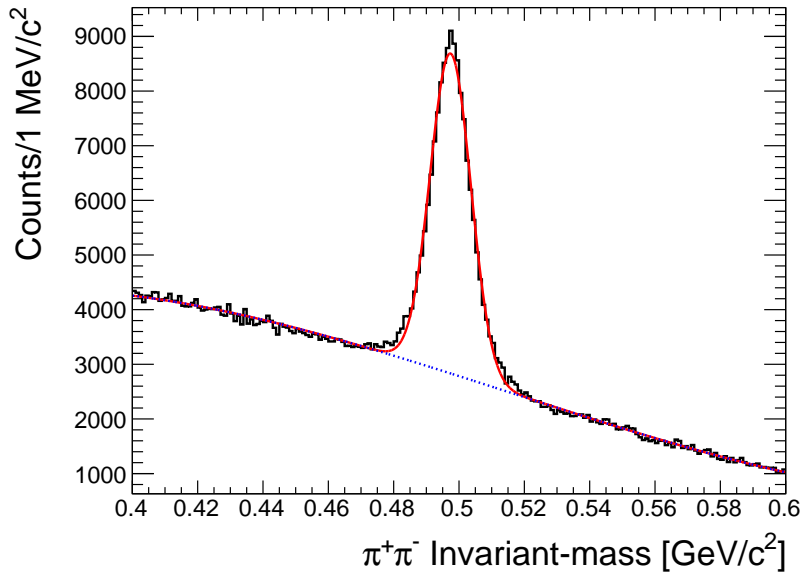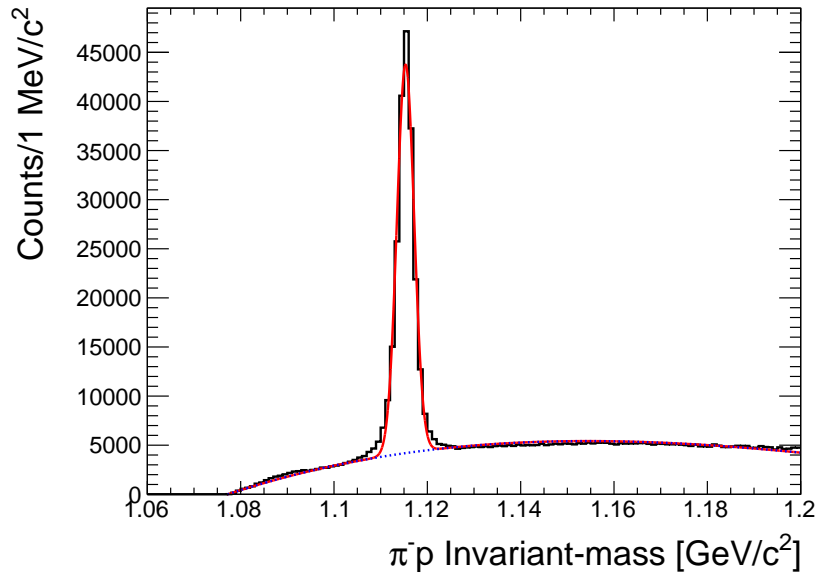
Figure 3.21: The distribution of invariant mass for $\pi^- p$ pairs identified by CDS is represented. The fitting of this distribution, indicated by the red and blue dotted lines, employs a combination of a Gaussian function for the peak and a third-order polynomial for the background. The peak, which arises from the decay of Λ, is accurately replicated in the model. The determined mass and resolution of this peak are 1115.33 MeV/c^2 and 1.8 MeV/c^2, respectively.

3.5   Analysis of forward calorimeter

3.5.1   Energy calibration for PbF_2

The PbF_2 calorimeter is calibrated using π^-s and electrons mixed in the beam. The π^- energy deposit is used to adjust the relative energy of each segment, while the electron beam is used to determine the absolute energy scale. The criteria for selecting the π^- beam is that BTC located downstream of the PbF_2 calorimeter has a hit, and only one of the 40 segments of the PbF2 calorimeter has a hit. This requirement ensures that the π^- beam passes through one segment with an almost fixed pass length.

Figure 3.22 (a) and (b) show the distributions of the π^- energy deposit in a PbF_2 segment after the relative energy calibration, when the data are obtained for helium-4 target and helium-3 target, respectively. The energy resolutions at the π^- peak are 9 % and 12 %, respectively. The difference between the two datasets could be due to the coupling method employed between the PbF_2 crystal and PMT. It is worth noting that UV-cured resin was used for the helium-4 run and silicon rubber was used for the helium-3 run. The light yield is roughly 20% less with a silicon rubber.
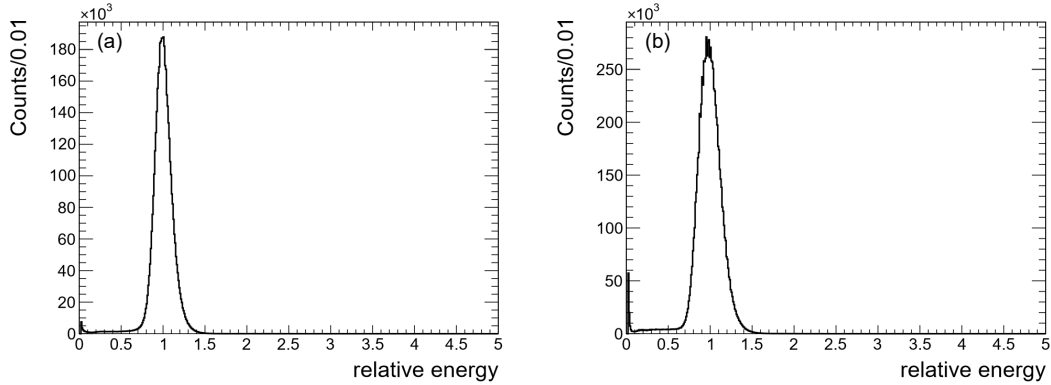

Figure 3.22: The energy distribution of the PbF_2 calorimeter normalized to unity for the π^- energy deposit with (a) the helium-4 target and (b) the helium-3 target. The energy resolution evaluated at the π^- peak is 9 % and 12 %, respectively.

As for the electron beam, the energy spreads over multiple segments due to the electromagnetic shower, where the Moliere radius characterizes a typical size of the shower. The present analysis defines the largest energy-deposit segment as the primary segment and the surrounding eight segments as secondary segments, forming a cluster as shown in Fig. 3.23. Then, the energy of the cluster (dE_{cluster}) is calculated using the energies of the primary segment ($dE_{primary}$) and the secondary segments ($dE_{\text{secondary}}$),

$$dE_{\text{cluster}} = dE_{\text{primary}} + \sum dE_{\text{secondary}}. \tag{3.10}$$

Here, only segments with energy above a certain threshold are summed up. If the primary segment is in the outer segments, the number of neighboring segments is 3 or 5. Therefore, the energy of the cluster is calculated with 4 and 6 segments, respectively.
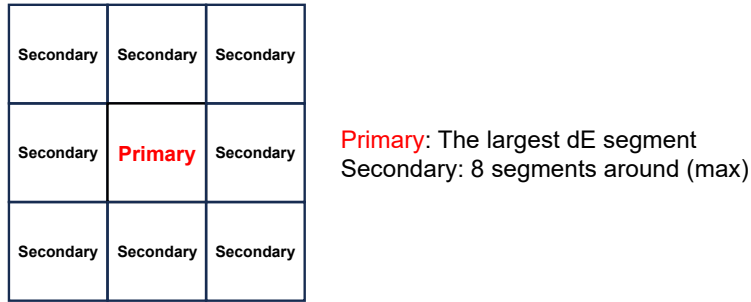
Figure 3.23: A conceptual diagram of clustering of PbF_2 calorimeter.

A minimum selection condition for the electron beam analysis is set: the injected particle into the PbF_2 calorimeter is identified as a charged particle by requiring a hit of VETO. Figure 3.24 shows the energy distribution of the PbF_2 cluster with the selection. A small peak observed in the large energy region can be interpreted as originating from the 1 GeV/c electron beams. The absolute energy of the energy distribution is calibrated so that the electron beam energy is reconstructed correctly. The energy resolution at 1 GeV/c, evaluated by fitting the electron peak, is 4.8 %(a) and 5.2 %(b) for helium-4 and helium-3 data, respectively. Fig-
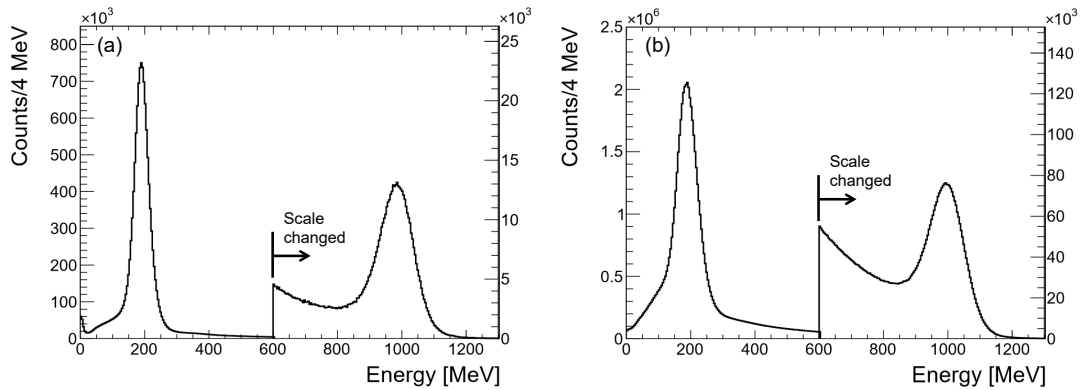
Figure 3.24: The energy distribution of the PbF_2 calorimeter for (a) helium-4 data and (b) helium-3 data. The vertical scale above 600 MeV is on the right axis. The peak near 1000 MeV is the electron beam events, and the peak near 200 MeV is the π^- beam events. The energy resolution at the electron peak is (a) 4.8 % and (b) 5.2 %, respectively.

ure 3.25 summarizes the energy resolution at the π^- and the electron peaks. The blue dotted line is the resolution function obtained from the test experiment at ELPH with positron beams as described in Sec. 2.6.1. The resolution at J-PARC is in a reasonable range expected from the test experiment.

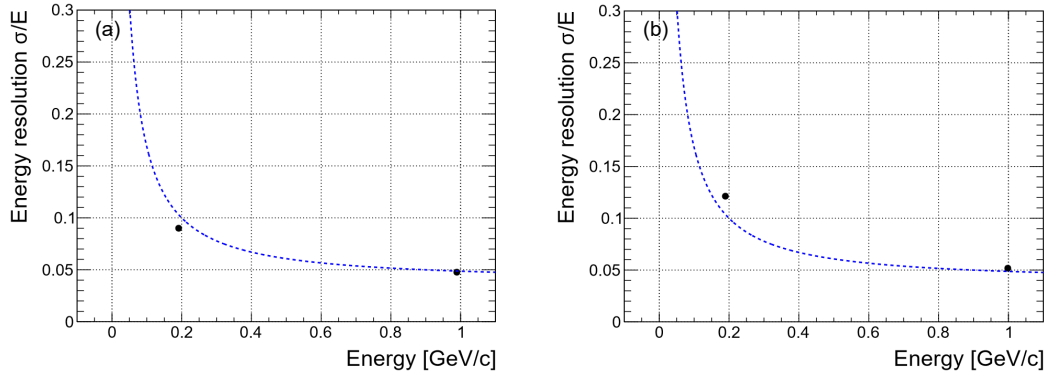**Figure 3.25:** The energy resolution at the π^- and the electron beam peaks for (a) helium-4 data, and
(b) helium-3 data. The blue dotted line is a resolution function evaluated from the test
experiment at ELPH.

3.5.2   gamma-ray selection

Gamma-rays in the production run are identified by excluding charged particles with VETO de-
tector installed in front of the PbF$_2$ calorimeter. Then, the total energy deposit is obtained with
the same clustering analysis as electrons. Figure 3.26 shows the energy distribution of the PbF$_2$
calorimeter for neutral particles obtained with the physics trigger. In both the helium-4 data (a)
and helium-3 data (b), it is shown that the gamma-ray energy distribution extends to approx-
imately 900 MeV, indicating the successful detection of high-energy gamma-rays associated
with hyperon productions via the (K^-, π^0) reaction.
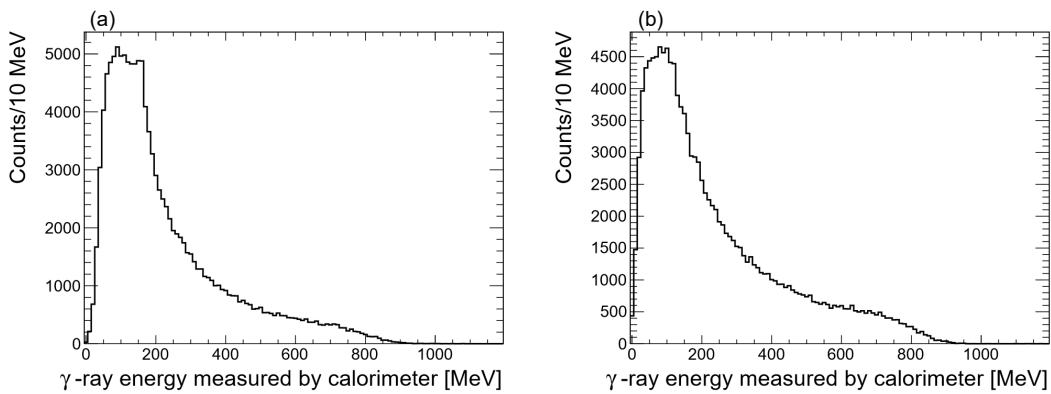

Figure 3.26: The energy distribution of the PbF$_2$ calorimeter with the $K \otimes \gamma$ trigger for (a) the helium-4
data and (b) the helium-3 data.

3.5.3 Monte-Carlo simulation of calorimeter response

To optimize the $^{3,4}_{\Lambda}$H event set an energy threshold to select high-energy gamma-rays. The selection efficiency will be evaluated based on a Monte Carlo simulation calculation. The GEANT4 toolkit was used for the Monte Carlo simulation. Gamma-rays with various energies $E_{\rm in}$ were injected, and energy depositions in the PbF$_2$ calorimeter dE were calculated using the same clustering method as for the beam data. Figure 3.27 shows the distribution of irradiated energy. The energy resolution of the PbF$_2$ calorimeter is introduced to match the experimental results. Figure 3.28 shows the energy resolution of the PbF$_2$ calorimeter in the simulation calculation. The blue dotted line is a function of energy resolution based on the results of a test experiment conducted at ELPH. Then, the energy scale of the beam data is modified based on the relationship between the actual irradiated energy $E_{\rm in}$ and the energy deposition dE as shown in Fig. 3.29.

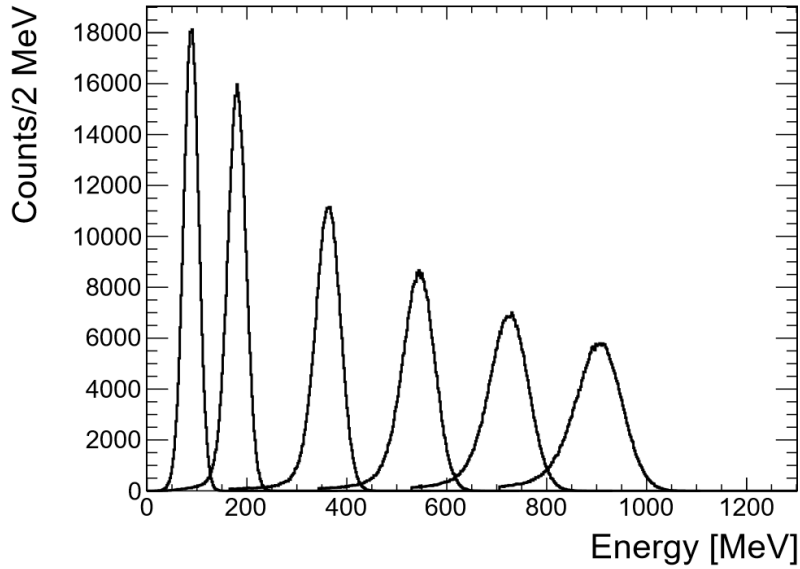**Figure 3.27:** The energy resolution of the PbF$_2$ calorimeter in the simulation.
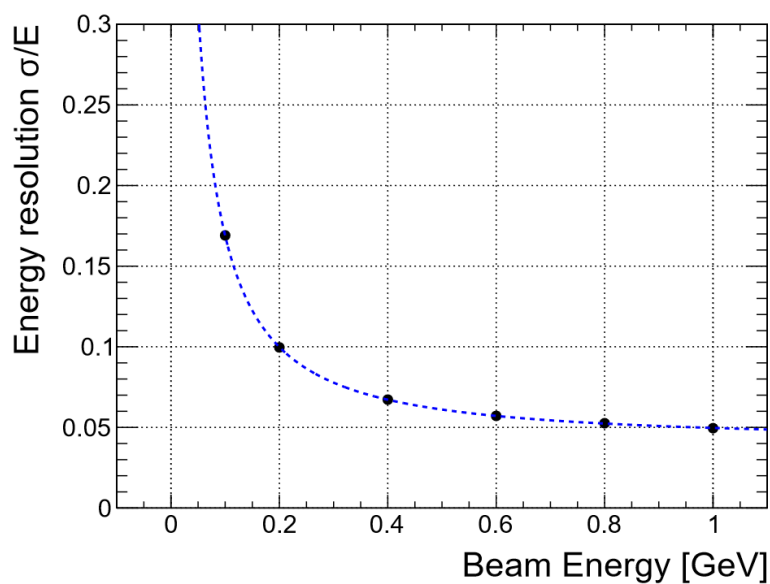
Figure 3.28: The energy resolution of the PbF$_2$ calorimeter in the simulation. The blue dotted line is a function of energy resolution based on the results of a test experiment conducted at ELPH.
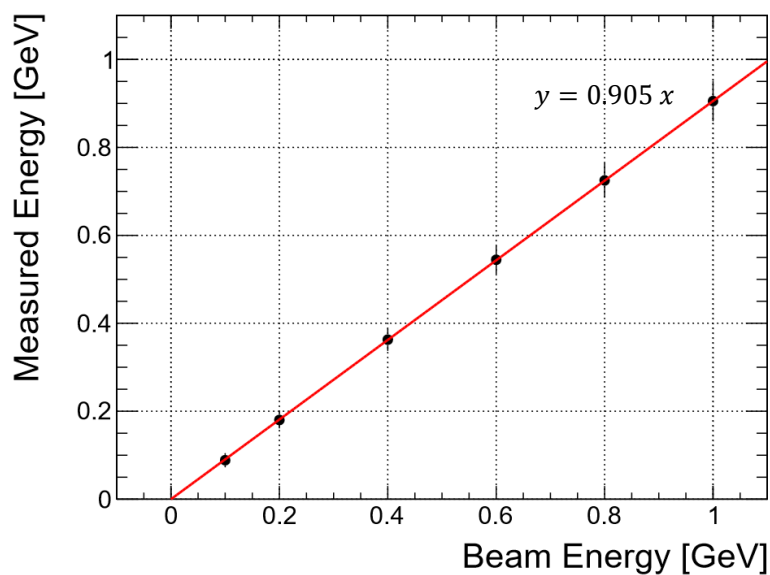

Figure 3.29: The relationship between the actual irradiated energy E_{in} and the energy deposition dE in the simulation.

Chapter 4

Analysis of the $(K^-, \gamma\pi^-)$ event

This section describes the event selection for the analysis of the production of hypernuclei with the physics trigger ($K_{\text{beam}} \otimes \gamma_{\text{forward}}$) data. The production events of the Λ hypernuclei, $^3_\Lambda$H and $^4_\Lambda$H, via the in-flight (K^-, π^0) reaction, are extracted, and the background is estimated. The helium-4 dataset is examined first due to its larger production cross section of $^4_\Lambda$H and higher branching ratio to the two-body MWD. The same analysis procedure is then applied to the helium-3 dataset for $^3_\Lambda$H.

4.1 Criteria of event selection for hypernucleus production

Instead of fully reconstructing the π^0 momentum, the (K^-, π^0) reaction is identified by detecting a high-energy gamma-ray from the π^0 decay at the forward angle with the PbF$_2$ calorimeter. The gamma-ray detection alone is insufficient to isolate the hypernucleus production events from the quasi-free hyperon production events. Therefore, π^- detected by CDS is additionally analyzed to identify the two-body MWD of produced hypernuclei. Because the hypernucleus is produced with a small recoil momentum by the (K^-, π^0) reaction if π^0 is emitted at the forward angle, the hypernucleus stops immediately (< 10 ps) after the production and produces monochromatic π^- in the two-body MWD.

4.1.1 π^- momentum distribution

Figure 4.1 shows a two-dimentional PID plot for particles detected by CDS for helium-4 target with the physics trigger. To avoid muon contamination, a threshold of 0.015 $(\text{GeV}/c^2)^2$ or higher with mass-square is selected. Figure 4.2 shows the π^- momentum distribution for the helium-4 dataset with the physics trigger data. A clear peak at around 133 MeV/c represents the contribution of π^- from the two-body decay of $^4_\Lambda$H $\to^4$ He $+ \pi^-$. $^4_\Lambda$H events are identified, but the amount of backgrounds is considerably large. Event selections will be optimized in the following subsections in terms of signal-to-noise ratio.
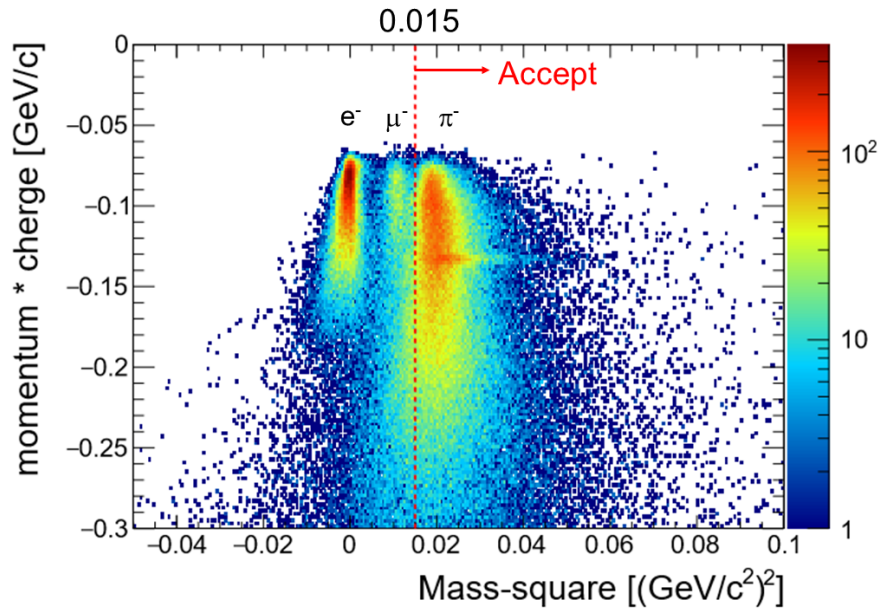
Figure 4.1: Two-dimentional PID plot for particles detected by CDS for helium-4 target with the physics trigger data. The red dotted line represents a 0.015 $(\text{GeV}/c^2)^2$ threshold for the π^- selection.

Figure 4.2: π^- momentum distribution for the helium-4 dataset with the physics trigger data. A clear peak at around 133 MeV/c represents the contribution of π^- from the two-body decay of $^4_\Lambda\text{H} \rightarrow ^4\text{He} + \pi^-$.

4.1.2 High-energy gamma-ray selection with PbF$_2$ calorimeter

Events with high energy gamma-rays are selected based on the energy deposited in the PbF$_2$ calorimeter (E_{calo}). Figure 4.3 shows the correlation between the π^- momentum and the energy deposit of the PbF$_2$ calorimeter. $^4_\Lambda$H signals are clearly observed as a vertical line at around 133 MeV/c.

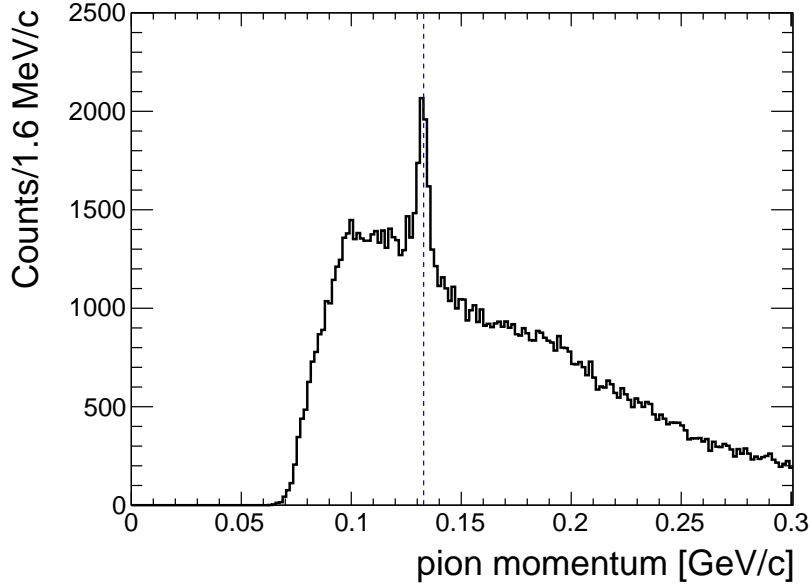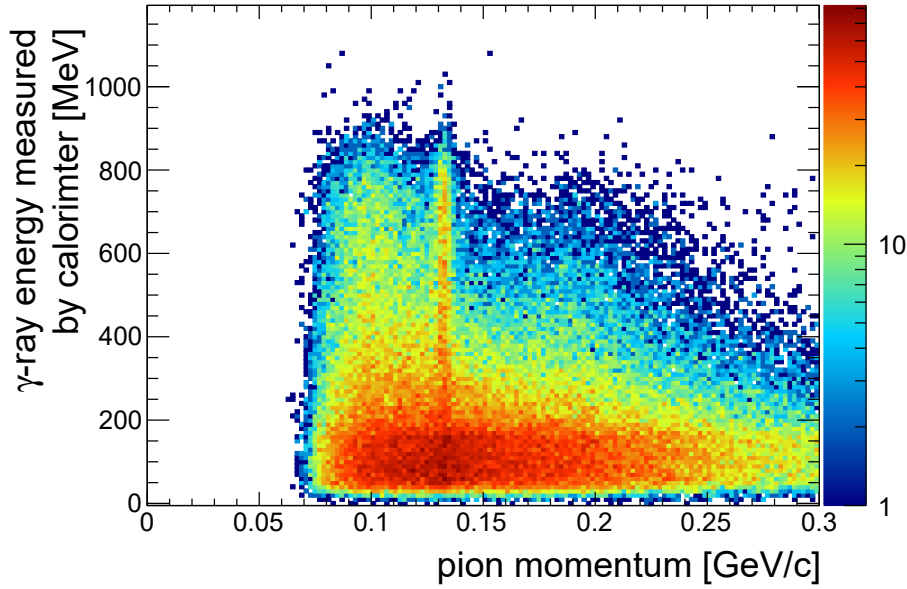**Figure 4.3:** Correlation between the π^- momentum and the energy deposit of the PbF$_2$ calorimeter for the helium-4 dataset. The horizontal axis represents the π^- momentum, while the vertical axis displays the energy deposited in the PbF$_2$ calorimeter.

To optimize the cutting condition for PbF$_2$ energy, a signal-to-noise ratio and a survival efficiency of the signal are used. The signal-to-noise ratio (S/N) is defined as the number of hypernuclei production signals (S) divided by the number of noises or backgrounds (N). The numbers S and N are derived by fitting the peak region of the π^- momentum distribution by a Gaussian and a third polynomial functions. The numbers are integrated over a $\pm 3\sigma$ region. The survival efficiency of the signal (ε) is calculated by dividing the number of signals obtained after the cut by the number of signals without the cut. The figure-of-merit (s^2/S_0) is determined as follows,

$$s^2 = \frac{S^2}{\sigma_S^2} = \frac{S^2}{(\sqrt{S+N})^2} = \frac{S^2}{S+N} = \frac{S}{N}\frac{\varepsilon S_0}{\frac{S}{N}+1}, \tag{4.1}$$

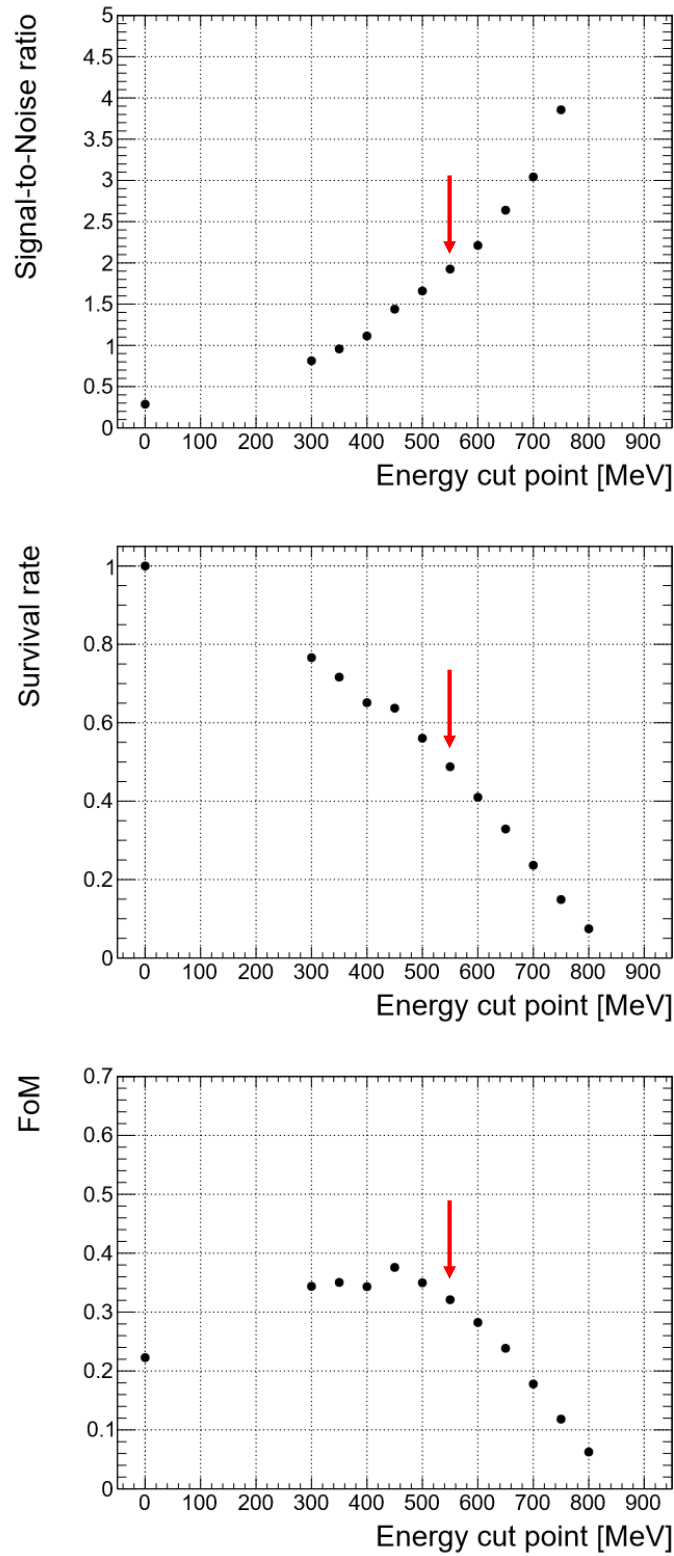$$\frac{s^2}{S_0} = \frac{S}{N}\frac{\varepsilon}{\frac{S}{N}+1}. \tag{4.2}$$

Figure 4.4: Signal-to-noise ratio (top), survival efficiency (middle) and figure of merit (bottom) against the cut value of the energy deposit in the PbF$_2$ calorimeter for the helium-4 dataset.

Figure 4.4 (top) shows how the signal-to-noise ratio changes with the cutting condition of the gamma-ray energy deposit in the PbF$_2$ calorimeter. Figure 4.4 (top) suggests that a higher cut value of energy gives better signal-to-noise ratio. Figure 4.4 (middle) shows the survival efficiency of the signal. The plot indicates a reduction of the survival efficiency of the signal as the gamma-rays energy is increased. Figure 4.4 (bottom) shows the figure of merit (FoM). Based on the results in Fig. 4.4, FoM has the largest values in the energy range from 300 to 500 MeV. The cut energy was selected to be larger than 550 MeV for two reasons. One reason is that the optimum range of the cut energy is expected to be shifted to higher energy if overall S/N ratio is smaller than that in Fig. 4.4 (top) due to the functional shape of Eq. (4.2). It is the case of the helium-3 target dataset. Second reason is that the gamma-ray energy spectrum of the PbF$_2$ calorimeter above 550 MeV is well reproduced by the Monte-Carlo simulation calculation to be discussed in Sec. 4.5.1, while the energy region below 550 MeV is not reproduced by the Monte-Carlo simulation. The understanding of the signal survival efficiency and the amount of the background by the Monte-Carlo simulation calculation is essential to obtain reliable results in this study. Figure 4.5 compares the π^- momentum distributions before and after the event selection by the energy deposit of the PbF$_2$ calorimeter. The signal-to-noise ratio is improved by a factor of roughly 6.7 with a signal efficiency of 48.8 %.
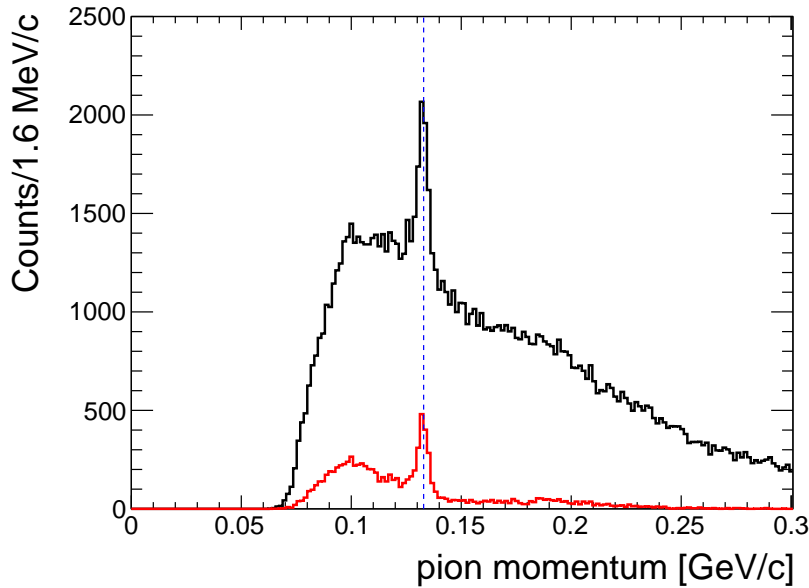

Figure 4.5: Change of the π^- momentum distribution for the helium-4 dataset after the gamma-ray energy selection with the PbF$_2$ calorimeter. The black line represents the distribution before the selection, while the red line represents the distribution after the selection.

4.1.3 DCA selection between K^- beam and π^- tracks

In the (K^-, π^0) reaction, a hypernucleus is produced with a small recoil momentum and quickly stops inside the target after moving a few mm before its decay. Therefore, the production point of the hypernucleus and the decay point are very close, giving a small value of the distance of the closest approach (DCA) between the K^- beam track measured by BPC and the π^- track in CDC. Hyperons from the background quasi-free production processes fly more distance before their decays, resulting in larger DCAs. Figure 4.6 shows the DCA distribution between the K^- beam track and the decay π^- track after the high-energy gamma-ray selection. Figure 4.7 shows the correlation between the π^- momentum and DCA, where signal events at around 133 MeV/c are concentrated in a small DCA region.
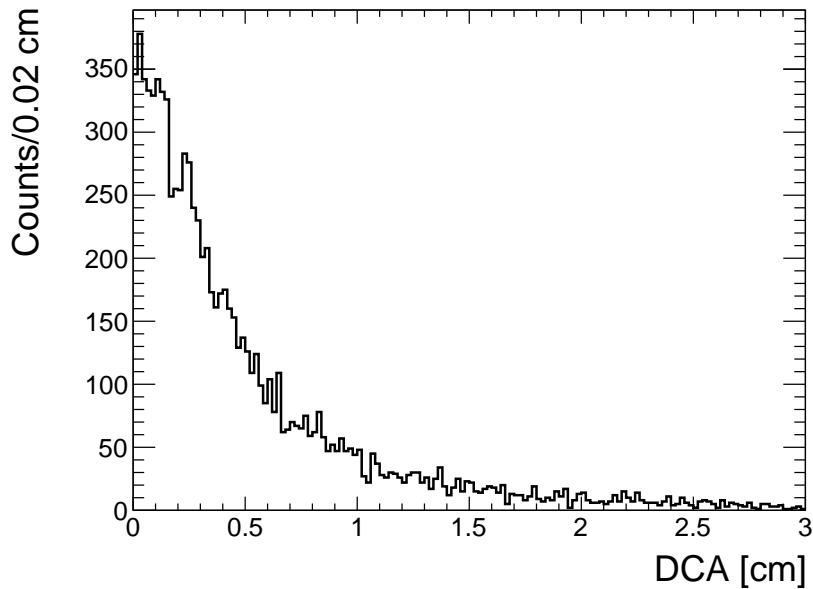
Figure 4.6: DCA distribution between the K^- beam track and the π^- track for the helium-4 dataset. The high-energy gamma-ray selection is already applied.
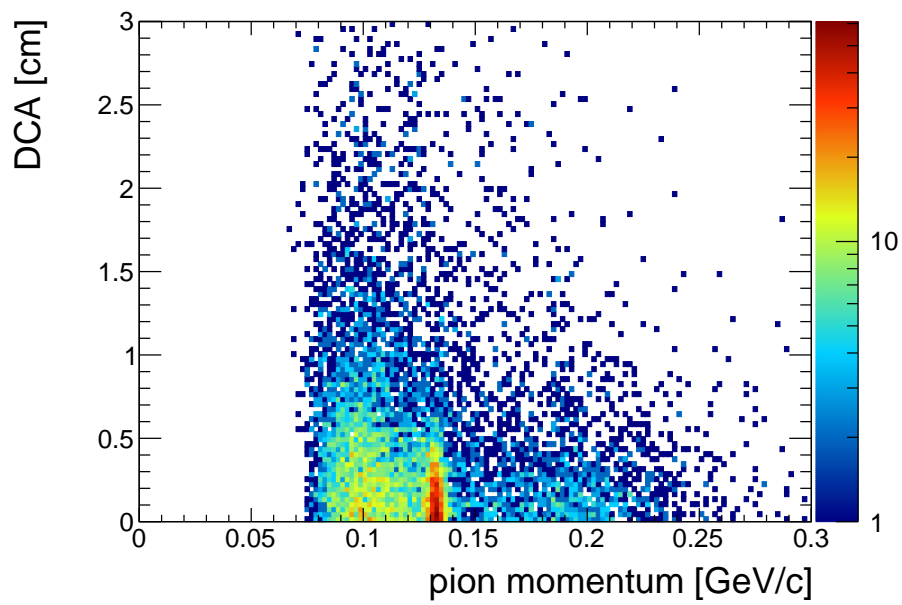
Figure 4.7: The correlation between the π^- momentum and DCA for the helium-4 dataset. A concentration of event at a momentum around 133 MeV/c and a small DCA is observed.
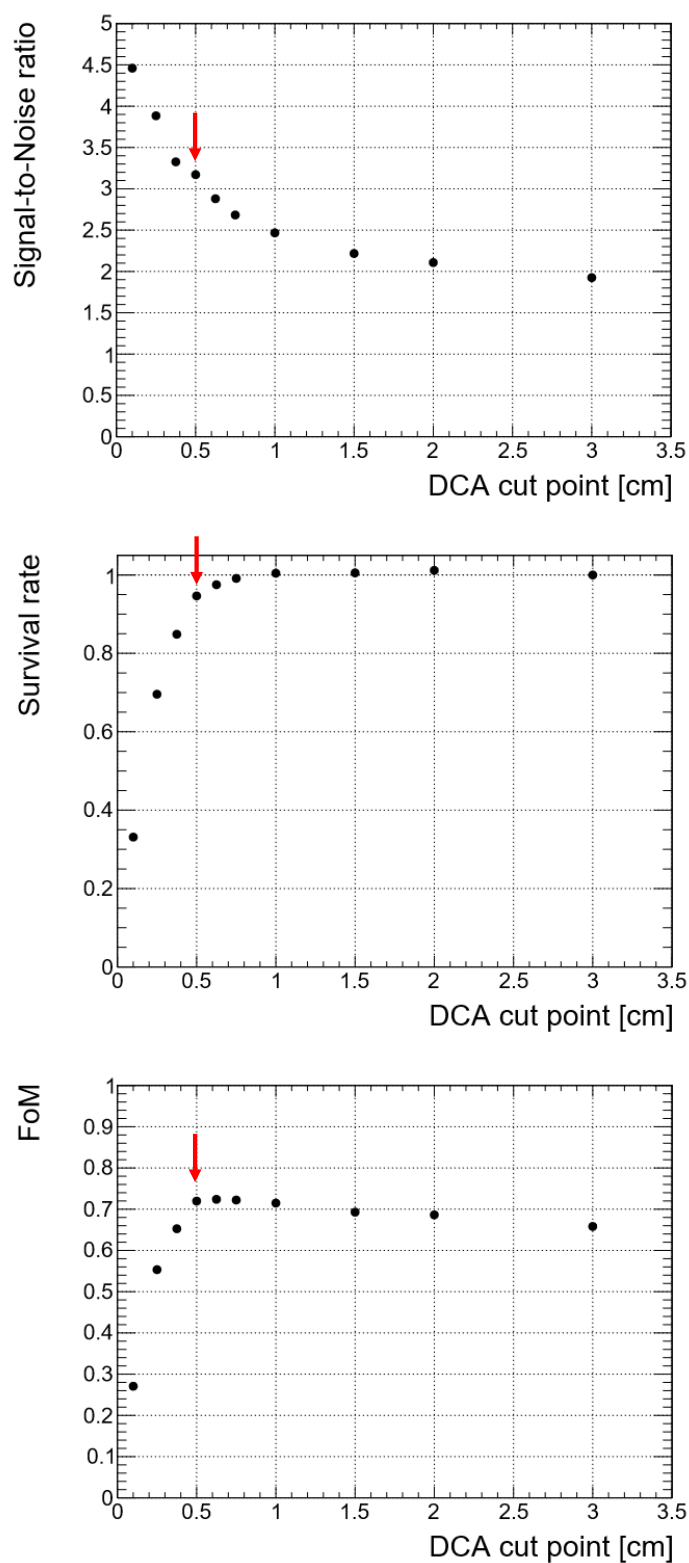
Figure 4.8: Signal-to-noise ratio (top), survival efficiency (middle) and figure of merit (bottom) against
the cut value of DCA for the helium-4 dataset.

Figure 4.8 (top) shows how the signal-to-noise ratio changes with the cut value of DCA. Figure 4.8 (middle) shows the survival efficiency of signal. Figure 4.8 (bottom) shows the figure of merit. The optimal cut is determined as 0.5 cm based on Fig. 4.8. Figure 4.9 shows the π^{-} momentum distribution before and after the event selection by DCA. The DCA cut improves the signal-to-noise ratio by a factor of roughly 1.6 with a signal efficiency of 94.7 %.
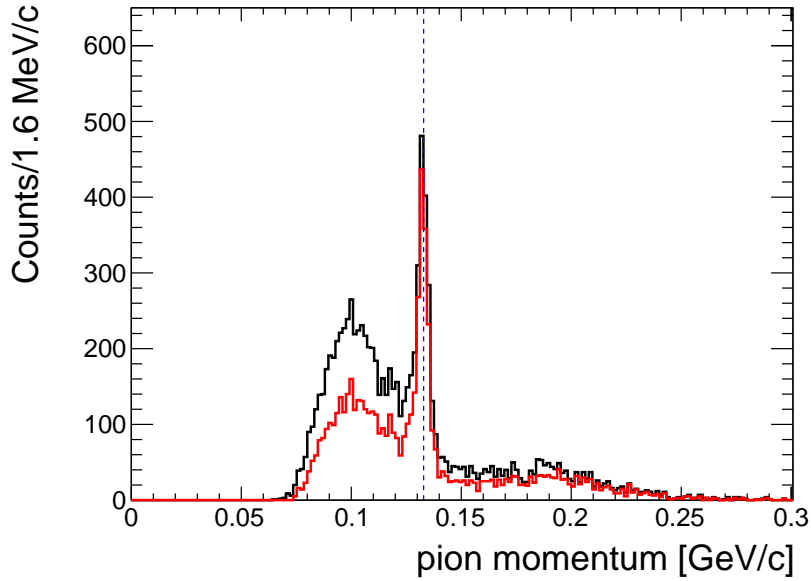

Figure 4.9: Change of the π^{-} momentum distribution by the DCA cut. The black line represents the distribution before the cut, while the red line represents the distribution after the cut.

4.2 Selection of $^{3}_{\Lambda}H$ event

Figure 4.10 shows two-dimentional PID plot for particles detected by CDS for helium-3 target with the physics trigger. As well as helium-4 target data, to avoid muon contamination, a threshold of 0.015 $(GeV/c^2)^2$ or higher with mass-square is chosen. Figure 4.11 shows the π^{-} momentum distribution for the helium-3 dataset with the physics trigger. The π^{-} momentum from the two-body decay of $^{3}_{\Lambda}H \rightarrow^{3} He + \pi^{-}$ is roughly 114 MeV/c by assuming $B_{\Lambda} = 0.13$ MeV. The signal of the two-body MWD of $^{3}_{\Lambda}H$ is visible as a small enhancement, but a precise extraction of signal yields is difficult due to the large amount of background. The same cuts as described in the previous section are applied for the analysis of the helium-4 dataset. An energy deposit $E_{\text{calo}} \geq 550$ MeV in the PbF$_2$ calorimeter and DCA ≤ 0.5 cm are required.
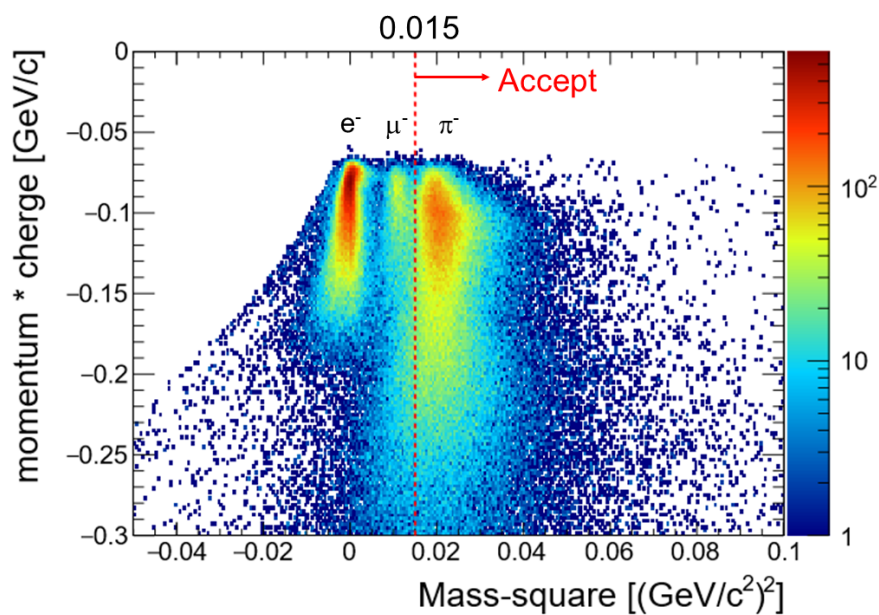
Figure 4.10: Two-dimentional PID plot for particles detected by CDS for helium-3 target with the physics trigger data. The red dotted line represents a 0.015 $(GeV/c^2)^2$ threshold for the π^- selection.

Figure 4.11: π^- momentum distribution for the helium-3 dataset with the physics trigger.

4.2.1 High-energy gamma-ray selection with PbF$_2$ calorimeter

Figure 4.12 shows the correlation between the π^- momentum and the energy deposit of the PbF$_2$ calorimeter. An energy deposit over 550 MeV with the PbF$_2$ calorimeter is selected for the helium-3 dataset. Figure 4.13 shows the π^- momentum distributions before and after the event selection by the PbF$_2$ calorimeter. The signal-to-noise ratio 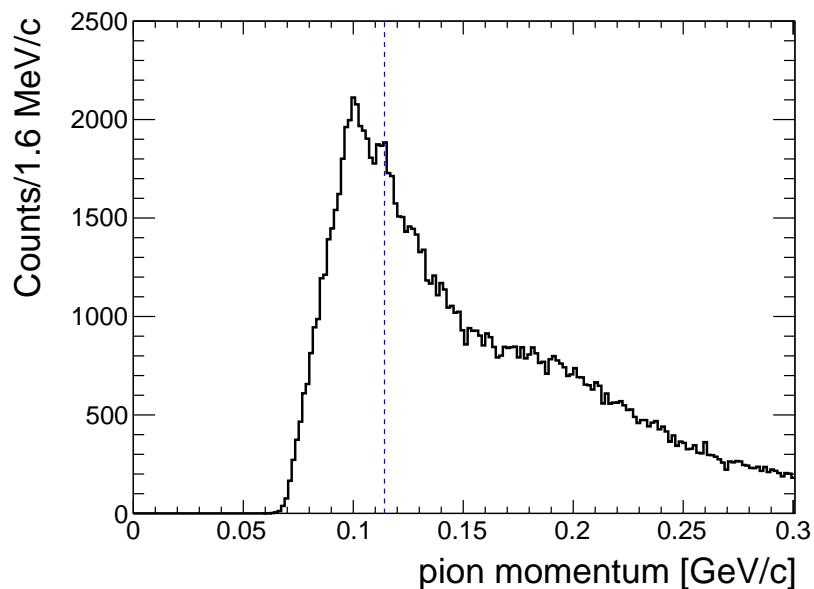is improved by a factor of roughly 2.7 with a signal efficiency of 48.8 %. The improvement of the S/N ratio is less significant comparing with that of the helium-4 dataset. The signal efficiency is nearly identical to that of the helium-4 target dataset.
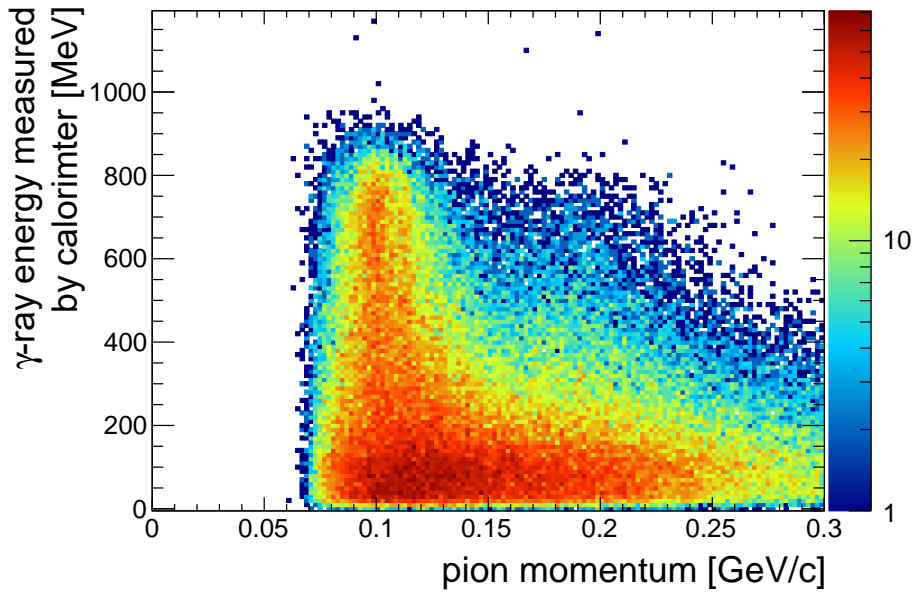
Figure 4.12: Correlation between the π^- momentum and the energy deposit of the PbF$_2$ calorimeter for the helium-3 dataset. The horizontal axis represents the π^- momentum, while the vertical axis displays the energy deposited in the PbF$_2$ calorimeter.

4.2.2 DCA selection between K^- beam and π^- tracks

Figure 4.14 shows the correlation between the π^- momentum and DCA. A DCA cut of less than 0.5 cm is applied after the high-energy gamma-ray selection. Figure 4.15 shows the π^- momentum distribution before and after the DCA selection for the helium-3 dataset. The DCA cut improves the signal-to-noise ratio by a factor of roughly 1.4 with a signal efficiency of 85.0 %. The rate of improvement in the signal-to-noise ratio is about the same as that for the helium-4 target dataset. However, the signal efficiency values differ from those of the helium-4 target dataset. It is important to note that the signal efficiency error from fitting error ranges from -20 % to $+15$ %, indicating no significant difference.

Figure 4.13: Change of the π^- momentum distribution before and after the PbF$_2$ energy selection for the helium-3 dataset. The black line represents the distribution before the selection, while the red line represents the distribution after the selection.
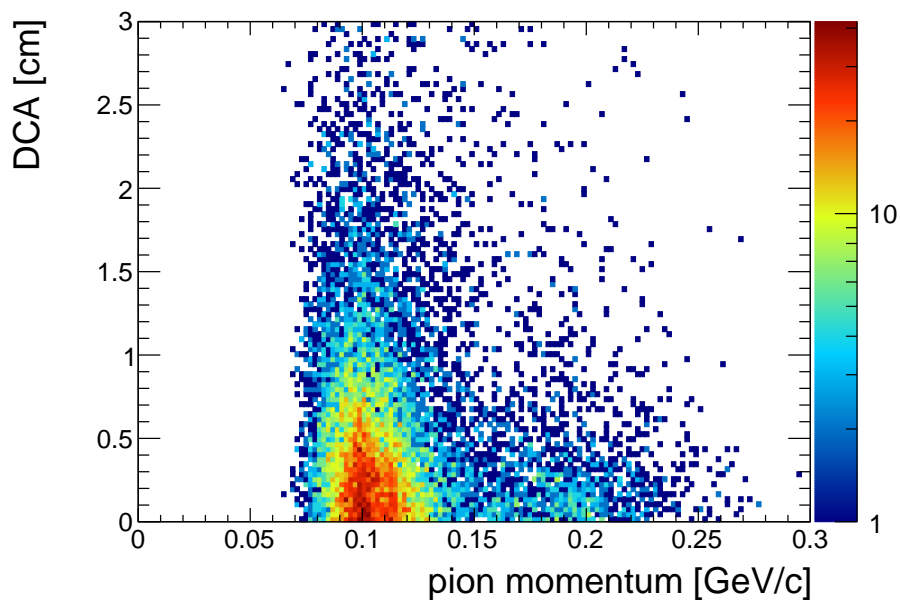
Figure 4.14: The correlation between the π^- momentum and DCA for the helium-3 dataset.

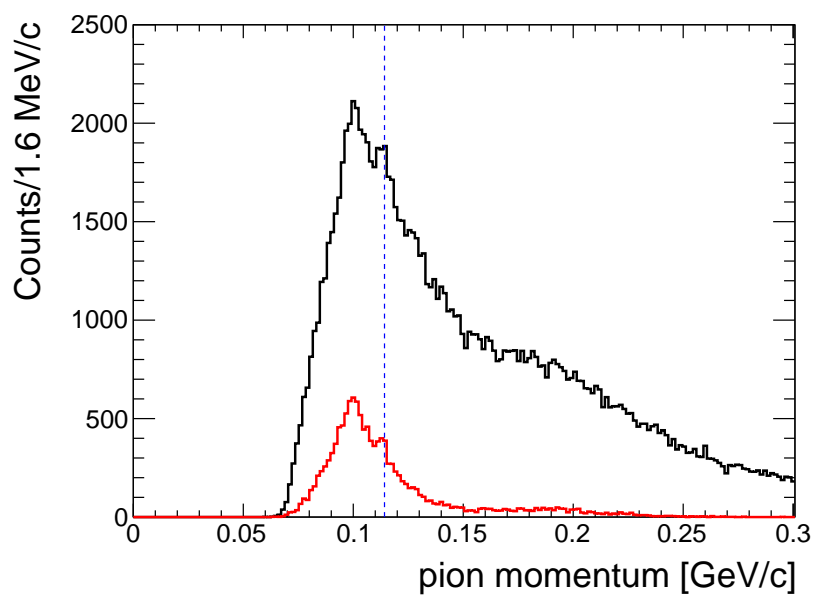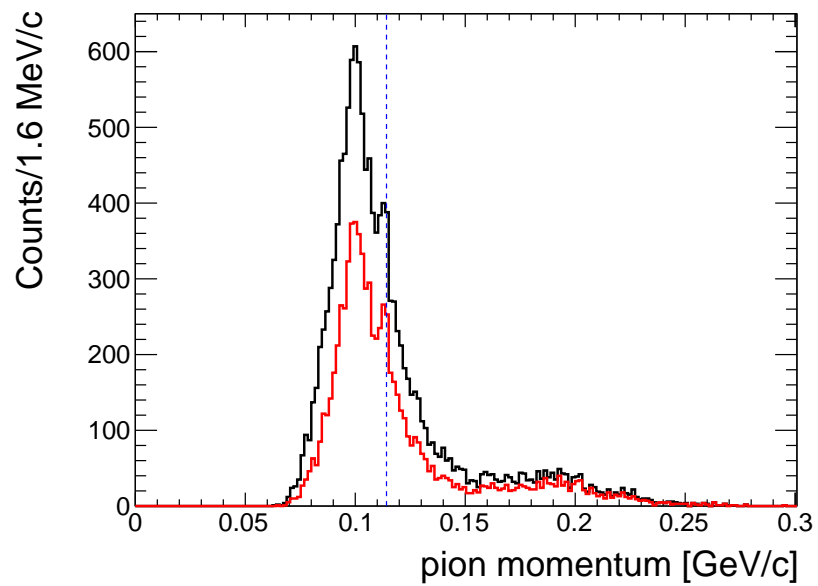**Figure 4.15:** Change of the π^{-} momentum distributions before and after the DCA cut for the helium-3 dataset. The black line represents the distribution before the cut, while the red line represents the distribution after the cut.

4.3 Final spectra of the π^- momentum distribution

Figure 4.16 show the π^- momentum spectra after the gamma-ray energy and the DCA cuts for the helium-4 (a) and the helium-3 datasets (b). From the spectra, the yields from the $^4_\Lambda$H and $^3_\Lambda$H two-body MWD are evaluated. Figure 4.17 shows the correlation between the π^- momentum and the π^- angle with respect to the K^- beam. For the in-flight hyperon decay in the quasi-free process, the momentum is angle dependent, while hypernucleus decay shows no angle dependence. The angular distribution will be helpful to understand background processes.
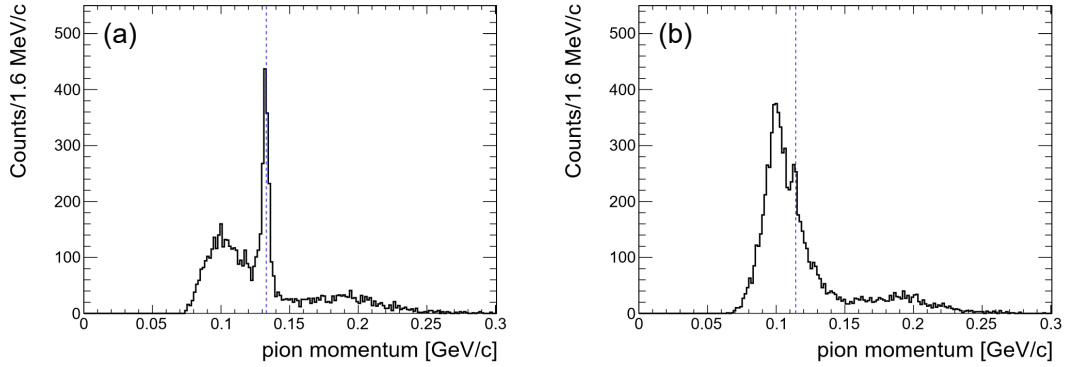
Figure 4.16: π^- momentum spectra after the gamma-ray energy and the DCA cuts for (a) the helium-4 and (b) the helium-3 datasets. The blue dashed line in each spectrum represents the π^- momentum of the two-body MWD of $^4_\Lambda$H and $^3_\Lambda$H, respectively.
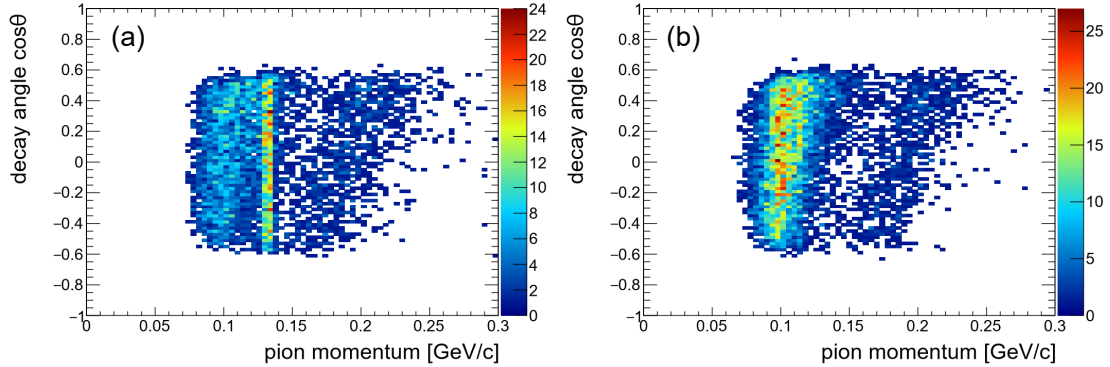
Figure 4.17: Correlation between the π^- momentum and π^- decay angle for (a) the helium-4 and (b) the helium-3 datasets. The horizontal axis represents the π^- momentum and the vertical axis represents the emission angle of π^-.

4.4   Estimation of background components by MC simulation

Although the signal-to-noise ratio is improved after event selection, background events still remain in the final spectra. After the high-energy gamma-ray selection with the PbF_2 calorimeter, most of the events come from decays of quasi-free hyperons produced via the (K^-, π^0) reactions. The distinction between hypernucleus production events and quasi-free hyperon production events cannot be made, since the calorimeter system does not fully reconstruct π^0, and the missing mass calculation of the $^{3,4}He(K^-, \pi^0)X$ reaction is not feasible. In addition, decay particles from the beam K^- can also contribute to the background. In this section, these background processes are investigated using a Monte-Carlo simulation, and an attempt is made to reproduce the π^- momentum distributions of the background processes. The distribution of the Fermi motion of the target particles was introduced into the Monte Carlo simulations. Helium-4 target is from Wiringa *et al.*[64] and Helium-3 target is from Jans *et al.*[65].

4.4.1   Quasi-free hyperon production

Most of the background hyperons are produced by the quasi-free (K^-, π^0) reaction, in which protons in helium are converted to Λ or Σ^0 and neutrons to Σ^-. Major hyperon decay processes with emission of a π^- are as follows,

$$\Lambda \to p + \pi^-,$$
$$\Sigma^0 \to \Lambda + \gamma, \ \Lambda \to p + \pi^-,$$
$$\Sigma^- \to n + \pi^-.$$

The Monte-Carlo simulation calculation for these quasi-free hyperon production processes was performed using the GEANT4 toolkit, and the same detector analysis procedure as applied to the experimental data was used.

Figure 4.18 shows the momentum distribution of π^- from the in-flight Λ, Σ^0, Σ^- decays. A small difference of widths of the distributions is seen between the helium-4 and helium-3 targets. This is due to the difference of Fermi motion of protons in the target nuclei. Figure 4.19 shows correlation between the π^- momentum and π^- decay angle from the in-flight Λ, Σ^0, Σ^- decays. The angle dependence of the momentum can be seen. Hyperons produced in the quasi-free process have high recoil momenta and decay before coming to rest in the target, so decay π^- momenta from the flying hyperons varies with angle due to Lorentz boost. Figure 4.20 shows the distribution of energy deposition in the PbF_2 calorimeter. The maximum value of energy that gamma-rays have in the process of producing Λ, Σ^0 and Σ^- is different because of the difference in energy needed to produce Λ, Σ^0 and Σ^-.
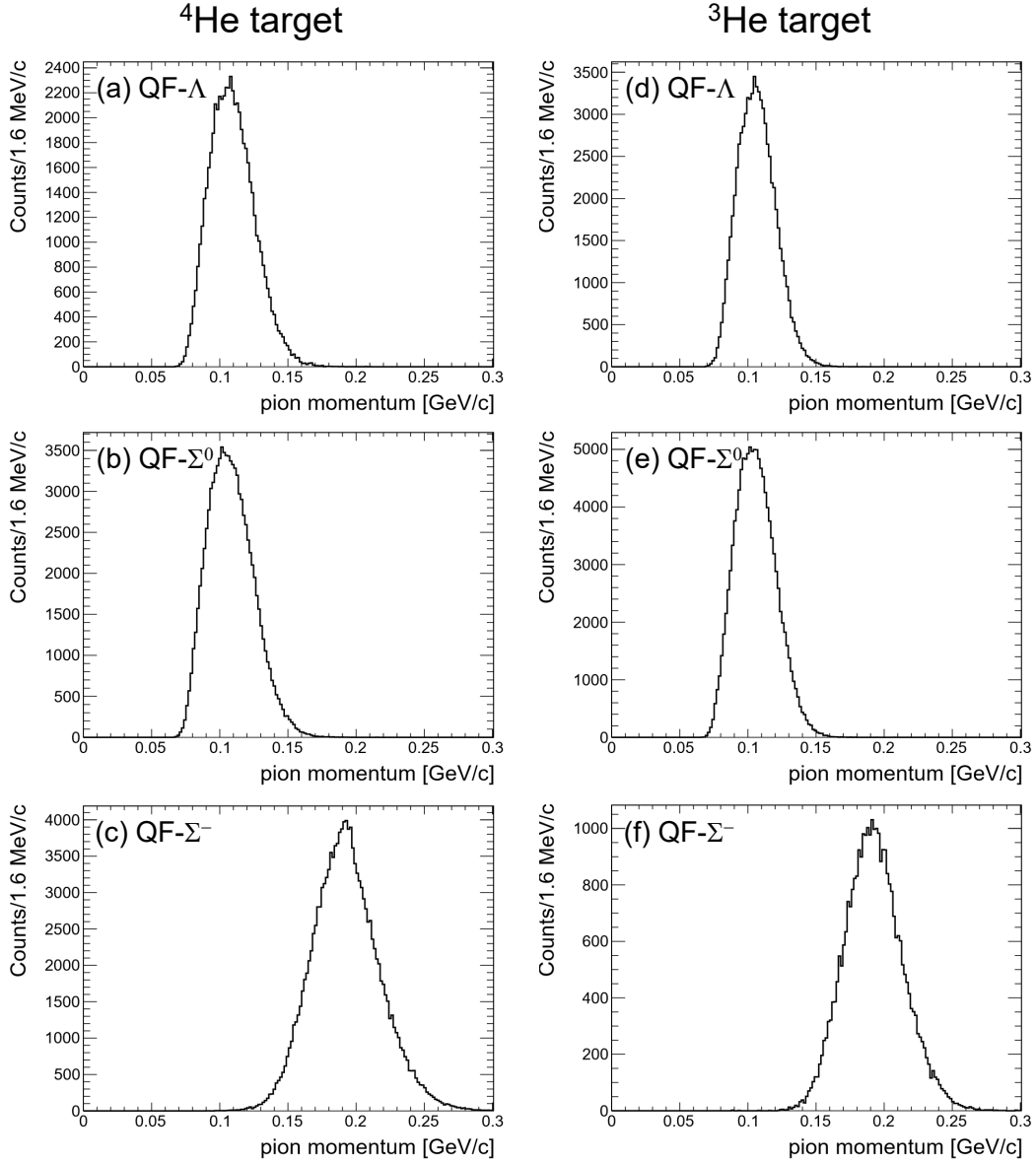
Figure 4.18: The π^- momentum distribution from decys of hyperons produced by the quasi-free pro-
duction reactions by a Monte-Carlo simulation. (a)Λ, (b)Σ^0, (c)Σ^- hyperon produced in
the quasi-free process with the helium-4 target. (d)Λ, (e)Σ^0, (f)Σ^- hyperon produced in
the quasi-free process with the helium-3 target.
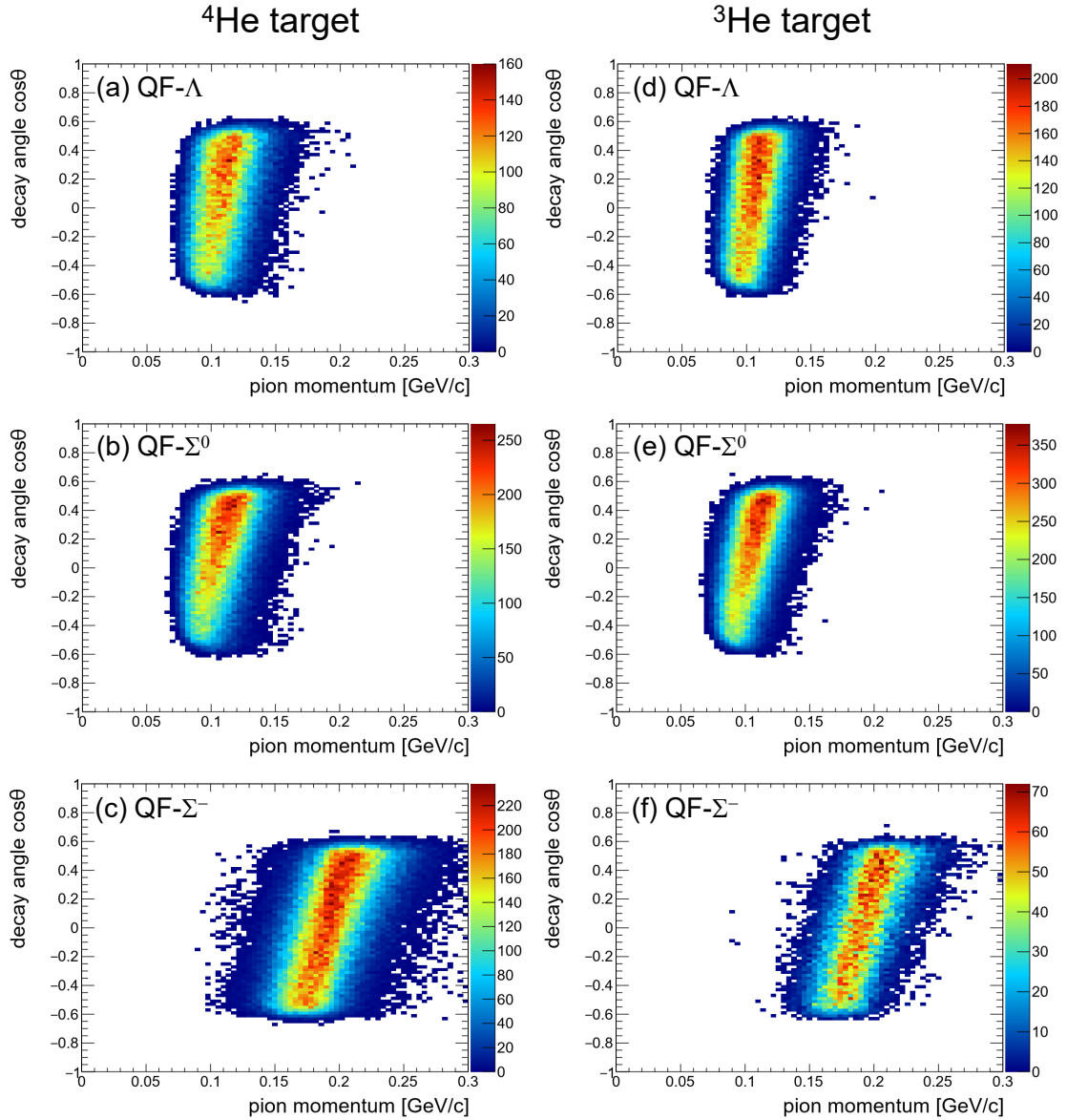
Figure 4.19: Simulated correlation between the π^- momentum and the π^- emission angle with respect to the K^- beam by a Monte-Carlo simulation. The hyperon elements shown here are the same as in Fig. 4.18.
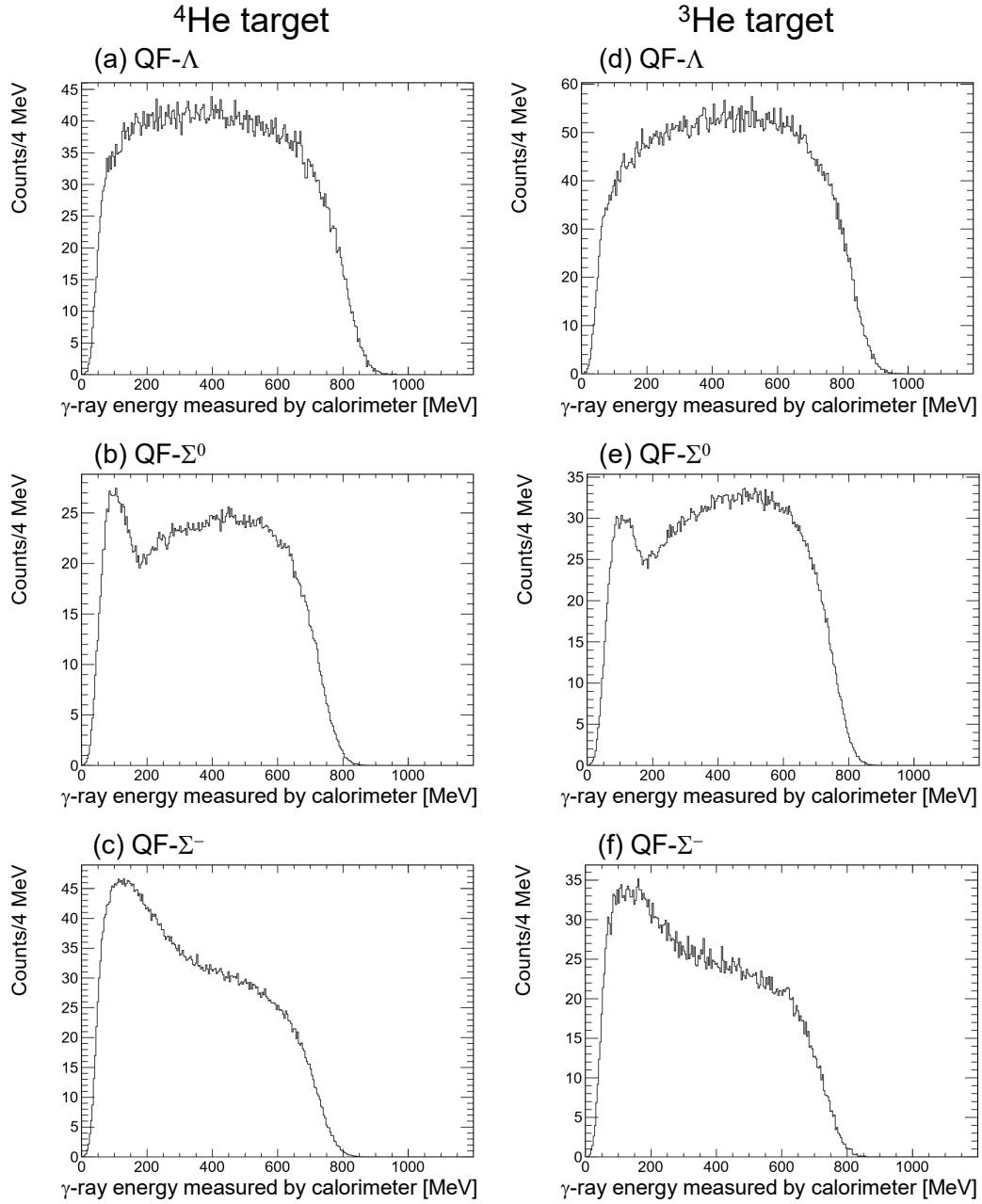
Figure 4.20: Simulated gamma-ray energy distribution from the quasi-free production reactions by a Monte-Carlo simulation. The hyperon elements shown here are the same as in Fig. 4.18 and Fig. 4.19.

4.4.2 In-flight Kaon decay

The target was irradiated with K^- in the Monte-Carlo sumilation calculation. Hadronic reactions are turned off to simulate only the kaon decay processes. Major decay modes of K^- emitting π^0 are as follows.

$$K^- \rightarrow \pi^0 + \pi^- \ (20.66\%),$$
$$K^- \rightarrow \pi^0 + \pi^0 + \pi^- \ (1.761\%),$$
$$K^- \rightarrow \pi^0 + \mu^- + \nu_\mu \ (3.353\%)$$

Figure 4.21 shows π^- momentum distribution from $K^- \rightarrow \pi^0 + \pi^-$ decay of the K^- beam after the gamma-ray energy and the DCA cuts. Figure 4.22 shows gamma-ray energy distribution from $K^- \rightarrow \pi^0 + \pi^-$ decay of the K^- beam.
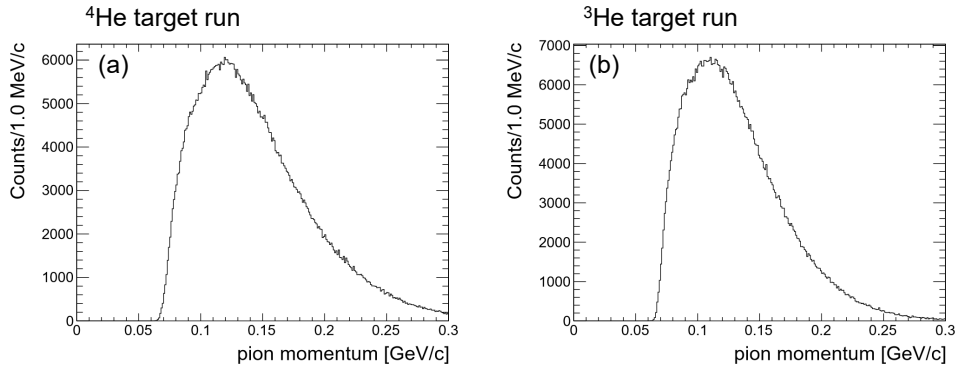
Figure 4.21: Simulated π^- momentum distribution from decays of the K^- beam. This distribution considers only $K^- \rightarrow \pi^0 + \pi^-$. (a) K^- beam irradiated to helium-4 target. (b) K^- beam irradiated to helium-3 target.
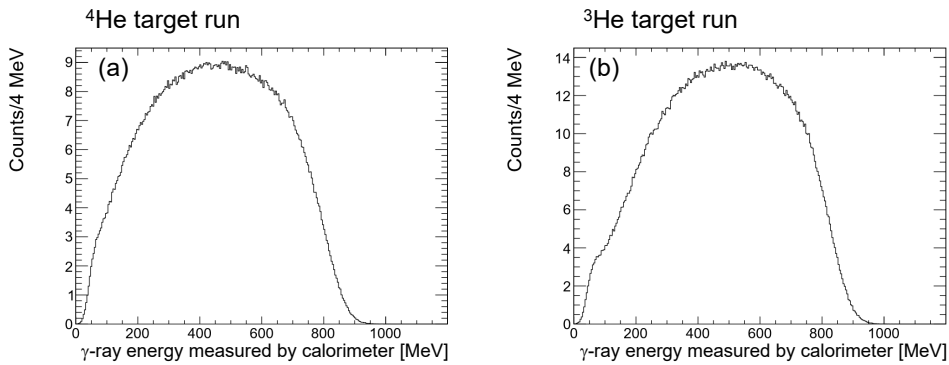
Figure 4.22: Simulated gamma-ray energy distribution from decays of the K^- beam. This distribution considers only $K^- \rightarrow \pi^0 + \pi^-$. (a) K^- beam irradiated to helium-4 target. (b) K^- beam irradiated to helium-3 target.

A large energy deposit is present in the PbF$_2$ calorimeter. It is evident that in-flight decay π^- from K^- beam may also serve as background. These distributions are used when fitting experimental data. However, estimating the number of such events from the π^- distribution of production data is difficult due to the small number of occurrences and the uncharacteristic shape. Therefore, the amount of background from the K^- decay event is estimated indirectly from the number of μ^- coming from the $K^- \to \pi^0 + \mu^- + \nu_\mu$ decay, as observed by CDS. In particle identification by CDS, μ^- can be seen as shown in Fig. 4.1. The number of μ^- is 513 events with mass square from 0.008 (GeV/c^2)^2 to 0.014 (GeV/c^2)^2 and momenta from 0 GeV/c to 0.125 GeV/c. μ^- momentum distribution from $K^- \to \pi^0 + \mu^- + \nu_\mu$ decay is simulated in the same way. First, the ratio of the number of μ^- in the data is taken to the number of μ^- in the simulation. This ratio and the number of π^- from simulations, along with the decay branching ratio, are analyzed to estimate the number of π^- resulting from in-flight K^- decay in the data. The ratio N_{μ^-}/N_{π^-} obtained from the simulation is 0.91. The number of decay π^- from the kaon beam is 467 events. Similarly, the number of muons in the helium-3 dataset is 899 events and the number of decay π^- from the kaon beam is 819 events. The number of μ^- in the helium-3 and helium-4 datasets is 1.7. This is consistent with the ratio of the number of kaon beam used in the analysis. Consequently, it is estimated that 5 % of the total number of events in the final spectrum in the helium-4 dataset and 10 % in the helium-3 dataset are attributable to the K^- in-flight decay. The contribution of the number of π^- from $K^- \to \pi^0 + \pi^0 + \pi^-$ decay is small and is negligible.

4.5 Analysis for production cross sections of hypernuclei

4.5.1 Fitting procedure

The signal and background fittings are performed on the final π^- momentum spectra to estimate the number of the decay π^- from the hypenuclei. The fittings are performed for the helium-4 dataset at first. The components of the background processes are the quasi-free Λ, Σ^0, Σ^- productions and the K^- decays. Figure 4.23 shows the fitting results.
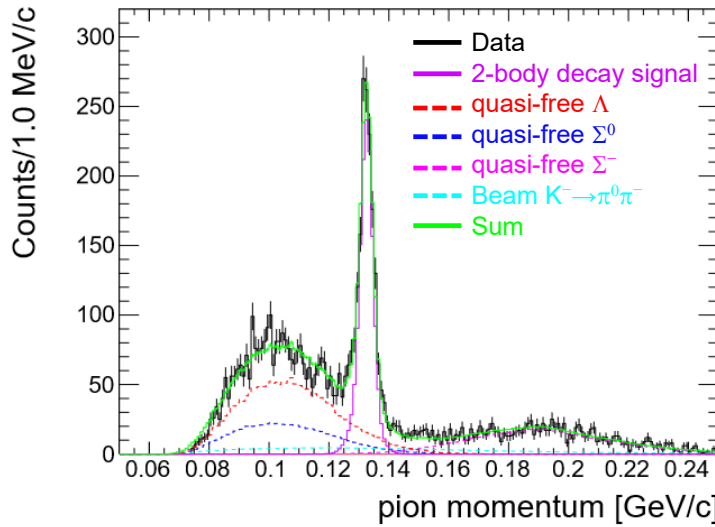

Figure 4.23: The π^- momentum spectra with fitting components for the helium-4 dataset. The brack line represents the spectra of the experimental data. The purple line represents the peak of the two-body MWD signal from $^4_\Lambda$H. The red dashed line represents the spectra from the in-flight Λ decay. The blue dashed line represents the spectra from the in-flight Σ^0 decay. The magenta dashed line represents the spectra from the in-flight Σ^- decay. The cyan dashed line represents the spectra from the beam K^- decay. The green line represents the summed spectra.

The π^- from the Λ and Σ^0 decay is the component with lower momentum from 0.07 GeV/c to 0.15 GeV/c. The ratio between Λ and Σ^0 productions is taken as the ratio of the production cross sections of the elementary processes . The production cross sections of the elementary processes are 3.4 mb for Λ [66] and 0.92 mb for Σ^0 [67] at the beam momentum of 1 GeV/c. The π^- momentum spectra from Λ and Σ^0 decays are obtained taking into account differences in angular distribution of the production reaction. π^- from the Σ^- decay is the component with higher momentum from 0.15 GeV/c to 0.25 GeV/c. The number of π^- due to the K^- decay is estimated as mentioned in Sec. 4.4.2. The peak at a momentum around 133 MeV/c is fit by a Gaussian function. The parameters for the fitting are the height of the π^- distibution from the Λ and Σ^0 decays, the height of the π^- distribution from the Σ^- decay and the parameters of the Gaussian function of the signal peak at a momentum around 133 MeV/c.

Figure 4.24 shows the spectra after subtracting the background. The number of π^- from the two-body MWD of $^4_\Lambda$H is estimated to be 1404 ± 45 from a histogram after background subtraction.
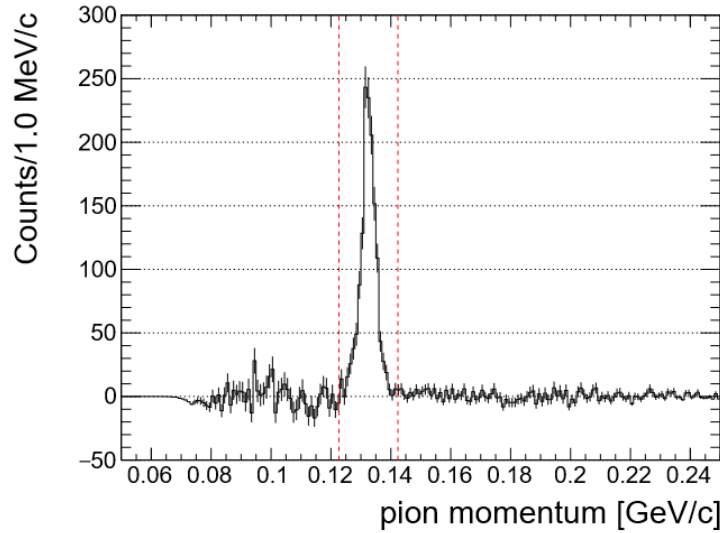

Figure 4.24: The π^- momentum spectra after the background subtraction for the helium-4 dataset. The remaining peak is the signal from the two-body decay of $^4_\Lambda$H.
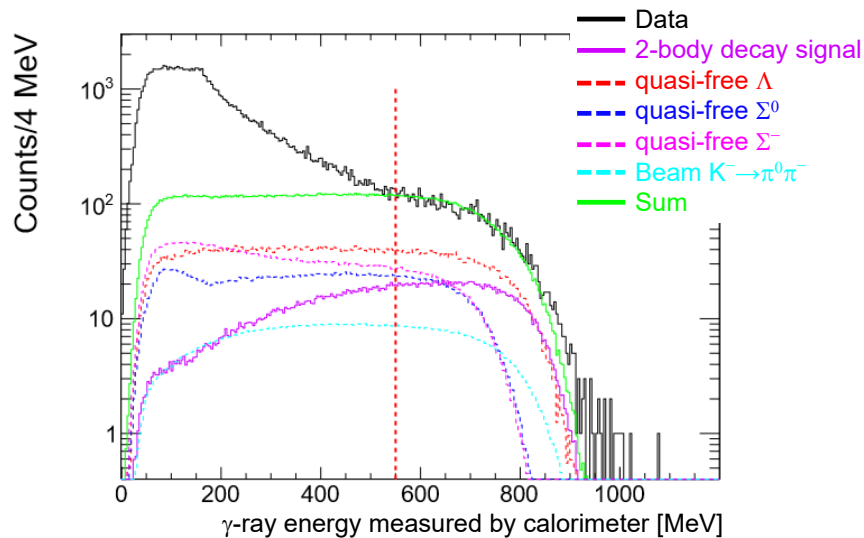

Figure 4.25: The gamma-ray energy distribution with signal and background components for the helium-4 dataset. The elements shown here are the same as in Fig. 4.23.

Figure 4.25 shows the simulated energy distribution of each component superimposed on the energy spectrum of the PbF$_2$ calorimeter with the final cut for the helium-4 dataset. The vertical scale factor of each energy distribution is determined by the factor used when fitting the π^- momentum distribution. The experimental energy spectrum of the PbF$_2$ calorimeter above 550 MeV can be well explained by the signal, the quasi-free hyperon, and the in-flight Kaon decay components. On the other hand, the inability to reproduce values below 500 MeV is mainly due to the contribution of processes that are not accounted for in the MC.

The fittings are performed also for the helium-3 dataset. Figure 4.26 shows the fitting results. As in $^4_\Lambda$H case, the background components are the decay from the quasi-free Λ, Σ^0, Σ^- production processes and the K^- decays. However, an unexplained distribution exists at around 0.1 GeV/c for components similar to $^4_\Lambda$H.
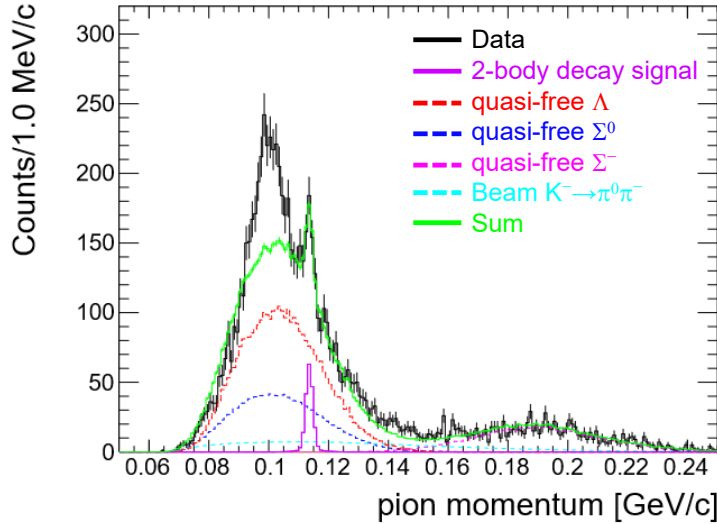
Figure 4.26: The π^- momentum spectra with fitting components for the helium-3 dataset. The brack line represents the spectra of the data. The purple line represents the peak from the two-body decay MWD signal of $^3_\Lambda$H. The red dashed line represents the spectra from the in-flight Λ decay. The blue dashed line represents the spectra from the in-flight Σ^0 decay. The magenta dashed line represents the spectra from the in-flight Σ^- decay. The cyan dashed line represents the spectra of the beam K^- decay. The green line represents the summed spectra.

Therefore, a component that can be explained at around 0.1 GeV/c will be introduced. To begin, a $^3_\Lambda$H three-body decay is introduced. For the $^3_\Lambda$H three-body decays, the π^- momentum distribution calculated by Kamada *et al.*[34] is used. The ratio of the number of signals for the two-body MWD events to the number of the three-body decay events was fixed to the ratio from previous experimental studies. The ratio of MWD into the π^- two-body to all π^- MWD is $0.357^{+0.028}_{-0.027}$[68] from previous studies. Figure 4.27 shows the fitting results with the three-body MWD component added. This alone cannot explain the structure around 100 MeV/c with only

three-body MWD signals.

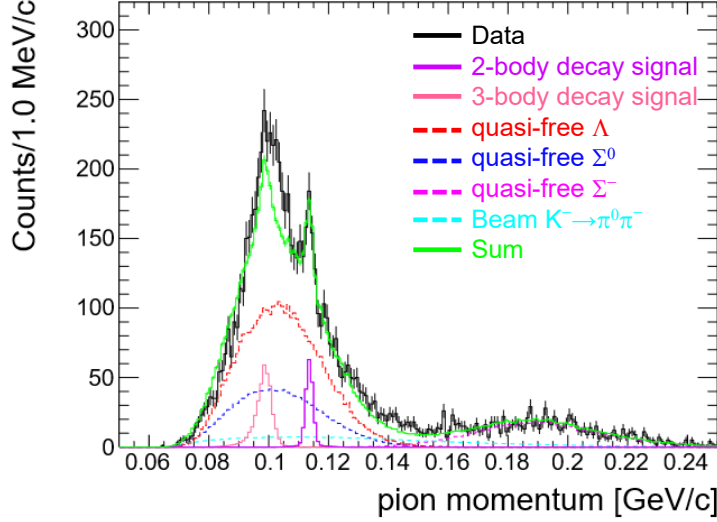**Figure 4.27:** The π^- momentum spectra with fitting components with the three-body MWD component added for the helium-3 dataset. The brack line represents the spectra of the data. The elements shown here are the same as in Fig. 4.26 and add the peak from the three-body MWD signal of $^3_\Lambda$H with the pink line.

In addition, A Gaussian centered at 100 MeV/c is added. This component appears to originate from Λ, as it has a momentum of around 100 MeV/c. Such a structure would be expected with a large number of low momentum Λ. This component is considered to be a Λ that did not form a bound state. This component seeps out to $B_\Lambda < 0$ when considering the distribution of Λ binding energy. One should notice that only helium-3 data has such contribution because of the concentration of such a Λ component around $B_\Lambda = 0$ due to small binding energy of $^3_\Lambda$H. Figure 4.28 shows the fitting results with the three-body MWD component and low momentum Λ component added. Figure 4.29 shows the spectra after subtracting the background. The number of π^- from the decay of $^3_\Lambda$H is estimated to be 225 ± 39 from a histogram after background subtraction.

Figure 4.30 shows the gamma-ray energy distribution of each component superimposed on the PbF$_2$ calorimeter energy distribution in the final cut for the helium-3 dataset. As with the helium-4 target, the vertical scale factor of each energy distribution is determined by the factor used when fitting the π^- momentum distribution. The gamma-ray energy spectrum above 550 MeV can be well explained by the $^3_\Lambda$H signal, the in-flight hyperon decay, and the in-flight Kaon decay components.

The fitting procedure in the π^- momentum distribution of $^4_\Lambda$H is revisited. In the π^- momentum distribution of $^3_\Lambda$H, a component of the three-body MWD of $^3_\Lambda$H and the low-momentum Λ hyperon was observed. The same components are expected to be present in the π^- momentum distribution of $^4_\Lambda$H. Therefore, the components of the three-body MWD of $^4_\Lambda$H and the low-

Figure 4.28: The π^- momentum spectra with fitting components with the three-body MWD component and low momentum Λ component added for the helium-3 dataset. The elements shown here are the same as in Fig. 4.27. The two line are added the spectra from the in-flight Λ decay and low Λ decay with the red dashed line and the spectra from the in-flight Λ decay with the red dotted.
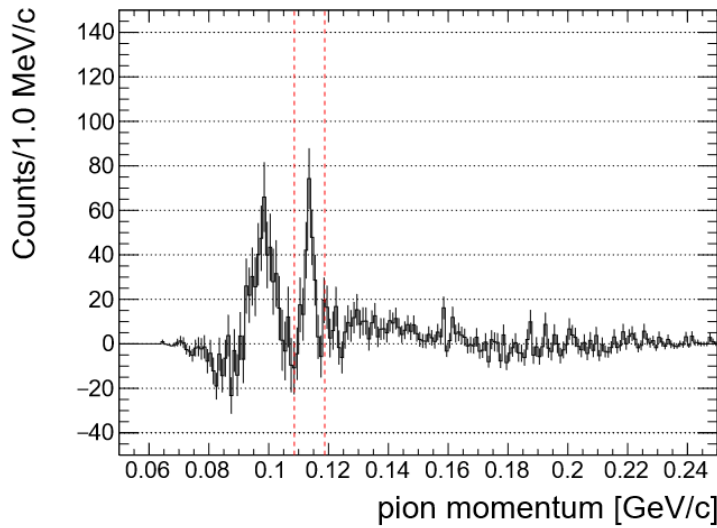
Figure 4.29: The π^- momentum spectra after the background subtraction for the helium-3 dataset. The peak at around 114 MeV/c is the events from the two-body MWD of $^3_\Lambda$H. The peak at around 100 MeV/c is the events from the three-body MWD of $^3_\Lambda$H.
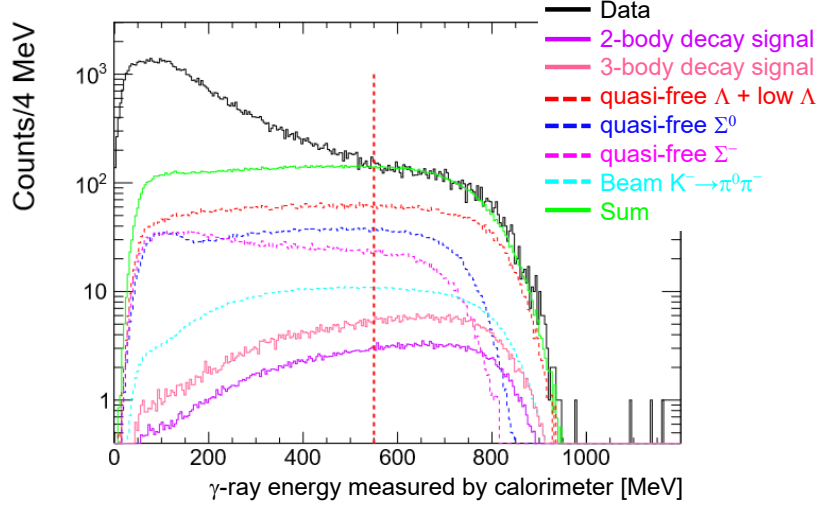
Figure 4.30: The gamma-ray energy distribution with signal and background components for the helium-3 dataset. The elements shown here are the same as in Fig. 4.28.

momentum Λ hyperon are introduced. For the distribution of three-body MWD of $^4_\Lambda$H, the π^- momentum distribution calculated by Motoba *et al.*[69] is used. The π^- momentum distribution of three-body MWD of $^4_\Lambda$H is only for the decay mode to $^4_\Lambda$H $\to t + p + \pi^-$. Figure 4.31 shows the fitting results with the three-body MWD component and the low-momentum Λ component added. The ratio of MWD into the π^- two-body to all π^- MWD is 0.69 $\pm$0.17[68] from previous studies. The distribution of three-body decays was introduced, and it was found that the shape fits only 1/3 of the expected number, which is within the margin of error. It is important to note that the distribution being considered is only the decay mode of $^4_\Lambda$H $\to t + p + \pi^-$, and there are events outside the acceptance. The $^3_\Lambda$H distribution had a high number of low-momentum lambda hyperons, whereas in the $^4_\Lambda$H distribution, they are fewer and more widely distributed. This difference may be attributed to the fact that the binding energy of $^4_\Lambda$H is B_Λ = 2.169 $\pm$ 0.042 MeV[68], which is more deeply bound than that of $^3_\Lambda$H, making it difficult to produce low-momentum Λ hyperons. In this analysis, the systematic error includes the number of Λ hyperons with low momentum. Figure 4.32 shows the spectra after subtracting the background. The number of π^- from the decay of $^3_\Lambda$H is estimated to be 1465 $\pm$ 45 from a histogram after background subtraction.

Figure 4.33 shows the revisit gamma-ray energy distribution of each component superimposed on the PbF$_2$ calorimeter energy distribution in the final cut for the helium-4 dataset. It is evident that the distribution above 550 MeV can be accounted for even with the inclusion of additional components.
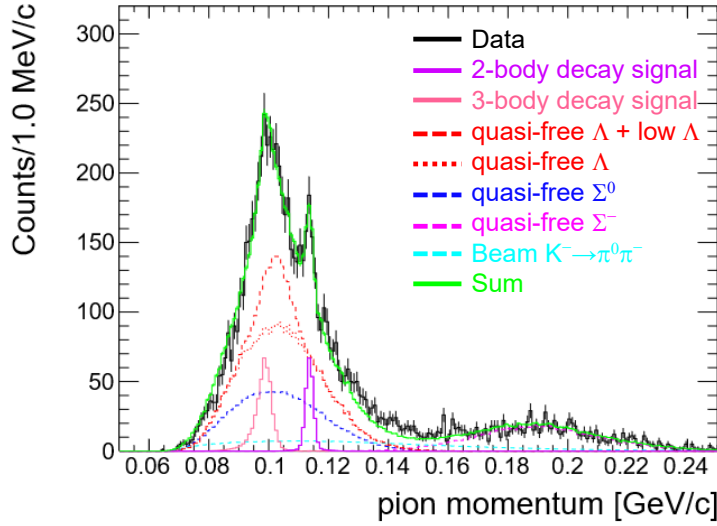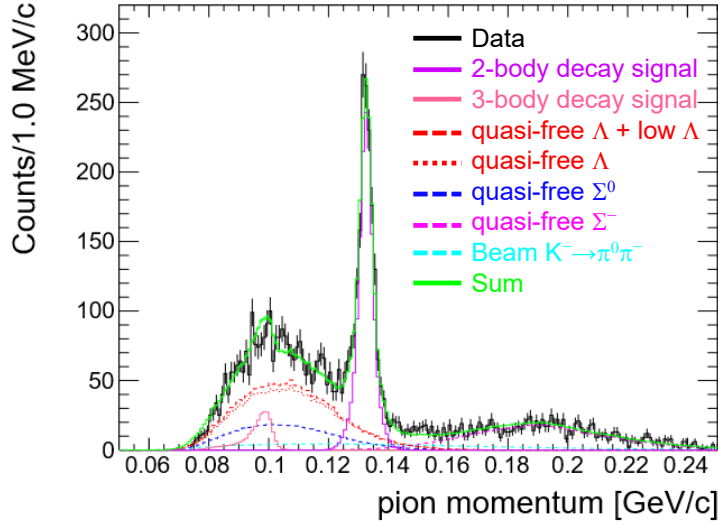
Figure 4.31: The π^- momentum spectra with fitting components with the three-body MWD component and low momentum Λ component added for the helium-4 dataset. The brack line represents the spectra of the data. The purple line represents the peak from the two-body MWD signal of $^4_\Lambda$H. The pink line represents the peak from the three-body MWD signal of $^4_\Lambda$H. The red dashed line represents the spectra from the in-flight Λ decay and low Λ decay. The red dotted line represents the spectra from the in-flight Λ decay. The blue dashed line represents the spectra from the in-flight Σ^0 decay. The magenta dashed line represents the spectra from the in-flight Σ^- decay. The cyan dashed line represents the spectra of the beam K^- decay. The green line represents the summed spectra.

Uncertainty of number of signal on fitting process

When performing the fitting, it is important to estimate the number of signals. In the helium-4 target dataset, the fitting results for various binning, different ratios of the Λ and Σ^0 components of the background and the presence of a low momentum Λ component were analyzed. This analysis uncertainty of the number of signals for 2-body decay in $^4_\Lambda$H is $^{+5}_{-61}$.

In the helium-3 target dataset, in addition to the fit results when binning was changed and when the ratio of the background Λ and Σ^0 components was changed, the ratio value that determines the number of 3-body decays was changed by 1σ and the presence of a low momentum Λ component was considered. This analysis uncertainty of the number of signals for 2-body decay in $^3_\Lambda$H is $^{+17}_{-25}$.
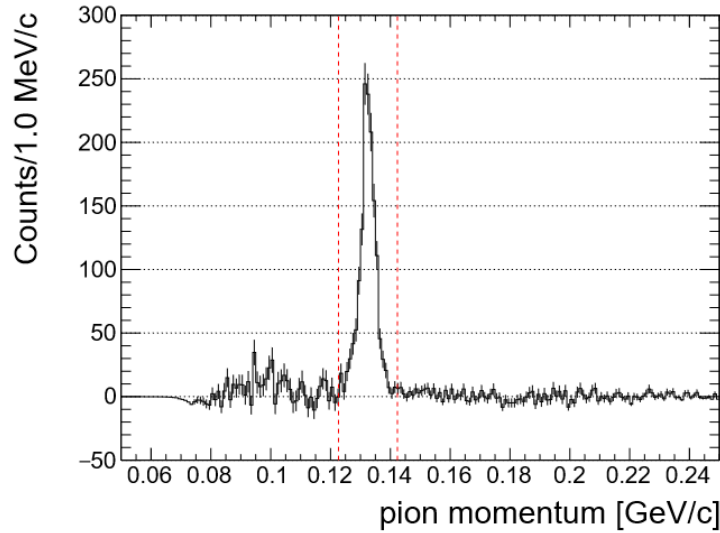
Figure 4.32: The π^- momentum spectra after the background subtraction for the helium-4 dataset. The peak at around 133 MeV/c is the events from the two-body MWD of $^4_\Lambda$H. The region less than 100 MeV/c is the events from the three-body MWD of $^4_\Lambda$H.
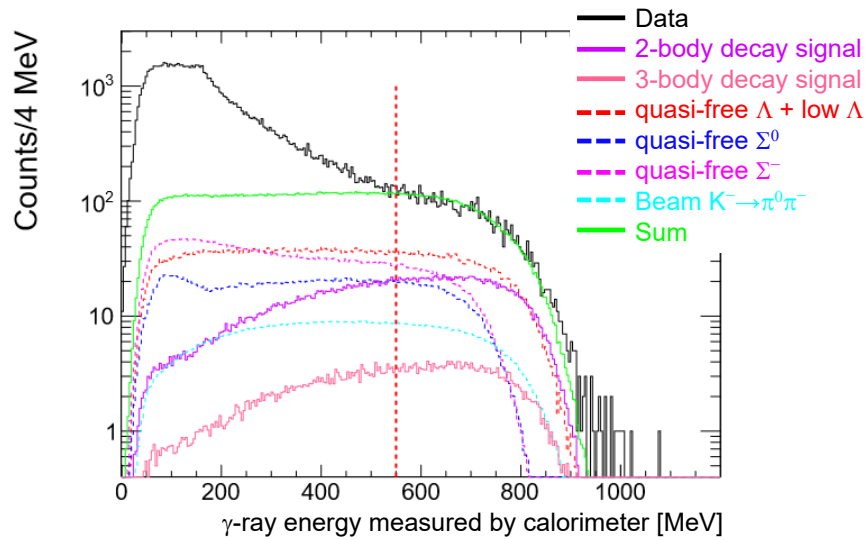

Figure 4.33: The gamma-ray energy distribution with signal and background components for the helium-3 dataset. The elements shown here are the same as in Fig. 4.31.

4.5.2 Acceptances and analysis efficiencies

Acceptance of CDS and the PbF$_2$ calorimeter and efficiencies were estimated by a Monte-Carlo simulation calculation based on GEANT4 package. A realistic CDS system and PbF$_2$ calorimeter setup were reproduced in the simulation. The same analysis procedure as those for the experimental data analysis were applied to the simulation data. The parameters required to produce $^{3,4}_{\Lambda}$H in the (K^-, π^0) reaction are the angular distribution of π^0 at the reaction vertex and the momentum of the incident K^-. Since the angular distribution of the production of the hypernuclei $^3_{\Lambda}$H and $^4_{\Lambda}$H by the (K^-, π^0) reaction was not measured in this experiment, theoretical calculation by Harada *et al.*[44] was used. Figure 4.34 shows the angular distributions of π^0 from the hypernuclei production reactions in the simulation calculation. π^0 is generated with the scattering angle from $0°$ to $20°$ on the hypernuclei production reactions in the simulation calculation.
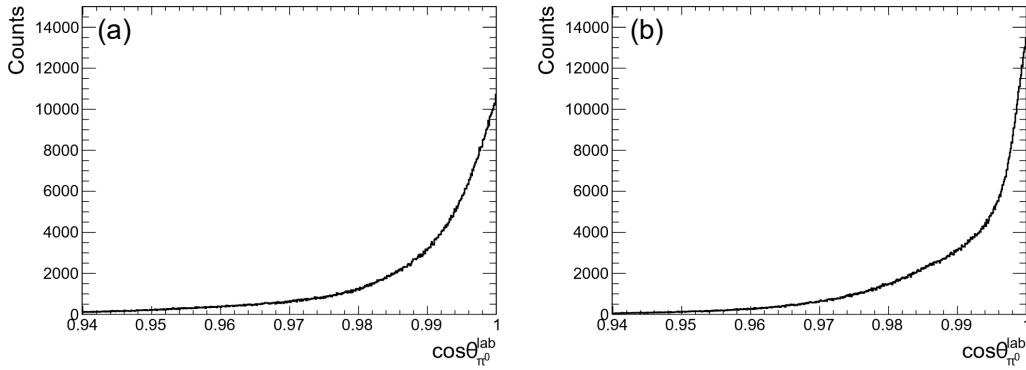
Figure 4.34: Calculated angular distributions for the $^4_{\Lambda}$H and $^3_{\Lambda}$H production via the ^{4}He(K^-, π^0) reactions at $p_{K^-} = 1.0$ GeV/c. (a) This is the distribution of angles at which π^0 is emitted when $^4_{\Lambda}$H is produced. (b) This is the distribution of angles at which π^0 is emitted when $^3_{\Lambda}$H is produced. These plots were output in the simulation calculation with input of theoretical calculations by Harada *et al*[44].

π^0 acceptance of geometry and uncertainty of gamma-ray selection efficiency by PbF$_2$ calorimeter

The acceptance of π^0, the parent particle of gamma rays measured by the PbF2 calorimeter, were estimated for the generated events in the simulation calculation. Acceptance of the PbF$_2$ calorimeter is defined as the fraction of events that can be detected. Figure 4.35 shows the acceptance when at least one gamma-ray enters the PbF$_2$ calorimeter. The ratio of the number of events in which gamma-rays are detected by the PbF$_2$ calorimeter and all generated events are 31.3 ± 0.2 % for the $^4_{\Lambda}$H and 31.9 ± 0.2 % for the $^3_{\Lambda}$H. Figure 4.36 shows the fraction of events in which the PbF$_2$ energy deposit is larger than 550 MeV within events that can be detected every angle. Figure 4.37 shows the fraction of events in which the PbF$_2$ energy deposit is larger than 550 MeV within events that can be detected PbF$_2$ calorimeter. In this experiment,

the energy calibration of the calorimeter was performed using 1 GeV/c electrons mixed in the meson beam. The beam momentum bite is roughly 3 %, the energy resolution is measured as 5 %. As there is only one calibration point, ambiguity in determining the calorimeter energy exists. Uncertainty of the gamma-ray selection efficiencies of the PbF$_2$ calorimeter are 50.1 $^{+5.9}_{-6.2}$ % for $^4_\Lambda$H and 51.4 $^{+6.0}_{-6.3}$ % for $^3_\Lambda$H.
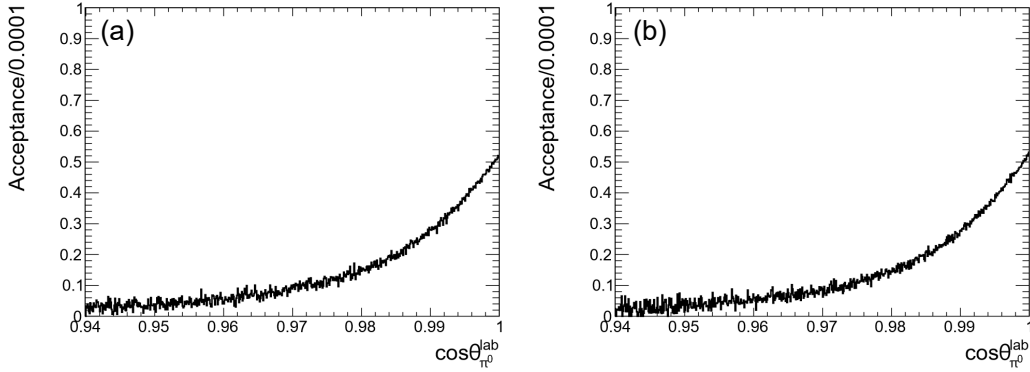
Figure 4.35: Geometrical acceptance of the PbF$_2$ calorimeter. Acceptance by PbF$_2$ calorimeter is the fraction of events that can be detected every angle. (a) The acceptance of π^0 is shown when $^4_\Lambda$H is generated. (b) The acceptance of π^0 is shown when $^3_\Lambda$H is generated.
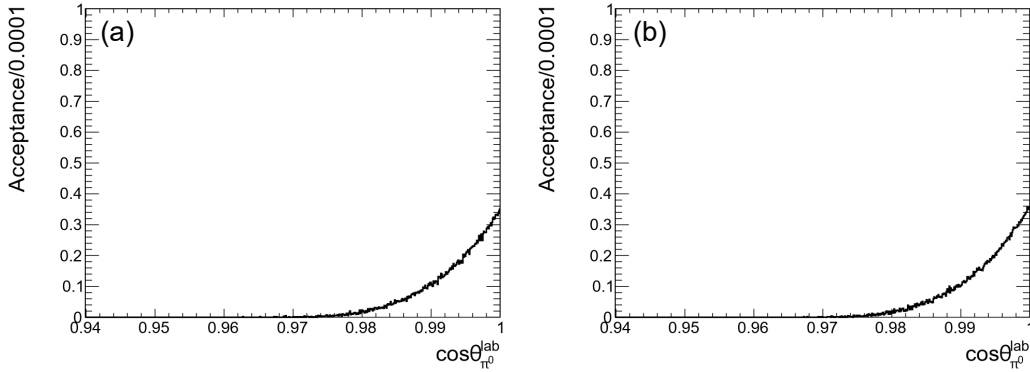
Figure 4.36: Acceptance of the PbF$_2$ calorimeter after selecting gamma-ray. (a) The acceptance of π^0 is shown when $^4_\Lambda$H is generated. (b) The acceptance of π^0 is shown when $^3_\Lambda$H is generated. The acceptance is the fraction of events in which the PbF$_2$ energy deposit is larger than 550 MeV within events that can be detected every angle.

π^- acceptance by CDS

The π^- acceptances by CDS were estimated for the two-body MWD of the hypernuclei. Hypernuclei were produced based on the beam profile intensity distribution in the experiment. The generated hypernuclei undergo the two-body decay. The events in which the decay π^- hit CDH
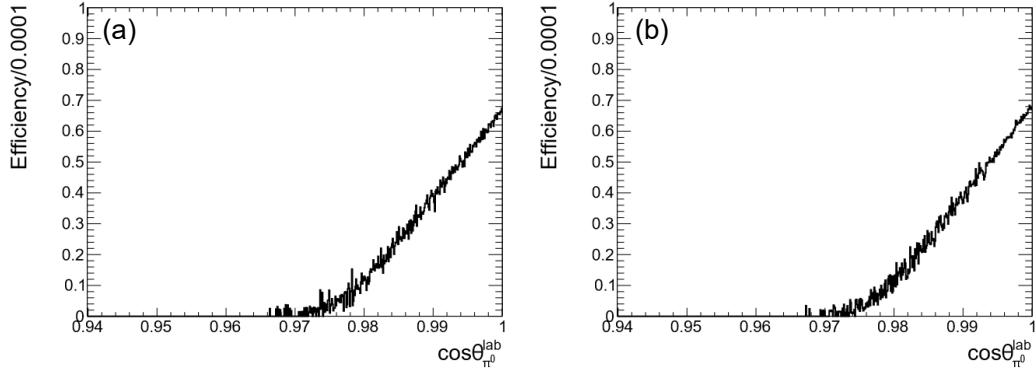
Figure 4.37: Gamma-ray selection efficiency by the PbF$_2$ calorimeter. (a) The efficiency of further selecting gamma-rays from the π^0 acceptance when $^4_\Lambda$H is generated is shown. (a) The efficiency of further selecting gamma-rays from the π^0 acceptance when $^3_\Lambda$H is generated is shown. The efficiency is the fraction of events in which the PbF$_2$ energy deposit is larger than 550 MeV.

were counted. The geometric acceptance was derived by dividing the number of CDH hits by the number of hypernucleus produced. Figure 4.38 shows the acceptance by CDS in every emitted angle. The ratio of accepted events to the total number is 51.5 ± 0.3 % for $^4_\Lambda$H and 49.8 ± 0.3 % for $^3_\Lambda$H.
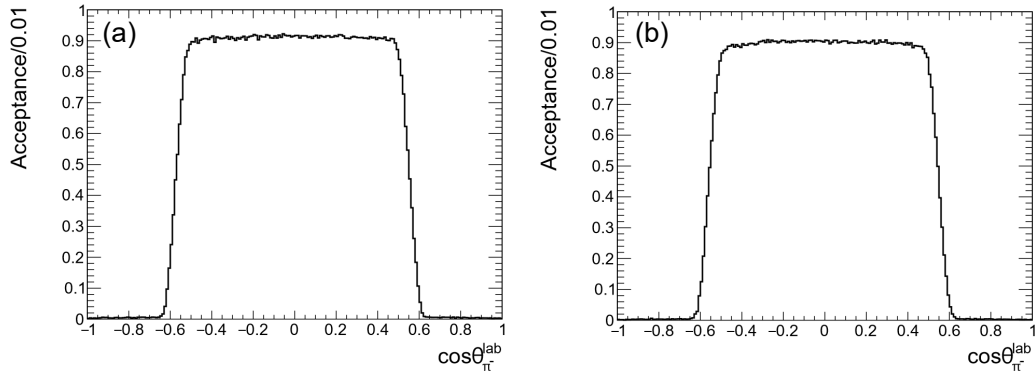
Figure 4.38: The π^- acceptances by CDS were estimated for π^- 0f the decay from the hypernucli. (a) The plot displays the acceptances for two-body MWD of $^4_\Lambda$H at 133 MeV/c π^- detected by CDS. (b) The plot displays the acceptances for two-body MWD of $^3_\Lambda$H at 114 MeV/c π^- detected by CDS.

Particle identification efficiency for π^- in CDS

As described in Sec 4.1, the selection of π^- is performed with the value of the mass-square. The value of mass-square of μ^- is close to that of pion. In this analysis, π^- are chosen to be

larger than 0.015 (GeV/c^2)^2 to eliminate μ^-. The survival efficiency of π^- emitted from the two-body decay of the hypernucleus was estimated by a Monte-Carlo simulation. As a result, the pion identification efficiency was estimated to be 94.8 $\pm$ 0.3 % for the helium-4 target runs and 96.5 $\pm$ 0.2 % for the helium-3 target runs.

DCA selection efficiency

As described in Sec. 4.1.3, the reaction vertex is reconstructed using the K^- beam and the CDC tracks, and the closest distance of the two tracks is used to select hypernucleus events. As in the case of the previous case, events were generated by the simulation calculation and the reaction vertex was reconstructed. By selecting the closest distance of less than 0.5 cm in the Monte-Carlo simulation, the survival efficiency was estimated. As a result, the closest distance selection efficiency was estimated to be 94.8 $\pm$ 0.5 % for the helium-4 target runs and 91.9 $\pm$ 0.5 % for the helium-3 target runs.

Chapter 5

Results and Discussion

In this chapter, the analysis results are reported. In particular, the $^{3,4}_{\Lambda}$H production cross section obtained by correcting the two-body decay branching ratio will be presented. Theoretical calculation suggests that the production cross section ratio $\sigma_{^3_\Lambda \text{H}}/\sigma_{^4_\Lambda \text{H}}$ in the (K^-, π^0) reaction is sensitive to the binding energy of $^3_\Lambda$H. The production cross section ratio is used to obtain the information of the binding energy of $^3_\Lambda$H. The results is compared with previous experimental measurements and theoretical calculations of the $^3_\Lambda$H binding energy. Finally, future prospects are discussed.

5.1 Results

5.1.1 Production cross section from two-body MWD

The production cross section of the $^{3,4}\text{He}(K^-, \pi^0)^{3,4}_{\Lambda}$H reaction is calculated using the experimental yield and several factors such as the detector efficiencies, the integrated luminosity, the acceptances of CDS and the PbF$_2$ calorimeter. Harada *et al.* [44] calculated the theoretical production cross section of hypernuclei with an angular distribution ranging from $0°$ to $20°$ in the laboratory system. The production cross section estimated in this analysis is the integral of differential cross sections by the π^0 scattering angle from $0°$ to $20°$, which is obtained from the numbers of the two-body decayed π^- events and the $^{3,4}_{\Lambda}$H decay branching ratios. In the present experiment, the cross section is defined as

$$\sigma^{\theta_{\text{lab}}=0°-20°}_{^{4,3}_{\Lambda}\text{H}} = \frac{N_{^{4,3}_{\Lambda}\text{H 2-body MWD}}}{L \cdot A_{\text{CDS}} \cdot A_{\text{PbF}_2} \cdot \epsilon_{\text{total}} \cdot Br_{\text{2-body}}}, \tag{5.1}$$

$$\epsilon_{\text{total}} = \epsilon_{\text{CDC}} \cdot \epsilon_{\text{PID}} \cdot \epsilon_{\text{PbF}_2} \cdot \epsilon_{\text{DCA}} \cdot \epsilon_{\text{DAQ}}.$$

Here, $N_{^{4,3}_{\Lambda}\text{H 2-body MWD}}$ is the number of π^- from the 2-body MWD detected by CDS as described in Sec. 4.5.1. L represent the integrated luminosity estimated in Sec. 3.3.5. A_{CDS} is the geometrical acceptance of CDS for π^-. A_{PbF_2} is the acceptance of the PbF$_2$ calorimeter for gamma-rays. The ϵs are the experimental efficiencies. Specificaly, ϵ_{CDC} is the CDC tracking

efficiency; ϵ_{PID} is the particle identification efficiency by CDS based on the simulation calculation; $\epsilon_{\mathrm{PbF_2}}$ is the selection efficiency for gamma-rays obtained from the simulation calculation; ϵ_{DCA} is selection efficiency for the DCA cut; ϵ_{DAQ} is the DAQ efficiency. Table 5.1 summarizes the factors used to derive the production cross section.

Table 5.1: Summary of the factors used to derive the production cross section.

target	helium-4			helium-3			
	value	stat.	syst.	value	stat.	syst.	Sec.
2-body MWD events	1465	± 45	$^{+5}_{-61}$	225	± 39	$^{+17}_{-25}$	4.5.1
Luminosity (μb^{-1})	868	± 24		984	± 27		3.3.5
A_{CDS}	0.515		± 0.003	0.498		± 0.003	4.5.2
$A_{\mathrm{PbF_2}}$	0.313		± 0.002	0.319		± 0.002	4.5.2
ϵ_{CDC}	0.981	± 0.002		0.977	± 0.003		3.4
ϵ_{PID}	0.948		± 0.003	0.965		± 0.002	4.5.2
$\epsilon_{\mathrm{PbF_2}}$	0.501		$^{+0.059}_{-0.062}$	0.514		$^{+0.060}_{-0.063}$	4.5.2
ϵ_{DCA}	0.948		± 0.005	0.919		± 0.005	4.5.2
ϵ_{DAQ}	0.918	± 0.007		0.926	± 0.004		2.8.2

Table 5.2 summarizes the systematic uncertainties of the production cross sections multiplied by the two-body MWD branching ratio.

Table 5.2: Summary of the systematic uncertainties for the production cross sections multiplied by the two-body MWD branching ratio

Contribution	Helium-4	Helium-3
fitting process	$^{+0.1}_{-1.1}\ \mu b$	$^{+0.3}_{-0.4}\ \mu b$
gamma-ray selection in PbF$_2$ calorimeter	$^{+3.0}_{-3.2}\ \mu b$	$\pm 0.4\ \mu b$
acceptance of CDS and PbF$_2$ calorimeter	$\pm 0.2\ \mu b$	$\pm 0.04\ \mu b$
efficiency in MC simulation calculation	$\pm 0.2\ \mu b$	$\pm 0.03\ \mu b$
Total (quadratic sum)	$^{+3.1}_{-3.4}\ \mu b$	$^{+0.5}_{-0.6}\ \mu b$

As a result, the production cross sections multiplied by the two-body MWD branching ratios are

$$\sigma^{\theta_{\mathrm{lab}}=0°-20°}_{^4_\Lambda\mathrm{H}} \times Br_{\text{2-body}}(^4_\Lambda\mathrm{H}) = 25.7 \pm 1.1\ (\text{stat.}) \ ^{+3.1}_{-3.4}\ (\text{syst.})\ \mu b,$$

$$\sigma^{\theta_{\mathrm{lab}}=0°-20°}_{^3_\Lambda\mathrm{H}} \times Br_{\text{2-body}}(^3_\Lambda\mathrm{H}) = 3.5 \pm 0.6\ (\text{stat.}) \ ^{+0.5}_{-0.6}\ (\text{syst.})\ \mu b.$$

5.1.2 Production cross section

Since the two-body MWD branching ratios cannot be measured in this experiment, the branching ratios obtained from previous experimental studies is used. The two-body decay branching ratio $(\Gamma(\mathrm{He} + \pi^-)/\Gamma_{\mathrm{all}})$ is calculated from the measured observables as follows:

$$\frac{\Gamma(^{4,3}\mathrm{He} + \pi^-)}{\Gamma_{\mathrm{all}}} = \frac{\Gamma(^{4,3}\mathrm{He} + \pi^-)}{\Gamma_{\pi^-}} \times \frac{1}{(1 + \frac{\Gamma_{\pi^0}}{\Gamma_{\pi^-}} + \frac{\Gamma_{\mathrm{nm}}}{\Gamma_{\pi^-}})}, \tag{5.2}$$

where Γ is the weak decay width. Γ_{π^-} is mesonic weak decay width of $^{4,3}_{\Lambda}\mathrm{H} \to X + \pi^-$. $\Gamma_{\pi^0}/\Gamma_{\pi^-}$ is the ratio of the mesonic weak decay widths of π^0 and π^-. $\Gamma_{\mathrm{nm}}/\Gamma_{\pi^-}$ is the ratio of the non-mesonic weak decay width of $^{4,3}_{\Lambda}\mathrm{H}$ and π^- mesonic weak decay width.

The values used in the calculation are summarized in Table 5.3.

Table 5.3: Summary of values for calculating the two-body MWD branching ratios.

Fractional branching ratio	Helium-4	Helium-3
$\Gamma(^{4,3}\mathrm{He} + \pi^-)/\Gamma_{\pi^-}$	0.690 ± 0.017 [68]	$0.357 ^{+0.028}_{-0.027}$ [68]
$\Gamma_{\pi^0}/\Gamma_{\pi^-}$	0.1 [70]	0.5 [34]
$\Gamma_{\mathrm{nm}}/\Gamma_{\pi^-}$	0.26 ± 0.13 [70]	0.025 [34]
$\Gamma(^{4,3}\mathrm{He} + \pi^-)/\Gamma_{\mathrm{all}}$	0.51 ± 0.05	0.23 ± 0.02

Finally, by correcting the two-body MWD branching ratios, the $^4_{\Lambda}\mathrm{H}$ and $^3_{\Lambda}\mathrm{H}$ production cross sections are estimated as,

$$\sigma^{\theta_{\mathrm{lab}}=0°-20°}_{^4_{\Lambda}\mathrm{H}} = 50.7 \pm 2.1 \,(\mathrm{stat.}) \,^{+7.8}_{-8.3} \,(\mathrm{syst.}) \,\mu\mathrm{b},$$

$$\sigma^{\theta_{\mathrm{lab}}=0°-20°}_{^3_{\Lambda}\mathrm{H}} = 15.0 \pm 2.6 \,(\mathrm{stat.}) \,^{+2.4}_{-2.8} \,(\mathrm{syst.}) \,\mu\mathrm{b}.$$

An additional systematic uncertainty are introduced due to errors of the branching ratios in previous experiments. The uncertainty in the two-body decay branching ratio is same level with the experimental systematic uncertainty. Future measurements of the branching ratios will reduce the systematic uncertainty of the production cross sections.

5.1.3   Production cross section ratio

The ratio $R_{34} = \sigma_{^3_\Lambda H}/\sigma_{^4_\Lambda H}$ is calculated using the production cross section given in the Sec. 5.1.1, 5.1.2. Because of the setup and analysis methods are same in this experiment, taking a ratio help to cancel out certain experimental uncertainty. the geometrical acceptances of CDS and PbF$_2$ and efficiencies of detectors are partially dropped out when calculating the R_{34}. This allows me to make less ambiguous comparison with the theoretical calculations. Table 5.4 summarizes the systematic uncertainties of the production cross section ratios multiplied by the two-body MWD branching ratios.

Table 5.4: Summary of the systematic uncertainties for the production cross section ratios multiplied by the two-body MWD branching ratio

Contribution	
fitting process	$^{+0.012}_{-0.015}$
gamma-ray selection in PbF$_2$ calorimeter	$^{+0.005}_{-0.002}$
acceptance of CDS and PbF$_2$ calorimeter	$\pm\,0.002$
efficiency in a MC simulation calculation	$\pm\,0.002$
Total (quadratic sum)	$^{+0.013}_{-0.015}$

As a result, the obtained production cross section ratio (R_{34}) multiplied by the two-body MWD branching ratios is

$$R_{34} \times \frac{Br_{\text{2-body}}(^3_\Lambda \text{H})}{Br_{\text{2-body}}(^4_\Lambda \text{H})} = 0.136 \pm 0.024 \text{ (stat.) } ^{+0.013}_{-0.015} \text{ (syst.).}$$

The obtained production cross section ratio (R_{34}) is

$$R_{34} = 0.295 \pm 0.053 \text{ (stat.) } ^{+0.047}_{-0.050} \text{ (syst.).}$$

5.2 Discussion

The theoretical estimation of the production cross section ratio between $^{3}_{\Lambda}$H and $^{4}_{\Lambda}$H by Harada *et al.*[44] is plotted in Fig. 5.1. The black crosses are the theoretically calculated production cross section ratio between $^{3}_{\Lambda}$H and $^{4}_{\Lambda}$H[71]. The horizontal red line in Fig. 5.1 is the value of the cross section ratio from present work, the long dashed lines shows the range of the statistical error and the short dashed lines shows the total errors. By comparing the theoretical calculation with the experimental values, $^{3}_{\Lambda}$H binding energy is estimated as follows:

$$B_\Lambda = 0.061 \, ^{+0.028}_{-0.022} \, (\text{stat.}) \, ^{+0.024}_{-0.021} \, (\text{syst.}) \, \text{MeV}.$$

The present results do not include the uncertainty of the theoretical calculations. The indeterminacy of this theoretical calculation is due to the assumption of a DWIA. The DWIA can approximately explain the production cross section of hypernuclei It is believed that the DWIA can approximately explain the production cross section of hypernuclei. However, it is questionable to what extent the DWIA is correct for reactions such as (K^-, π^0)[72]. The same is true for the ratio of hypernucleaar prodcution cross section; the shape factor also includes distorted waves due to mesons and is affected by these distorted wave features.
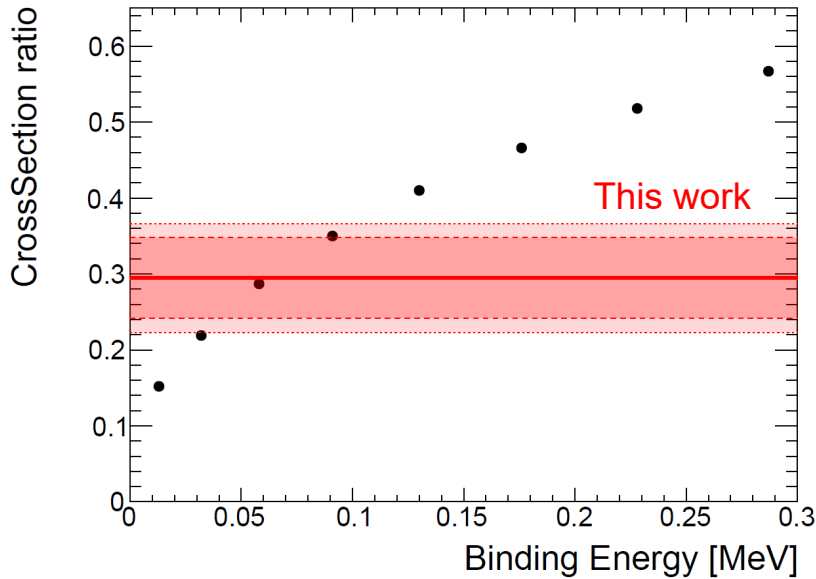

Figure 5.1: Crosses show the estimation of the theoretical calculation of the production cross section ratio as a function of the binding energy of $^{3}_{\Lambda}$H. The horizontal red line is the value of the cross section ratio from present work, the long dashed lines shows the range of the statistical errors, and the short dashed lines shows the total errors.

Figure 5.2 shows a summary of the measured Λ binding energies for $^{3}_{\Lambda}$H. The latest world average of the Λ binding energy of $^{3}_{\Lambda}$H, which combines the results of all previous experiments, is $B_{\Lambda} = 0.164 \pm 0.043$ MeV [68]. Recently, the $^{3}_{\Lambda}$H binding energy results reported $0.41 \pm 0.12(\text{stat.}) \pm 0.11(\text{syst.})$ MeV from the STAR collaboration and $0.102 \pm 0.063(\text{stat.}) \pm 0.067(\text{syst.})$ MeV from the ALICE collaboration. The Λ binding energy from this work has the smallest value of the binding energy, but is consistent with the world average and the ALICE results within statistical errors. It is worthwhile to mention that the result of the present work has the smallest statistical and systematic errors in the summary due to the completely different method in deriving the $^{3}_{\Lambda}$H binding energy. However, theoretical input of the relation between the $^{3}_{\Lambda}$H binding energy and the cross section ratio R_{34} should be carefully examined by further theoretical studies.
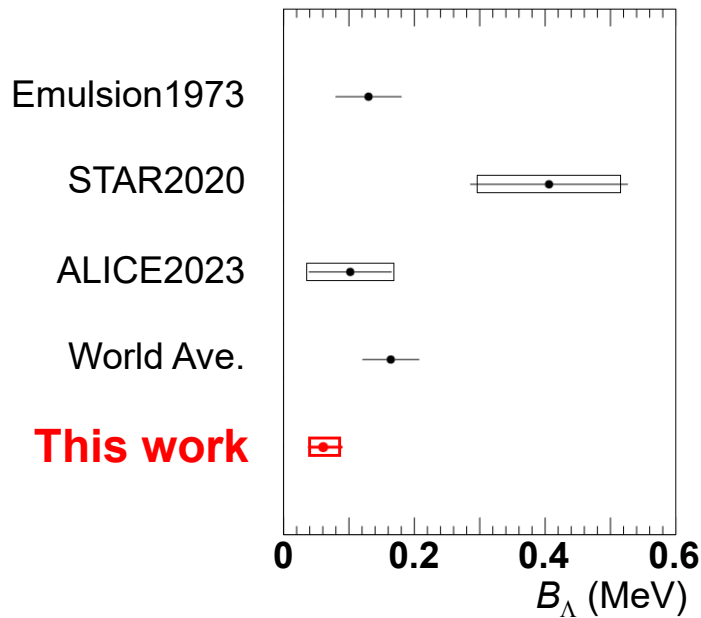

Figure 5.2: Summary of the measured Λ binding energies for $^{3}_{\Lambda}$H. The horizontal lines and boxes are the statistical and systematic uncertainties, respectively.

There are several theoretical calculations of B_{Λ} for $^{3}_{\Lambda}$H. In 1972, Dalitz reported a calculation of $B_{\Lambda} = 0.10$ MeV using a simple model that incorporates both a Λ-nucleon (ΛN) and a Λ-nucleon-nucleon (ΛNN) potential [38]. Recent calculations have yielded different results, with $B_{\Lambda} = 0.289$ MeV obtained based on SU(6) quark model baryon–baryon interactions [73], and B_{Λ} calculated to be 0.23 MeV using an auxiliary field diffusion Monte Carlo (AFDMC) method [39]. Another theoretical study considered ΛN and ΣN interactions at next-to-leading order in the SU(3) chiral effective field theory, resulting in a calculated binding energy of $^{3}_{\Lambda}$H ranging from 0.046 MeV to 0.162 MeV [40]. The result of this work may guide improvements and future development of theoretical works.

5.2.1 Future prospect

$^3_\Lambda$H lifetime

In the J-PARC E73 experiment, it is planned to obtain data to derive the lifetime of the $^3_\Lambda$H in the near future. The experimental method to derive the lifetime was established by deriving the lifetime of $^4_\Lambda$H [52], and the result is consistent with the values from the result reported by Outa *et al.*[74] and the STAR collaboration[21]. Similarly, it is possible to derive the lifetime of $^3_\Lambda$H in the J-PARC E73 experiment. It is expexted that future measurements of the $^3_\Lambda$H lifetime in this experiment will provide an answer to the $^3_\Lambda$H lifetime puzzle.

Chapter 6

Conclusion

The study of hypernuclei aims to understand the change in nuclear force resulting from the entry of strange quarks. This is achieved by measuring the forces acting between protons, neutrons, and lambda hyperons. Understanding the properties of the nuclear force based on quarks can unravel the origin and evolution of matter. In hypernuclear research, hypertriton ($^{3}_{\Lambda}$H) is one of the most significant hypernuclei. The lifetime and binding energy of $^{3}_{\Lambda}$H have been the focus of numerous experiments and remain topics of debate.

The J-PARC E73 experiment aims to address the $^{3}_{\Lambda}$H lifetime puzzle through the (K^{-}, π^{0}) reaction. It is crucial to determine complementary values for both the lifetime and binding energy, utilizing methods distinct from heavy-ion collision experiments. In this thesis, I measured the production cross sections of $^{4}_{\Lambda}$H and $^{3}_{\Lambda}$H in the (K^{-}, π^{0}) reaction at a kaon beam momentum of 1 GeV/c. Additionally, I estimated the binding energy of $^{3}_{\Lambda}$H through theoretical calculations.

A feasibility study was conducted with a helium-4 target and short production runs as a pilot experiment to measure the $^{3}_{\Lambda}$H production cross section on a helium-3 target. The Cylindrical Detector System (CDS) identified π^{-} particles from the two-body decay of $^{4}_{\Lambda}$H or $^{3}_{\Lambda}$H and obtained momentum spectra. Mono-momentum peaks resulting from the two-body decays of $^{4}_{\Lambda}$H and $^{3}_{\Lambda}$H were observed. The number of hypernuclei produced was estimated by fitting the signal and background in the π^{-} momentum spectrum. The majority of the background originated from the decay of hyperons produced through quasi-free processes. The momentum distribution was reproduced using Monte Carlo simulation. The estimated production cross sections for $^{4}_{\Lambda}$H and $^{3}_{\Lambda}$H via the (K^{-}, π^{0}) reactions are $50.7 \pm 2.1(\text{stat.})^{+7.8}_{-8.3}(\text{syst.})\mu$b and $15.0 \pm 2.6(\text{stat.}) ^{+2.4}_{-2.8}(\text{syst.})$ μb, respectively.

Theoretical calculations by Harada *et al.* using the Distorted-Wave Impulse Approximation (DWIA) framework suggest that the production cross-section ratio $\sigma_{^{3}_{\Lambda}\text{H}}/\sigma_{^{4}_{\Lambda}\text{H}}$ in the (K^{-}, π^{0}) reaction is sensitive to the binding energy of $^{3}_{\Lambda}$H. The estimated ratio $\sigma_{^{3}_{\Lambda}\text{H}}/\sigma_{^{4}_{\Lambda}\text{H}}$ is 0.295 ± 0.053 (stat.) $^{+0.047}_{-0.050}$ (syst.). The binding energy of $^{3}_{\Lambda}$H is estimated to be $0.061 ^{+0.028}_{-0.022}$ (stat.) $^{+0.024}_{-0.021}$(syst.) MeV from the production cross-section ratio with the theoretical information. The Λ binding energy from this work has the smallest value of the binding energy, but is consistent with the world average and the ALICE results within statistical errors.

In the near future, data will be obtained to derive the lifetime of $^{3}_{\Lambda}$H. It is expected that future

measurements of the $^3_\Lambda$H lifetime in this experiment will provide an answer to the $^3_\Lambda$H lifetime puzzle.

Acknowledgements

Bibliography

[1] V. G. J. Stoks, R. A. M. Klomp, C. P. F. Terheggen, and J. J. de Swart. Construction of high-quality NN potential models. *Phys. Rev. C*, 49:2950–2962, Jun 1994.

[2] R. B. Wiringa, V. G. J. Stoks, and R. Schiavilla. Accurate nucleon-nucleon potential with charge-independence breaking. *Phys. Rev. C*, 51:38–51, Jan 1995.

[3] R. Machleidt. High-precision, charge-dependent Bonn nucleon-nucleon potential. *Phys. Rev. C*, 63:024001, Jan 2001.

[4] Makoto Oka, Kiyotaka Shimizu, and Koichi Yazaki. Quark Cluster Model of Baryon-Baryon Interaction. *Progress of Theoretical Physics Supplement*, 137:1–20, 03 2000.

[5] Particle Data Group. Review of Particle Physics. *Phys. Rev. D*, 98:030001, Aug 2018.

[6] D.H. Davis. 50 years of hypernuclear physics: I. The early experiments. *Nuclear Physics A*, 754:3–13, 2005. Proceedings of the Eighth International Conference on Hypernuclear and Strange Particle Physics.

[7] H Bhang, S Ajimura, K Aoki, T Hasegawa, O Hashimoto, H Hotchi, YD Kim, T Kishimoto, K Maeda, H Noumi, et al. Lifetime Measurement of $^{12}_{\Lambda}$C, $^{28}_{\Lambda}$Si, and $_{\Lambda}$Fe Hypernuclei. *Physical review letters*, 81(20):4321, 1998.

[8] D. Bertrand, G. Coremans, C. Mayeur, J. Sacton, P. Vilain, G. Wilquet, J.H. Wickens, D. O'Sullivan, D.H. Davis, and J.E. Allen. Branching ratios for the π^{-} mesonic decays of the hypernuclei $^{3}_{\Lambda}$H and $^{4}_{\Lambda}$H. *Nuclear Physics B*, 16(1):77–84, 1970.

[9] M. Bedjidian, E. Descroix, J.Y. Grossiord, A. Guichard, M. Gusakow, M. Jacquin, M.J. Kudła, H. Piekarz, J. Piekarz, J.R. Pizzi, and J. Pniewski. Further investigation of the γ-transitions in $^{4}_{\Lambda}$H and $^{4}_{\Lambda}$He hypernuclei. *Physics Letters B*, 83(2):252–256, 1979.

[10] RJ Prem and PH Steinberg. Lifetimes of Hypernuclei, $^{3}_{\Lambda}$H, $^{4}_{\Lambda}$H, $^{5}_{\Lambda}$H. *Physical Review*, 136(6B):B1803, 1964.

[11] G Keyes, M Derrick, T Fields, LG Hyman, JG Fetkovich, J McKenzie, B Riley, and I-T Wang. New Measurement of the $^{3}_{\Lambda}$H Lifetime. *Physical Review Letters*, 20(15):819, 1968.

[12] RE Phillips and J Schneps. Lifetimes of light hyperfragments. II. *Physical Review*, 180(5):1307, 1969.

[13] Georg Bohm, J Klabuhn, U Krecker, F Wysotzki, Ghislaine Coremans, Jean Sacton, Pierre Vilain, John H Wickens, Gaston Wilquet, Denis O'Sullivan, et al. On the lifetime of the $^3_\Lambda$H hypernucleus. *Nuclear Physics B*, 16(1):46–52, 1970.

[14] G. Keyes, M. Derrick, T. Fields, L. G. Hyman, J. G. Fetkovich, J. McKenzie, B. Riley, and I. T. Wang. Properties of $^3_\Lambda$H. *Phys. Rev. D*, 1:66–77, Jan 1970.

[15] G Keyes, Jean Sacton, John H Wickens, and MM Block. A measurement of the lifetime of the $^3_\Lambda$H hypernucleus. *Nuclear Physics B*, 67(2):269–283, 1973.

[16] Star Collaboration, BI Abelev, MM Aggarwal, Z Ahammed, AV Alakhverdyants, I Alekseev, BD Anderson, D Arkhipin, GS Averichev, J Balewski, et al. Observation of an antimatter hypernucleus. *Science*, 328(5974):58–62, 2010.

[17] C Rappold, E Kim, D Nakajima, TR Saito, O Bertini, S Bianchin, V Bozkurt, M Kavatsyuk, Y Ma, F Maas, et al. Hypernuclear spectroscopy of products from ^{6}Li projectiles on a carbon target at 2 A GeV. *Nuclear Physics A*, 913:170–184, 2013.

[18] Alice Collaboration et al. $^3_\Lambda$H and $^3_\Lambda\overline{\text{H}}$ production in Pb–Pb collisions at $\sqrt{S_{NN}} = 2.76$ TeV. *Physics Letters B*, 754:360–372, 2016.

[19] L Adamczyk, JR Adams, James K Adkins, G Agakishiev, MM Aggarwal, Z Ahammed, NN Ajitanand, I Alekseev, J Alford, DM Anderson, et al. Measurement of the $^3_\Lambda$H lifetime in Au + Au collisions at the BNL Relativistic Heavy Ion Collider. *Physical Review C*, 97(5):054909, 2018.

[20] ALICE collaboration et al. $^3_\Lambda$H and $^3_\Lambda\overline{\text{H}}$ lifetime measurement in Pb–Pb collisions at $\sqrt{S_{NN}} = 5.02$ TeV via two-body decay. *Physics Letters B*, 797, 2019.

[21] MS Abdallah, BE Aboona, J Adam, L Adamczyk, JR Adams, JK Adkins, G Agakishiev, I Aggarwal, MM Aggarwal, Z Ahammed, et al. Measurements of $^3_\Lambda$H and $^4_\Lambda$H Lifetimes and Yields in Au + Au Collisions in the High Baryon Density Region. *Physical review letters*, 128(20):202301, 2022.

[22] S Acharya, D Adamová, A Adler, G Aglieri Rinella, M Agnello, N Agrawal, Z Ahammed, S Ahmad, SU Ahn, I Ahuja, et al. Measurement of the Lifetime and Λ Separation Energy of $^3_\Lambda$H. *Physical review letters*, 131(10):102302, 2023.

[23] Y. Prakash, P. H. Steinberg, D. Chandler, and R. J. Prem. On the binding energies of mesic hypernuclei. *Il Nuovo Cimento (1955-1965)*, 21:235–248, 1961.

[24] R. G. Ammar, W. Dunn, and M. Holland. On the Spin and Binding of $^3_\Lambda$H. 1962.

[25] C. Mayeur, J. Sacton, P. Vilain, G. Wilquet, D. Stanley, P. Allen, D. Davis, E. Fletcher, D. A. Garbutt, M. Shaukat, J. Allen, V. Bull, A. Conway, and P. March. A determination of the B$_\Lambda$ values of light hypernucleivalues of light hypernuclei. *Il Nuovo Cimento A (1971-1996)*, 43:180–192, 1966.

[26] W. Gajewski, C. Mayeur, J. Sacton, P. Vilain, G. Wilquet, D. Harmsen, R.Levi Setti, M. Raymund, J. Zakrzewski, D. Stanley, D.H. Davis, E.R. Fletcher, J.E. Allen, V.A. Bull, A.P. Conway, and P.V. March. A compilation of binding energy values of light hypernuclei. *Nuclear Physics B*, 1(3):105 – 113, 1967.

[27] G. Bohm, J. Klabuhn, U. Krecker, F. Wysotski, G. Coremans, W. Gajewski, C. Mayeur, J. Sacton, P. Vilain, G. Wilquet, D. O'Sullivan, D. Stanley, D.H. Davis, E.R. Fletcher, S.P. Lovell, N.C. Roy, J.H. Wickens, A. Filipkowski, K. Garbowska-Pniewska, T. Pniewski, E. Skrzypczak, T. Sobczak, J.E. Allen, V.A. Bull, A.P. Conway, A. Fishwick, and P.V. March. A determination of the binding-energy values of light hypernuclei. *Nuclear Physics B*, 4(6):511 – 526, 1968.

[28] Mira Jurič, Georg Bohm, J Klabuhn, U Krecker, F Wysotzki, Gh Coremans-Bertrand, Jean Sacton, Gaston Wilquet, Tom Cantwell, F Esmael, et al. A new determination of the binding-energy values of the light hypernuclei (A ≤ 15). *Nuclear physics B*, 52(1):1–30, 1973.

[29] Measurement of the mass difference and the binding energy of the hypertriton and antihypertriton. *Nature Physics*, 16(4):409–412, 2020.

[30] PG Hansen, AS Jensen, and B Jonson. Nuclear halos. *Annual Review of Nuclear and Particle Science*, 45(1):591–634, 1995.

[31] A Cobis, A S Jensen, and D V Fedorov. The simplest strange three-body halo. *Journal of Physics G: Nuclear and Particle Physics*, 23(4):401, apr 1997.

[32] M Rayet and RH Dalitz. The lifetime of $^3_\Lambda$H. *Il Nuovo Cimento A (1971-1996)*, 46:786–794, 1966.

[33] JG Gongleton. A simple model of the hypertriton. *Journal of Physics G: Nuclear and Particle Physics*, 18(2):339, 1992.

[34] H Kamada, J Golak, K Miyagawa, H Witała, and W Gloeckle. π^- mesonic decay of the hypertriton. *Physical Review C*, 57(4):1595, 1998.

[35] Avraham Gal and Humberto Garcilazo. Towards resolving the $^3_\Lambda$H lifetime puzzle. *Physics Letters B*, 791:48–53, 2019.

[36] F Hildenbrand and H-W Hammer. Lifetime of the hypertriton. *Physical Review C*, 102(6):064002, 2020.

[37] A Pérez-Obiol, D Gazda, E Friedman, and A Gal. Revisiting the hypertriton lifetime puzzle. *Physics Letters B*, 811:135916, 2020.

[38] RH Dalitz, RC Herndon, and YC Tang. Phenomenological study of s-shell hypernuclei with ΛN and ΛNN potentials. *Nuclear Physics B*, 47(1):109–137, 1972.

[39] Diego Lonardoni and Francesco Pederiva. Medium-mass hypernuclei and the nucleon-isospin dependence of the three-body hyperon-nucleon-nucleon force. *arXiv preprint arXiv:1711.07521*, 2017.

[40] J Haidenbauer, U-G Meißner, and Andreas Nogga. Hyperon-nucleon interaction within chiral effective field theory revisited. *The European Physical Journal A*, 56(3):91, 2020.

[41] Y. Ma et al. $^{3}_{\Lambda}$H and $^{4}_{\Lambda}$H mesonic weak decay lifetime measurement with ^{3,4}He$(k^{-}, \pi^{0})^{3,4}_{\Lambda}$H reaction. *J-PARC E73 proposal*, 2018.

[42] T.Yamamoto. Ph.D. thesis Tohoku University. 2016, p.18.

[43] A. Rusek. $(K^{-}_{\text{stop}}, \pi^{0})$ with the neutral meson spectrometer. *Nuclear Physics A*, 639(1):111c–116c, 1998. Proceedings of the International Conference on Hypernuclear and Strange Particle Physics.

[44] Toru Harada and Yoshiharu Hirabayashi. Production cross sections of $^{3,4}_{\Lambda}$H bound states in ^{3,4}He(K^{-}, π^{0}) reactions at 1 GeV/c. *Nuclear Physics A*, 1015:122301, 2021.

[45] F. Dohrmann, A. Ahmidouch, C. S. Armstrong, J. Arrington, R. Asaturyan, S. Avery, K. Bailey, H. Bitao, H. Breuer, D. S. Brown, R. Carlini, J. Cha, N. Chant, E. Christy, A. Cochran, L. Cole, J. Crowder, S. Danagoulian, M. Elaasar, R. Ent, H. Fenker, Y. Fujii, L. Gan, K. Garrow, D. F. Geesaman, P. Gueye, K. Hafidi, W. Hinton, H. Juengst, C. Keppel, Y. Liang, J. H. Liu, A. Lung, D. Mack, P. Markowitz, J. Mitchell, T. Miyoshi, H. Mkrtchyan, S. K. Mtingwa, B. Mueller, G. Niculescu, I. Niculescu, D. Potterveld, B. A. Raue, P. E. Reimer, J. Reinhold, J. Roche, M. Sarsour, Y. Sato, R. E. Segel, A. Semenov, S. Stepanyan, V. Tadevosian, S. Tajima, L. Tang, A. Uzzle, S. Wood, H. Yamaguchi, C. Yan, L. Yuan, B. Zeidman, M. Zeier, and B. Zihlmann. Angular Distributions for $^{3,4}_{\Lambda}$H Bound States in the ^{3,4}He$(e, e'K^{+})$ Reaction. *Phys. Rev. Lett.*, 93:242501, Dec 2004.

[46] KEK Report99. The joint project for high-intensity proton accelerators. *JAERI-Tech*, 99:056, 1999.

[47] M. Tomizawa, Y. Arakaki, T. Kimura, R. Muto, S. Murasugi, K. Okamura, H. Sato, Y. Shirakabe, and E. Yanaoka. Slow extraction from the J-PARC main ring using a dynamic bump. *Nuclear Instruments and Methods in Physics Research Section A: Accelerators, Spectrometers, Detectors and Associated Equipment*, 902:51–61, 2018.

[48] Ryotaro Muto, Yoshitsugu Arakaki, Takuro Kimura, S Murasugi, M Okada, K Okamura, T Shimogawa, Y Shirakabe, M Tomizawa, T Toyama, et al. Current status of slow extraction from J-PARC Main Ring. In *Journal of Physics: Conference Series*, volume 1350, page 012105. IOP Publishing, 2019.

[49] Keizo Agari, Shuhei Ajimura, George Beer, Hyoungchan Bhang, Mario Bragadireanu, Paul Buehler, Luigi Busso, Michael Cargnelli, Seonho Choi, and Catalina Curceanu. The K1.8BR spectrometer system at J-PARC. *Progress of Theoretical and Experimental Physics*, page 02B011, 2012.

[50] Keizo Agari, Shun Enomoto, Hiroyuki Fujioka, Yuya Fujiwara, Tadashi Hashimoto, Ryugo S Hayano, Toshihiko Hiraiwa, Erina Hirose, Masaharu Ieiri, and Youichi Igarashi. Secondary charged beam lines at the J-PARC hadron experimental hall. *Progress of Theoretical and Experimental Physics*, page 02B009, 2012.

[51] T.Hashimoto. Ph.D. thesis University of Tokyo. 2013.

[52] T. Akaishi et al. Precise lifetime measurement of $^4_\Lambda$H hypernucleus using in-flight ^{4}He$(K^-, \pi^0)^4_\Lambda$H reaction. *Phys. Lett. B*, 845:138128, 2023.

[53] Y Yoshimura. Crystal Cherenkov Radiator KEK Proceedings 97-9. In *Proceedings of the Workshop on Scintillating Crystals*, pages 178–183, 1997.

[54] DF Anderson, M Kobayashi, CL Woody, and Y Yoshimura. Lead fluoride: An ultra-compact Cherenkov radiator for EM calorimetry. *Nuclear Instruments and Methods in Physics Research Section A: Accelerators, Spectrometers, Detectors and Associated Equipment*, 290(2-3):385–389, 1990.

[55] HIROYUKI HAMA. ELPH, Towards Scientific Research Core Based on Electron Accelerators. *AAPPS Bulletin*, 30(2), 2020.

[56] Fujio Hinode, H Hama, Masayuki Kawai, A Kurihara, M Mutoh, M Nanao, Y Shibasaki, S Takahashi, T Tanaka, A Miyamoto, et al. Lattice modification of a 1.2 GEV STB ring for generation of high energy gamma-rays using internal target wire. In *Proceedings of the 2005 Particle Accelerator Conference*, pages 2458–2460. IEEE, 2005.

[57] F Hinode, S Kashiwagi, T Muto, I Nagasawa, K Nanbu, Y Shibasaki, K Takahashi, and H Hama. Status of upgrade project of the 1.2 GeV booster synchrotron at tohoku university. In *Proc. 4th Int. Particle Accelerator Conf.(IPAC'13)*, pages 151–153, 2013.

[58] Fujio Hinode, I Nagasawa, Shigeru Kashiwagi, Toshiya Muto, K Nanbu, Y Shibasaki, K Takahashi, C Tokoku, and H Hama. Status of the 1.3 GeV booster synchrotron for generating high energy gamma rays at Tohoku University. In *7th Int. Particle Accelerator Conf.(IPAC'16), Busan, Korea, May 8-13, 2016*, pages 701–703. JACOW, Geneva, Switzerland, 2016.

[59] T. Ishikawa, H. Fujimura, R. Hashimoto, T. Ishida, J. Kasagi, T. Kinoshita, S. Kuwasaki, F. Miyahara, A. Miyamoto, K. Mochizuki, T. Nakabayashi, M. Nanao, K. Nawa, Y. Okada, K. Okamura, Y. Onodera, Y. Saito, K. Satou, M. Sengoku, H. Shimizu, K. Suzuki, S. Suzuki, Y. Tajima, T. Takahashi, H. Yamazaki, H. Yonemura, and H.Y. Yoshida. The second GeV tagged photon beamline at ELPH. *Nuclear Instruments and Methods in Physics Research Section A: Accelerators, Spectrometers, Detectors and Associated Equipment*, 622(1):1–10, 2010.

[60] T Ishikawa, H Fujimura, R Hashimoto, T Ishida, J Kasagi, T Kinoshita, S Kuwasaki, F Miyahara, A Miyamoto, K Mochizuki, et al. The second GeV tagged photon beamline at ELPH. *Nuclear Instruments and Methods in Physics Research Section A: Accelerators, Spectrometers, Detectors and Associated Equipment*, 622(1):1–10, 2010.

[61] AT Fienberg, LP Alonzi, A Anastasi, R Bjorkquist, Diego Cauz, R Fatemi, C Ferrari, A Fioretti, A Frankenthal, C Gabbanini, et al. Studies of an array of PbF2 Cherenkov crystals with large-area SiPM readout. *Nuclear Instruments and Methods in Physics Research Section A: Accelerators, Spectrometers, Detectors and Associated Equipment*, 783:12–21, 2015.

[62] Youichi Igarashi, Masahiro Ikeno, Masatoshi Saito, Kazuo Nakayoshi, Manobu Tanaka, Tomonori Takahashi, Manabu Moritsu, Atsushi Okamura, Kenji Hosomi, Toshiyuki Takahashi, and Kenta Itahashi. An Integrated Data Acquisition System for J-PARC Hadron Experiments. *IEEE Transactions on Nuclear Science*, 57(2):618–624, 2010.

[63] Hadron Universal Logic module User Guide.

[64] Robert B Wiringa. Variational calculations of few-body nuclei. *Physical Review C*, 43(4):1585, 1991.

[65] E Jans, P Barreau, M Bernheim, JM Finn, J Morgenstern, J Mougey, D Tarnowski, S Turck-Chieze, S Frullani, F Garibaldi, et al. Quasifree $(e, e'p)$ Reaction on ^{3}He. *Physical Review Letters*, 49(14):974, 1982.

[66] M Jones, R Levi Setti, D Merrill, and RD Tripp. $K^- p$ charge exchange and hyperon production cross sections from 860 to 1000 MeV/c. *Nuclear Physics B*, 90:349–383, 1975.

[67] B Conforto, GP Gopal, GE Kalmus, PJ Litchfield, RT Ross, AJ Van Horn, TC Bacon, I Butterworth, EF Clayton, RM Waters, et al. $K^- p$ reactions from 0.960 to 1.355 GeV/c involving two-body final states. *Nuclear Physics B*, 105(2):189–221, 1976.

[68] P Eckert, P Achenbach, et al. Chart of hypernuclides—Hypernuclear structure and decay data. 2021.

[69] T Motoba, H Bandō, T Fukuda, and J Žofka. Continuum pion spectra in the weak decays of $^4_\Lambda$H, $^5_\Lambda$He and $^6_{\Lambda\Lambda}$He. *Nuclear Physics A*, 534(3-4):597–619, 1991.

[70] W. O. Lock, editor. *International Conference on Hyperfragments, St. Cergue, Switzerland, 28-30 March, 1963: Proceedings*, CERN Yellow Reports: Conference Proceedings, p.62–78, 1 1964.

[71] T. Harada. In the private communication (2023).

[72] Toru Harada and Yoshiharu Hirabayashi. Extended optimal Fermi averaging for near-recoilless Λ production in the (K^-, π^-) reaction on nuclei. *Phys. Rev. C*, 105:064606, Jun 2022.

[73] Y Fujiwara, Y Suzuki, M Kohno, K Miyagawa, et al. Addendum to triton and hypertriton binding energies calculated from SU 6 quark-model baryon-baryon interactions. *Physical Review C*, 77(2):027001, 2008.

[74] H. Outa, M. Aoki, R. S. Hayano, T. Ishikawa, M. Iwasaki, A. Sakaguchi, E. Takada, H. Tamura, and T. Yamazaki. Lifetime measurement of $^{4}_{\Lambda}$H hypernucleus. *Nucl. Phys. A*, 547:109C–114C, 1992.